Photosensitization of Inorganic Semiconducting Nanostructures for Solar Energy Conversion

Francisco Yarur Villanueva

A Thesis in the Department of Chemistry & Biochemistry

Presented in Partial Fulfillment of the Requirements for the Degree of Master of Science (Chemistry) at Concordia University
Montreal, Quebec, Canada

July 2020

Concordia University

School of Graduate Studies

This is to certify that the thesis prepared

By: Francisco Yarur Villanueva

Entitled: Photosensitization of Inorganic Semiconducting Nanostructures for Solar Energy Conversion

and submitted in partial fulfillment of the requirements for the degree of

Master of Science (Inorganic Photochemistry)

complies with the regulations of the University and meets the accepted standards with respect to originality and quality.

Signed by the final Examining Committee:

_____Chair

Dr. Paul Joyce

_____Examiner

Dr. Ashlee Howarth

_____Examiner

Dr. Laszlo Kalman

_____Supervisor

Dr. Marek B. Majewski

Approved by _____

Dr. Yves Gélinas, GPD

July 24th, 2020 _____

Pascale Sicotte, Dean of Faculty

Abstract

Photosensitization of Inorganic Semiconducting Nanostructures for Solar Energy Conversion

Francisco Yarur Villanueva

The engineering of efficient solar energy conversion devices with Earth-abundant elements is of paramount importance to meet the energy demands of a carbon-neutral society and to mitigate environmental damage. Converting solar energy into clean solar fuels and to drive industrially relevant processes is an attractive alternative to address the global energy problem. Typical molecular methods for the production of solar fuels make use of photosensitizers containing precious metals in order to harvest visible light. Carbon dots and kesterite nanocrystals have both recently and separately been considered as suitable candidates to photosensitize metal oxide structures due to their low cost and absorption across the visible portion of the solar spectrum. The physical and electronic architecture of these nanohybrids is a crucial factor that will dictate their optical and catalytic properties.

In this work, the photosensitization of zinc oxide nanowires with carbon dots to produce solar fuels is explored. In addition, due to the unknown formation pathway of carbon dots, the formation mechanism for the synthesis of kesterite Cu_2ZnSnS_4 nanocrystals is evaluated to achieve better control at tuning the optical and photocatalytic properties of nanomaterials. The carbon dot system is employed as a heterogeneous photocatalytic electrode surface for the α-heteroarylation of 1-phenylpyrrolidine and the generation of a high value-added benzyl amine pharmacophore. Furthermore, insight into possible mechanisms of electron transfer between the photoelectrode and

organic substrate is presented. Regarding the kesterite nanocrystals, the optimization of their synthesis to tailor the size dispersity is investigated given the strong correlation between the size and function of nanomaterials. A non-classical formation mechanism is suggested with the formation of a copper-sulfide intermediate followed by the incorporation of Sn^{4+} and Zn^{2+} through cation exchange.

Acknowledgements

First, I would like to thank my supervisor Dr. Marek B. Majewski for his guidance, useful advice, and encouragement that helped me excel in my research. I must also thank Dr. John Manioudakis and Jian Tian Liu for their assistance and suggestions to the research and to my lab colleagues Joseph Ricardo Noordberg, William Leal, and Zujhar Singh. I would also like to thank the Howarth and the Naccache groups for their insightful discussions. I should also thank Kirstin Buenviaje and Shahnaj Ullah for their assistance with the synthetic procedures. I would like to thank my committee members Dr. Ashlee Howarth, Dr. Laszlo Kalman, and Dr. Rafik Naccache for their advice and assistance throughout the years.

I thank the Natural Sciences and Engineering Research Council of Canada (NSERC), Fonds de Recherche du Québec − Nature et technologies (FRQNT), and Quebec Centre for Advanced Materials (QCAM) for financial support. I would like to thank Concordia University for research support under a Graduate Scholarship in Natural Sciences and Engineering Research (CGS NSER) award. SEM work was carried out by Hudson Bicalho at the Federal University of Minas Gerais. XPS analysis was performed at McGill University (MIAM) with the assistance of Dr. Lihong Shang. TEM work was performed at McGill University (MILab) in the Chemistry Characterization facility with the assistance of Mohini Ramkaran and at Polytechnique Montreal in the Centre for Characterization and Microscopy of Materials (CM2) with the assistance of Jean-Philippe Masse. DRS and profilometry was performed at Université de Montréal (LAMP lab) with the assistance of Dr. Daniel Chartrand. Mass spectrometry work was done at the Centre for Biological Applications of Mass Spectrometry (CBAMS) with the assistance of Alain Tessier. Raman spectroscopy was performed at Université de Montréal with the assistance of Professor Nikolay

Kornienko. Density functional theory calculations were done by Hang Hu at Centre for Research in Molecular Modeling (CERMM) at Concordia University.

I would like to thank my friends for the good times; soccer, hockey and rugby games, trips, beers, etc. that made graduate school an extra-enjoyable experience. I must also thank my family for their love, support, and for bearing with me when I would start talking about my research.

I would like to dedicate this work to my beloved mother who unfortunately left us halfway through my degree. This work is the fruit of her unconditional love and encouragement in my endeavors.

Contribution of Authors

In all chapters, Prof. Marek B. Majewski acted in a supervisory role. Chapter 2 involved collaboration with Prof. Rafik Naccache and Dr. John Manioudakis at Concordia University.

Chapter 2 has been published previously, and I am the principal author of this work. I carried out the majority of the experimental work in this chapter with the exception that Dr. John Manioudakis first synthesized both RCDs and PD2-CDs and characterized them through FTIR and XPS. I am the principal author of the work in Chapter 3.

Publications arising from this work:

Yarur Villanueva, F.; Manioudakis, J.; Naccache, R.; Majewski, M. B., Carbon Dot-Sensitized Photoanodes for Visible Light-Driven Organic Transformations. *ACS Appl. Nano Mater.* **2020**, *3* (3), 2756-2765.

Table of Contents

List of Figures

List of Tables

List of Abbreviations

BE	bulk electrolysis
CA	chronoamperometry
CD	carbon dot
CE	counter electrode
CNT	classical nucleation theory
CZTS	Cu_2ZnSnS_4
DHN	dihydronaphtalene
DMA	N,N-dimethylacetamide
DRIFTS	diffuse reflectance infrared Fourier-transform spectroscopy
DRS	diffuse reflectance spectroscopy
EDS	energy-dispersive X-ray spectroscopy
FTIR-ATR	Fourier-transform infrared attenuated total reflectance
FWHM	full width at half maximum
FTO	fluorine-doped tin oxide
GCD	green carbon dot
HI	hot-injection
HMTA	hexamethylenetetramine
HOMO	highest occupied molecular orbital
LUMO	lowest unoccupied molecular orbital
MOx	metal oxide
NC	nanocrystal
NIR	near infrared

NM	nanomaterial
NMR	nuclear magnetic resonance
NP	nanoparticle
NW	nanowire
OA	oleylamine
OR	Ostwald ripening
PD2-CD	propylenediamine carbon dot
PEC	photoelectrochemical
PXRD	powder X-ray diffraction
RCD	red carbon dot
RE	reference electrode
SC	semiconductor
SEM	scanning electron microscopy
SET	single electron transfer
$TBAPF_6$	tetrabutylammoniumhexafluorophosphate
TEM	transmission electron microscopy
TMB	1,3,5-trimethoxybenzene
XPS	X-ray photoelectron spectroscopy
WE	working electrode

Chapter 1 Introduction

1.1 Solar-to-Chemical Energy Conversion

The detrimental effects of the use of fossil fuels have brought about the need to develop sustainable and renewable energy technologies to supply the energetic demands of a carbon-neutral society. Solar energy is widely regarded as one of the most promising sources of renewable energy due to its great abundance and the fast-emerging technologies that benefit from it. This energy can be converted into electricity with efficiencies of 43.5% with photovoltaic devices.[1] However, harvesting solar energy and storing it in chemical bonds (*i.e.* artificial photosynthesis) has garnered significant attention as a strategy to work in conjunction with photovoltaic systems to meet global energy demands.

There exists a plethora of opportunities when it comes to the production of solar fuels including the generation of hydrogen from water splitting and the formation of hydrocarbons from the reduction of carbon dioxide.[2-3] Artificial photosynthetic systems require, amongst other things, a high stability under continuous light irradiation and the use of Earth-abundant elements to make these technologies economically feasible. Current strategies for the generation of solar fuels employ electrolyzers and thermochemical methods.[4-5] While these systems are efficient at producing significant amounts of solar fuels, they are not economically sustainable because they require large inputs of energy to drive the conversion process. Therefore, research has focused on the creation of photoelectrochemical (PEC) cells for solar-to-chemical energy conversion where a photoactive material, usually a semiconductor (SC), performs the conversion upon light irradiation.[6] One of the most efficient PEC systems to-date

are tandem cells for water splitting.[7] These devices have two or more SCs connected in series that produce enough potential to electrolyze water. For instance, Varadhan *et al.* achieved 9% efficiency for ~150 hrs for the production of hydrogen using a double junction cell from InGaP and GaAs.[8] Nonetheless, these devices suffer from photocorrosion under operating conditions diminishing the performance over time. To decrease photocorrosion, the surface of the active material can be coated with a thin layer of a polymer or co-catalyst as has been previously explored. This protective technique has achieved remarkable efficiencies in tandem cells.[9-10] The use of metal oxide (MOx) nanomaterials (NMs) as SCs has attracted significant attention within the past few decades as another strategy to prevent photocorrosion. These SCs have a high stability, low cost, high surface area, and ability to absorb light from different parts of the solar spectrum.

1.2 Solar-to-Chemical Using Metal Oxide Semiconductors

The production of solar fuels *via* MOx SCs offers several advantages compared to the generation of electricity through photovoltaics, mainly because of the simplicity of the device design. Devices made up of MOx SCs may be engineered from Earth-abundant elements and typically involve the use of a few layers of different materials coming together to achieve the conversion of solar energy into solar fuels. The absorption of a photon by the SC is characterized by an intrinsic threshold photon energy (the bandgap energy, E_{bg}). The absorption probability is proportional to the oscillator strength and density of occupied states in the valence band and unoccupied states in the conduction band. An absorbed photon will always produce an electronic transition, creating an exciton (associated electron-hole pair) with a specific binding energy (Step 1, Figure 1.1). The binding energy must be overcome to separate the charges (Step 2, Figure 1.1) that can then be used for follow-on redox reactions

(Step 3, Figure 1.1). Many known conventional semiconducting materials are wide bandgap materials and their use for solar fuels production is partially hindered by the resulting limited absorption range in the solar spectrum, as well as the difficulty to find a single SC with low h^+/e^- recombination rates while having enough driving force for the targeted conversion. This problem can be bypassed by designing p-n SC junctions or by the attachment of photosensitizers onto the surface of the SC.[11-12]

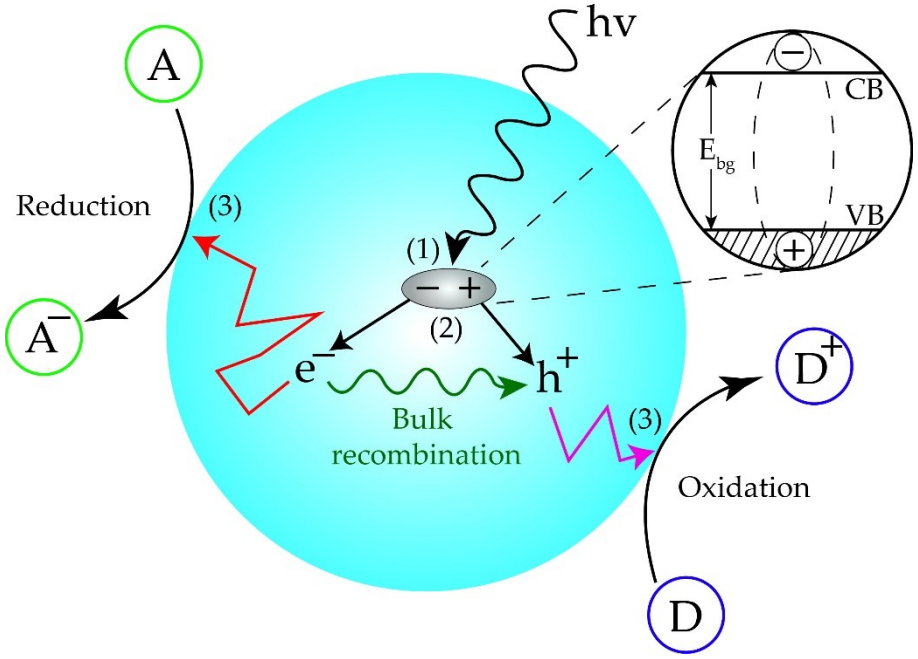

Figure 1.1 Photocatalytic process in semiconductors. The absorption of a photon with $h\nu \geq E_{bg}$ by the semiconductor creates an exciton (Step 1) with a specific binding energy. Close-up shows how the electron and the hole bind through Coulombic interactions across the conduction and valence bands. Once the binding energy is overcome (through thermal absorption, electric field, etc.) the exciton dissociates into free charges (Step 2). These charges can recombine where the energy is lost as heat or photon emission (bulk recombination), or they can reach the surface and drive useful redox processes (Step 3).

A feature of this type of solar energy conversion scheme is the direct contact between the device and the reaction solution. The transfer of charges happens at this interface through an equilibration between the redox potential of the electrolyte solution and the Fermi level (E_F)

of the SC (or chemical potential). In an optimal configuration, there will be creation of a Schottky-like junction between the SC surface and the electrolyte due to the formation of a depletion layer generated from the consumption of charge carriers at the interface,[13] leading to a bending of the conduction and valence bands of the SC (Figure 1.2). The formation of this junction is key to the rectification of charge transfer and the decrease of carrier recombination.

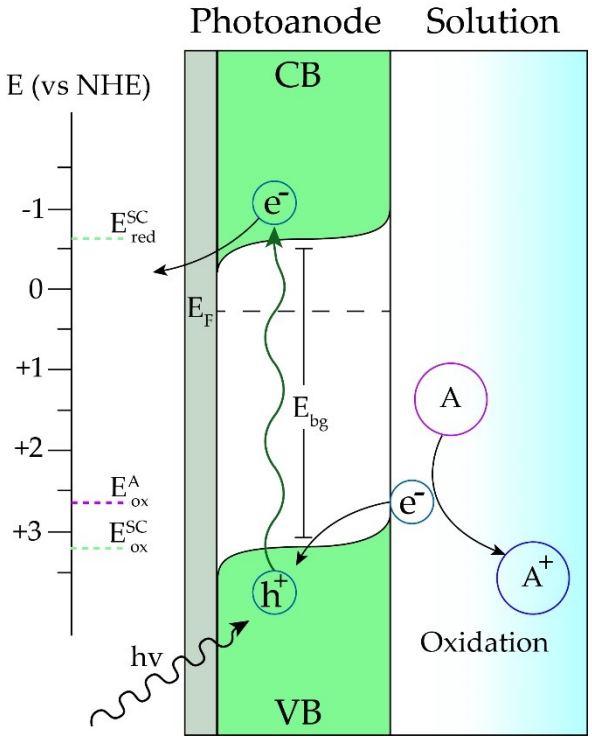

Figure 1.2 Solid-liquid interface between the photoanode and the electrolyte solution. The band bending is a product of the generation of a charge depletion layer. A Schottky junction behavior is observed as a consequence of the depletion of charges.

Binary MOx SCs including ZnO ($E_{bg} \approx 3.2$) and TiO_2 ($E_{bg} \approx 3.3$ eV) have simple and economical synthesis procedures, and have been shown to maintain their chemical and structural composition during PEC processes.[1] However, the bandgap energies for these SCs are not fully suitable for solar energy harvesting (Figure 1.3) with respect to capturing photons from the visible portion of the solar spectrum. Thus, additional strategies to maximize visible-

light absorption must be considered, and these may include nanostructuring and photosensitization of the surface.

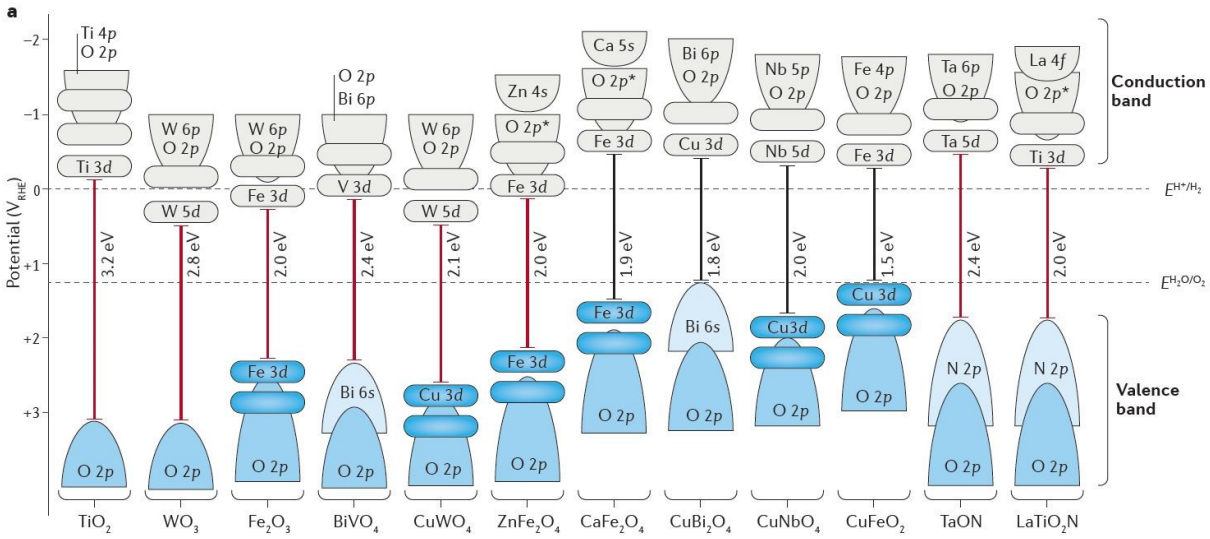

Figure 1.3 Bandgap energies for different metal oxide semiconductors (reprinted with permission from ref. 14)

1.3 Nanostructuring

Photoelectrochemical catalysis with nanoscale systems has increased in popularity in the last decade with work focusing on Ni_xO and RuO_2 nanostructures.[15-16] These materials were found to operate with low efficiency and require high energy UV light for activation. However, the efficiency of NMs can be increased considerably by exploiting the properties intrinsic to materials at the nanoscale including large surface areas and shorter carrier collection pathways. The favorable influence of these properties on the performance of PEC devices was first shown by Vante *et al*. in 1983 with copper(I) complexes.[17] Nevertheless, O'Regan and Grätzel demonstrated the practical applicability of such devices in 1991 with the dye-sensitized solar cell, also popularizing the possibility to photosensitize SCs to visible light.[18]

The solar PEC process relies on favorable electrical and optical properties of the material for visible light absorption, charge separation, and charge transport. These properties can be tailored for optimal performance by the variation of the size and morphology of the structure. Nonetheless, in some cases, the variation of these parameters can bring about some drawbacks as well. Hence, there ought to be a methodical optimization of the nanostructure taking both advantages and disadvantages into account. The pros and cons of nanoscaling with regards to solar PEC processes will be discussed before examining the use of photosensitizers (Sections 1.3.1 and 1.3.2).

1.3.1 Advantages of Nanoscaling in PEC Devices

1.3.1.1- Enhanced Surface Area

The surface area-to-volume ratio is significantly larger for NMs than their bulk counterparts, meaning that most of the material lies on the surface. Large surface areas grant NMs optimal properties for photocatalysis by having more active site-substrate interactions. This translates to lower overpotentials due to faster kinetics for the photocatalytic process.[19] For example, Amano *et al.* observed a faster photocatalytic decomposition of acetaldehyde on Bi_2WO_6 as the surface area of the nanostructures increased.[20]

1.3.1.2- Quantum Confinement

The size and morphology of NMs play a crucial role in the bandgap energy of the material. This phenomenon happens due to the size of the material being of the same dimensions as the exciton Bohr radius. When that dimension is reached, the energy levels' continuum is collapsed due to the quantization of momentum. Therefore, the solution for the energy of the confined electron becomes (from the Schrödinger equation):

$$E_n = \frac{h^2 n^2}{2 m_e L^2} \qquad \textbf{Eq. 1.1}$$

where the energy is quantized and inversely proportional to the square of the size (L) of the NM. This effect can be advantageous in many applications including light emitting diodes, single electron transistors, lasers, and others.[21] Yet, this confinement effect is particularly useful in photocatalysis where the bandgap can be tuned to reach a certain oxidation or reduction potential (Figure 1.4).[22] A better match between the redox potential of the SC and the substrate will unfold in the increase of the thermodynamic driving force and the rate for interfacial charge transfer as predicted by Marcus theory.[23]

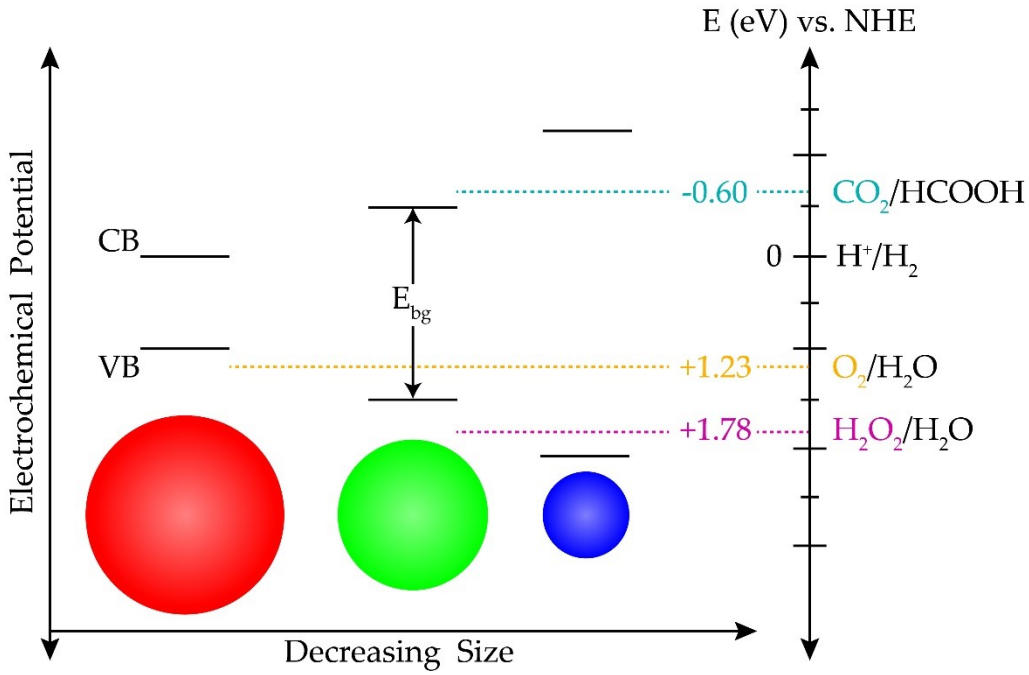

Figure 1.4 Exploiting quantum confinement in photocatalysis. An increase in the bandgap energy is observed as the size of the NM decreases due to the quantization of momentum. This quantum confinement effect can be exploited to tailor the redox potential of the NM for a specific conversion. For instance, the smaller NM (blue) can oxidize H_2O_2 and O_2, and reduce CO_2, while the medium-sized NM (green) can only oxidize O_2.[22]

1.3.1.3- Charge Carrier Collection Pathways

The absorption of a photon by the SC creates an exciton (electron-hole pair). Once separated, these charges have a predetermined mobility and lifetime within the material and their values will depend on the nature of both the material and the charge. Inside the material, there are two main driving forces acting upon the movement of these charges: the electrostatic potential that acts on the charge, and the electrochemical potential that acts on their quantity.[24] The distance that a charge will travel within the material, taking these forces into consideration, is defined by the mean free diffusion length L:

$$L^2 = qD\tau \qquad \textbf{Eq. 1.2}$$

where q is the dimensionality constant (q = 2, 4, 6 for one-, two-, or three-dimensional diffusion), D is the carrier diffusion constant, and τ is the charge carrier lifetime. The concentration of carriers can be manipulated by doping which will directly affect the lifetime and diffusion length of the carrier. Therefore, one must be aware of all these factors that come into play when computing L for engineering devices because the optimal thickness for charge carrier extraction will be dictated by L. The ideal thickness to maximize the performance of SCs for solar energy conversion should be of the same magnitude as the L for electrons and holes.[25]

1.3.1.4- Absorption of Photons/Light Distribution

The Beer-Lambert law determines the probability of absorbing a photon by a material. This probability is defined by the absorption coefficient α, which is proportional to the density of unoccupied states in the conduction band for electron generation.[24] Additionally, a factor

that will also limit the photon absorption is the light penetration depth of a material. This penetration depth is a measure of the intensity of the light within the material and is given by $x = 1/\alpha$. Thus, at a distance "x" from the surface the light intensity will be attenuated by a factor of $1/\alpha$. In this regard, the optimal thickness to maximize photon absorption should be > 2.3 times the value of $1/\alpha$.[1] In addition, the light is scattered to a higher extent in NMs and therefore distributed more efficiently throughout the material avoiding reflection losses.

1.3.2 Disadvantages of Nanoscaling in PEC Devices

1.3.2.1- Surface Recombination

The surface of NMs is usually where most defects are found due to crystal discontinuity (*i.e.* dangling bonds).[24] These defects create energy levels within the bandgap that act as recombination centers for the charge carriers. Additional recombination pathways include the tunneling of electrons through the depletion layer barrier and undesired reactions at the solid-liquid interface. Though, passivating the surface to reduce the surface defects of NMs is a viable option to decrease charge recombination.[26]

1.3.2.2- Smaller Depletion Layer

Due to the size of NMs, it is challenging to achieve an effective depletion layer. This becomes almost unfeasible at the lower nanosized-regime (~10 nm) because the depletion layer would need to be of the same dimensions or even larger than the size of the material. As previously mentioned (Figure 1.2), one of the main benefits of generating a depletion layer is the creation of a Schottky-like junction that rectifies the charge transfer from or into the SC. If there is no depletion layer, the conduction and valence bands will be flat, increasing the back recombination at the surface, and lowering the efficiency of charge transfer.[27]

1.4 Photosensitizers

Photosensitizers can be used to ensure visible light harvesting in wide-bandgap SC systems. Devices with a semiconductor|photosensitizer interface are inspired by the processes of photosynthesis in nature. The efficiency of this process is based on an energetic alignment that is thermodynamically favored for downhill electron transfer reactions. Furthermore, it avoids electron back recombination due to the separation of charges in space. This favorable electron transfer is mimicked in artificial systems where the photosensitizer creates an excited state followed by the injection of either an electron or a hole into the SC to separate the charges.[5] For the context of this thesis, and in the generation of solar fuels, a photosensitizer must absorb light in the visible-near-IR regions where the highest photon flux is found in the solar spectrum (Figure 1.5). The absorption cross-section of the target photosensitizer should also have some degree of tunability to make these materials versatile for different transformations. Parameters including the number of excited states possible, their lifetimes and quantum yields must be investigated in detail and optimized for maximum performance.

Lastly, the photosensitizer must have an appropriate excited state redox potential and should be photo- and chemically stable.

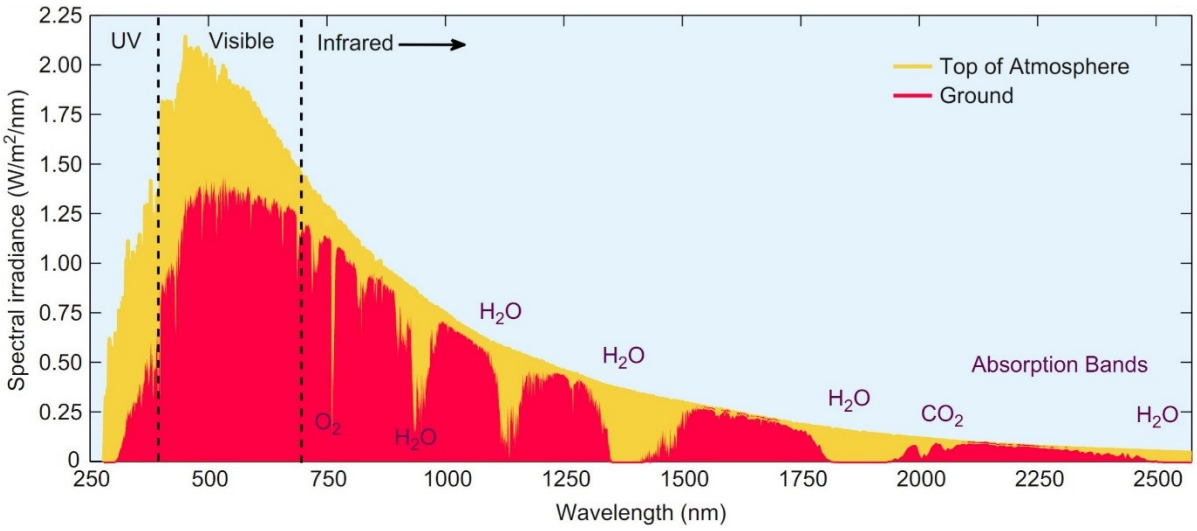

Figure 1.5 Photon flux in the solar spectrum as a function of wavelength. Reprinted with permission from ref. 28.

Extensive research has been done towards the discovery of new and efficient photosensitizers. For instance, there are examples of transition metal complexes, organic dyes, and plasmonic materials employed as photosensitizers on SCs.[29-31] However, some of these materials are toxic and their preparation suffers from poor cost-effectiveness. Therefore, the use of facilely prepared photosensitizers engineered from Earth-abundant elements is paramount to achieve sustainability.

1.4.1 Carbon-Based Nanomaterial Photosensitizers

Carbon-based NMs have emerged as a new class of photosensitizers for solar-to-chemical energy conversion. These materials can be synthesized through two approaches: top-

down and bottom-up. The former synthetic route makes use of techniques including electrochemical etching,[32] laser ablation,[33] and arc-discharge[34] in order to exfoliate a bulk carbon source (*i.e.* coal[35] or candle soot[36]). This approach generates nanometer-sized carbon particles with varying degrees of crystallinity. Conversely, the bottom-up route employs small building blocks such as amino acids[37] or polymers[38] to form carbon NMs through microwave-assisted reactions,[37] hydrothermal synthesis,[39] and thermal decomposition.[40]

Although there are many multidimensional carbon NMs, carbon dots (CDs) have comparatively easier synthetic procedures and a higher degree of flexibility when it comes to the tailoring of their optical properties. Thus, the use of carbon-based NMs for photocatalytic purposes has been focused on CDs. These CDs are usually ~10 nm in size, and they are mainly composed of carbon, oxygen, and hydrogen, with the possibility of doping nitrogen, sulfur, and phosphorous into the structure. The elemental composition of the CDs can be varied according to the starting materials used for the synthesis and subsequent surface treatment steps. These materials are capable of absorbing light throughout the visible and NIR regions of the spectrum, making them promising candidates for solar energy conversion (Figure 1.6).[41] The absorption can also be tuned through doping and surface passivation.

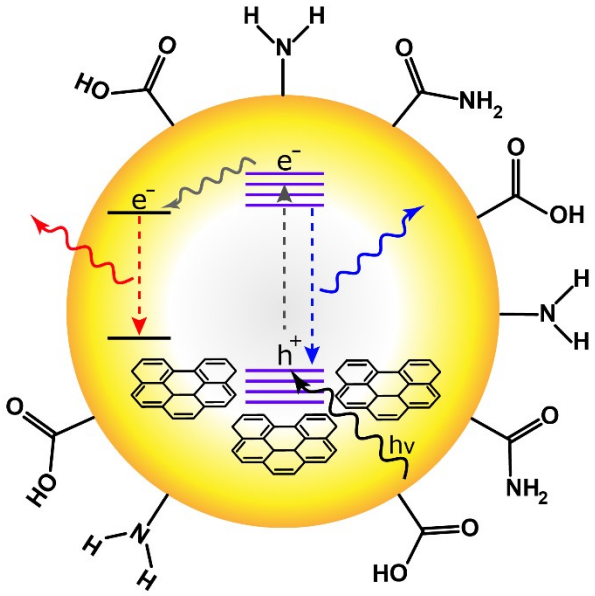

Figure 1.6 A dual absorbing/emitting CD with absorptions in the blue and red regions of the visible spectrum. The optical properties, redox potential, and surface functional groups can be modified by varying the starting materials, doping, or passivation procedures.

While CDs have many advantages over common precious metal-containing photosensitizers including their Earth-abundant element composition and simple syntheses, there are still some unresolved issues. These issues concern their compositional monodispersity, and the understanding of energy and electron transfer mechanisms that are strongly related to the tunability of their optical properties. Understanding their formation mechanism would provide insights on how to direct and access the reaction towards the production of highly tuned CDs. However, CDs are amorphous materials and their formation most likely requires a high number of cyclization and coupling reactions, complicating interpretation. Unlike CDs, chalcogenide SC nanocrystals (NCs, *i.e.* kesterite Cu_2ZnSnS_4) have a higher formation pathway accessibility owed to their known crystalline composition and nucleation theories in place.

1.4.2 Kesterite $Cu_2ZnSn(S,Se)_4$ (CZTS) NCs as Photosensitizers

Optimization of the preparation of colloidal inorganic NCs is of great interest because these materials can be employed as the active component in various technologies including light emitting diodes,[42] infrared sensors,[43] and in photocatalysis.[44] Following the discovery and use of $Cu(In,Ga)Se_2$ (CIGS) materials for solar energy conversion, the investigation of more sustainable NMs with similar properties became desirable. Hence, kesterite CZTS materials have garnered significant attention due to their elemental composition and optical properties. This material has a direct bandgap energy of 1.0-1.5 eV (827-1240 nm) with a high absorption coefficient (~10^4 cm^{-1}).[45] The synthesis of bulk kesterite CZTS is straightforward and can be done with high reproducibility. However, the production of NCs is non-trivial due to the possible formation of undesired binary (Cu_2S, SnS, and ZnS), ternary (Cu_2SnS_3), and quaternary (stannite and wurtzite, figure 1.7) CZTS phases. In seminal work, Nistche *et al.* demonstrated the production of stannite CZTS NCs through an iodine vapour transfer method.[46] After this report, a number of synthetic methodologies have been used to produce kesterite CZTS NCs including thermal evaporation,[47] sulfurization of precursors,[48] electrochemical deposition,[49] and solution-based methods.[50] The biggest challenge in the synthesis of this material is the generation of pure kesterite CZTS phase samples with narrow size distributions.

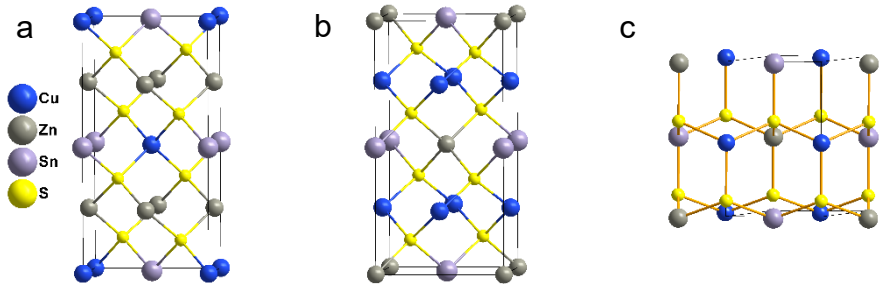

Figure 1.7 CZTS unit cell structures for a) kesterite, b) stannite, and c) wurtzite.

Control over the synthetic pathway of these NCs is one key to tailor their properties and catalytic efficiency given the strong correlation between structure and function.[51] In order to obtain synthetic control, however; there must be a fundamental understanding of the underlying mechanisms of nucleation and growth. Even though classical theories for the nucleation and growth of colloids do a fair job at explaining one-step growth mechanisms, they are often incapable of accounting for more complicated multi-step pathways. These pathways usually occur through the formation of metastable intermediate species. For instance, Gary *et al.* demonstrated that the formation of InP quantum dots happens through the generation of a kinetically stable "magic-sized" cluster.[52] Therefore, understanding how these metastable intermediates form and evolve is as important as the reactivity of the precursors in order to control and direct the synthesis of NCs.

1.4.3 Kinetics and Mechanisms of Nanocrystal Nucleation and Growth

The current state of NC synthesis has room for improvement in order to meet the control required to tailor their elemental composition and size dispersity. The use of empirical methods to achieve more synthetic control was the rule for many years until the LaMer nucleation and growth mechanism (classical nucleation theory or CNT), and Ostwald ripening (OR) were articulated.[53-54] To date, mechanistic studies on the nucleation and growth of NCs are scarce even though these mechanisms started garnering attention during the mid 1990s.[55] These studies have relied on both LaMer and OR pathways to make sense of the formation process. In the former, the nucleation is separated from the growth period by a burst-nucleation event while the latter explains how bigger crystals grow at the expense of smaller ones that dissolve due to surface energy considerations. More recent studies have observed other types of growth through NC aggregation and coalescence (non-classical behavior).[56-58] Therefore,

the understanding of all the underlying formation mechanisms at play is paramount to achieve better synthetic control towards the colloidal synthesis of inorganic NCs. This section will provide a brief overview of the most typical formation mechanisms (classical vs. non-classical) identified in such syntheses (Figure 1.8).

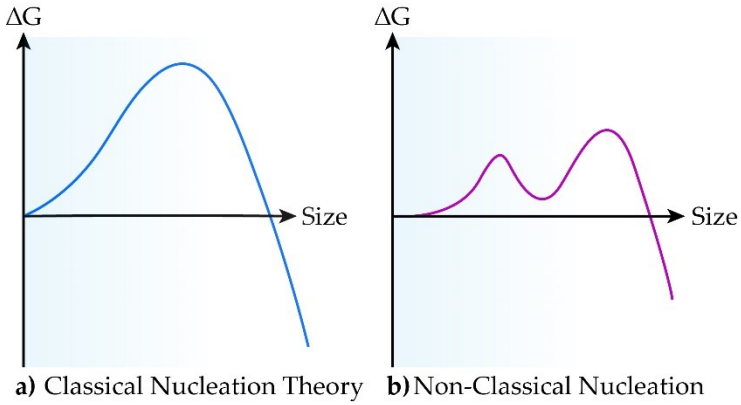

Figure 1.8 Free energy diagrams for CNT (a) and non-classical nucleation (b). These plots show how the free energy of the NCs changes as a function of increasing size. There is a large thermodynamic energy barrier in (a), while (b) provides an alternative route with lower energy barriers and local minima as the NC grows.

1.4.3.1- Classical Nucleation Theory (CNT)

The LaMer mechanism predicts the minimum size for thermodynamic stability and provides information about the kinetics of the process (Eq. 1.3) where the nucleation rate (j_n, number of nuclei formed per unit time and volume) relates to the temperature (T), the monomer diffusion constant (D), the monomer concentration ([M]), the monomer solubility limit ($[M]_0$), and the supersaturation level (S, Eq. 1.4).[51] The other constants include the molar (V_M) and molecular (v_0) volume of the NC, the surface tension (γ), and the gas constant (R).

$$j_n = \frac{2D}{v_o^{\frac{5}{3}}} \exp\left[-\frac{16\pi\gamma^3 V_m^2}{3(RT)^3(\ln S)^2}\right] \qquad \textbf{Eq. 1.3}$$

$$S = \frac{[M]}{[M]_o} \qquad \textbf{Eq. 1.4}$$

This mechanism is dived into four phases (Figure 1.9). The first one includes the generation of solute building blocks from a chemical reaction between the precursors. The solute rapidly increases in concentration reaching supersaturation and passing through a threshold. This threshold has a high thermodynamic energy barrier because of the high surface-to-volume ratio, where nuclei start to form. This phase is referred to as a "burst nucleation" stage in which the thermodynamical energy barrier width is essential to achieve a narrow size distribution of NCs since it prevents the random formation of NC at any given radius below the critical size. The formation of nuclei denotes the start of phase (II) where the nuclei increase in concentration. Once a significant number of nuclei form and the concentration of solute decreases below the threshold, phase (III) starts and the nuclei begin to grow. Thus, this mechanism effectively separates nucleation (phase II) from growth (phase III). During phase (IV) OR is the main growth mechanism at play.

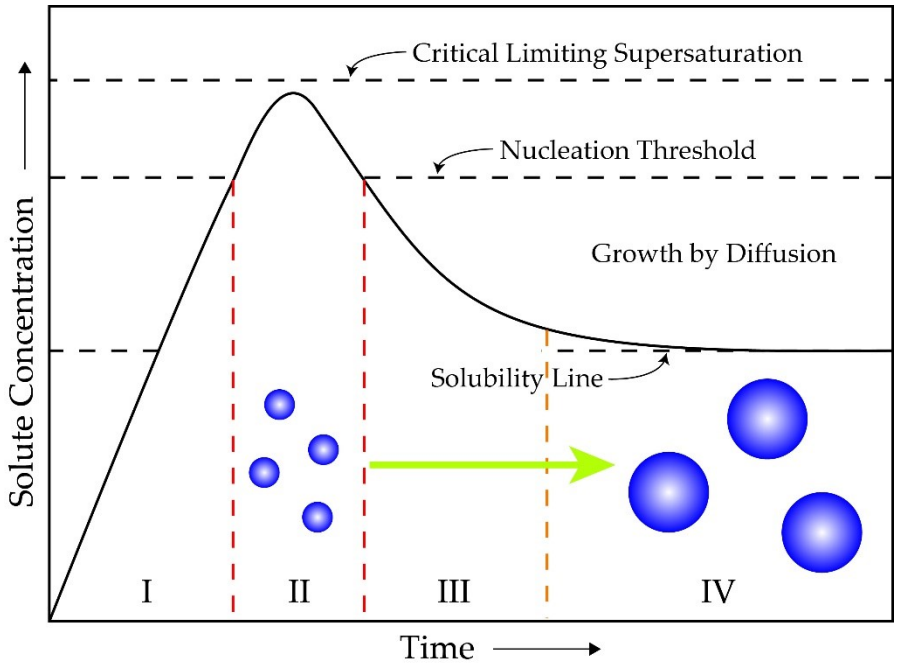

Figure 1.9 This scheme represents the growth process in CNT. The growth is governed by the concentration of solute (growth monomers/dimers/trimers etc.) in solution. In phase I, there is a rapid increase in the solute concentration until a critical concentration for the onset of nucleation or nucleation threshold is reached. At this point, the solute starts nucleating producing a "burst-nucleation" event (phase II). Then, the system enters phase III where the nuclei generated in the previous phase start to grow by attachment of the leftover solute. Finally, the NCs grow through OR governed by surface energy instability of smaller nuclei (phase IV).

In an effort to simplify CNT and its definition, the theory is founded on several assumptions that reduce its ability to address a variety of cases starting by the assumption that size is the only factor that will determine if the solute will nucleate or not.[59] The theory also assumes that nuclei are strictly spherical and uniform throughout their structure. Thus, the final NC must be identical in composition as the nuclei seeds. Surface tension effects are neglected, therefore, the impact of the solvent on the curvature of the NC is disregarded. In addition, the total number of nuclei is assumed to be settled instantaneously upon supersaturation. In such a case, the system would be presumed to follow steady-state kinetics where the rate of nucleation is time independent and the size distribution of the NCs would be extremely narrow, a phenomenon that is not observed in reality. Finally, nuclei growth is thought to happen through

the addition of one solute building block at a time where nuclei are assumed to be at rest, thus, all collisions between nuclei and NCs are ignored.

There are several experiments that corroborate the separation of nucleation and growth in time as predicted by CNT.[54, 60-61] Nonetheless, the limitations in the theory obscure the quantitative analysis of the number, size, and polydispersity of the final size distribution. Many factors interrupt and regulate the nucleation phase. For instance, the presence of additives that disrupt the concentration of solute can induce nucleation below the threshold.[51, 60, 62] Thus, understanding how additives (*i.e.* complexing agents, ionic strength, pH, etc.) affect the behavior of the solute prior to the nucleation phase can render the theory robust for the theoretical evaluation of homogeneous nucleation. In this respect, Sugimoto extended CNT with a powerful simplification that allows for better interpretation of experimental data.[63] From two differential equations concerning the concentration of solute and the nuclei population, Sugimoto concluded that the total number of nuclei formed during the burst is:

$$p_T^{\infty} = \frac{Q}{G} \qquad \textbf{Eq. 1.5}$$

where Q is the solute supply rate and G is the growth rate in solutes attached per nucleus. This equation predicts that the nucleation kinetics have no relationship with the total number of nuclei generated. It also predicts that there is an increasing linear correlation between Q and p_T^{∞}. This extension to CNT does a reasonable job explaining the nucleation behavior during the formation of AgCl clusters.[64] However, deviations from linearity have been observed when this equation has been implemented in other systems.[65-66] Chu, Owen and Peters further extended the work of Sugimoto to account for the solute concentration dependency (solute kinetics) on the size of nuclei.[67] Their analysis verified that the Q/G ratio almost completely

governs the number of nuclei generated as stated by Sugimoto, but also predicted that large critical nuclei coupled with slow growth kinetics can provoke a non-linear relationship in the relationship proposed by Sugimoto. Therefore, they proved the partial role of the nucleation kinetics over the time and supersaturation level at the nucleation burst, and that the growth rate G is in fact size dependent.

1.4.3.2- Non-Classical Nucleation and Growth

In CNT, the surface energy per area and the ΔG per volume are constant with respect to particle size, however, this is not the case for non-classical mechanisms. These non-classical nucleation routes are comprised of metastable intermediates (*i.e.* magic-sized and pre-nucleation clusters)[51, 62] that offer an alternate pathway to the high thermodynamic energy barrier from CNT as these intermediates possess lower surface energy. Hence, these intermediates create local energy minima towards solute supersaturation and subsequent nucleation that lowers the effective energy barrier for nucleation allowing the solute building blocks to form nuclei at a lower concentration to that predicted by CNT (Figure 1.8). The formation of these metastable clusters has been observed in numerous syntheses. For instance, the formation of magic-sized CdSe clusters as a metastable intermediate in the synthesis of CdSe nanorods was clearly demonstrated by Jiang *et al*.[62] Recently, Green *et al*. showed the formation of a pre-nucleation cluster in the synthesis of PbS NCs.[51] The formation of these clusters was controlled by the addition of different amines in order to tailor the size dispersity of the NCs. This highlights the shortcomings of CNT when it comes to the prediction of multi-step nucleation processes. CNT allows the estimation of the critical size for the onset of nucleation, but it fails in evaluating the routes leading to the formation of nuclei. Moreover,

the only precedent that dictates if the solute building blocks will become nuclei or not is size, which is a substantial weakness in the theory.

There are multiple ways for nuclei to grow after achieving thermodynamic equilibrium. In a seminal study, Zheng *et al*. demonstrated that platinum NCs have two growth mechanisms: simple monomer attachment and particle coalescence (Figure 1.10).[56] The smaller NCs have larger surface area to volume ratios as well as higher surface energies, mobility, and collision frequency, thus they were more likely to coalesce compared to larger NCs. Following this study, many groups delved into the investigation of growth mechanisms in the colloidal synthesis of inorganic NCs.[68-70] The different growth mechanisms include aggregative growth, oriented attachment, and OR.

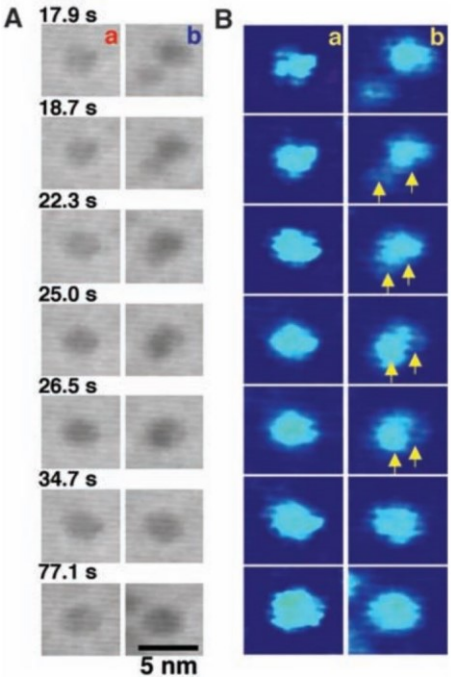

Figure 1.10 A) Captures from a TEM video displaying the growth of Pt NCs by monomer addition (a) and coalescence (b); B) Enlarged (colored) images from A. The yellow arrows in (b) point out the coalescence process where a NC dissolves and recrystallizes on the adjacent NC reprinted with permission from ref. 56.

Aggregative Growth: The early stages of this mechanism can be properly described by CNT followed by aggregative considerations (Figure 1.11). The second induction period shown on this figure corresponds to the growth of NCs by aggregative nucleation, while the third period illustrates the possibility for OR. Aggregative growth is governed by kinetic factors instead of thermodynamic ones. For instance, we know from CNT that nuclei with smaller size than the critical value for surface stability tend to dissolve. Nevertheless, if the collision frequency of the nuclei is higher than their dissolution rate, then, there is the chance for two or more nuclei to collide and form a larger and more stable NC. This type of growth would abruptly deviate from a classical behavior. In fact, this growth mechanism can be thought of as a tunneling-like process where the NCs 'tunnel' through a free energy barrier even in a low saturation regime.[71]

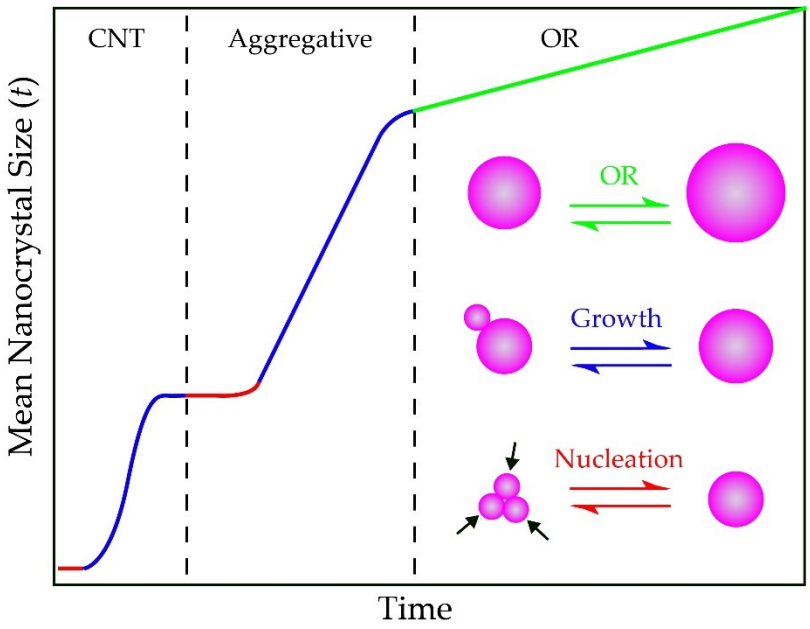

Figure 1.11 This scheme depicts the three different growth mechanisms discussed in this section. All mechanism could overlap in time to a certain extent (not shown here). Both CNT and aggregative growth have a kinetic profile that fluctuates in time. Conversely, OR shows a steady growth (adapted from ref. 53).

Oriented Attachment: Although this mechanism falls within aggregative growth, its kinetics have been widely studied. This type of growth occurs when two nuclei collide with their crystallographic phases aligning or rearranging in such a way causing an attachment and merging of the nuclei into a single-phased NC (Figure 1.12). Huang *et al*. found that the oriented attachment growth kinetics of ZnS NCs could be modeled taking into consideration the mean diameter (*D*) as a function of time (*t*) and the rate constant for oriented attachment (k_1) (Eq. 1.6).[72]

$$D = \frac{D_0\left((2)^{\frac{1}{3}} k_1 t + 1\right)}{k_1 t + 1} \qquad \textbf{Eq. 1.6}$$

This model was refined by Zhang *et al*. in a follow up publication[73] and further developed by Penn *et al*.[74] In addition, Burrows *et al*. investigated the effects of ionic strength in the kinetics for oriented attachment of NCs.[75] It was found that increasing the ionic strength of the solution provoked a linear increase in the rate constant for oriented attachment. This study demonstrates the pivotal effect of additives to obtain better synthetic control over the growth of NCs.

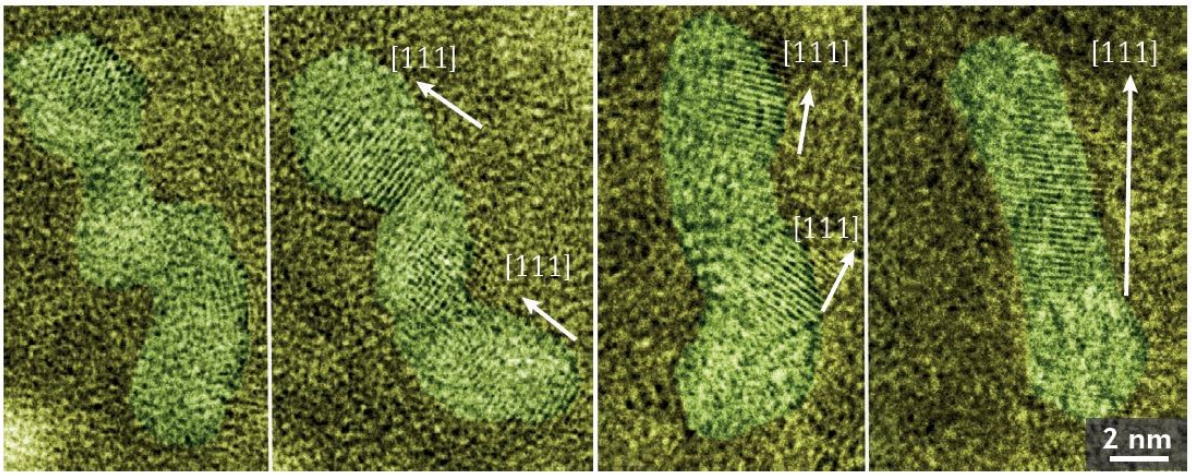

Figure 1.12 TEM images depicting the alignment of Pt_3Fe NCs over time. At first, the NCs are completely misaligned after the collision, however; the redistribution of atoms within the NCs brings the aggregate from a multi-phased amorphous shape to a single-phased nanorod (adapted and reprinted with permission from ref. 76).

Ostwald Ripening: This growth mechanism describes how bigger NCs grow at the expense of smaller ones that dissolve and "feed" bigger crystals. In the standard model for OR, the mean NC volume increases linearly in time. Also, this is not a process that involves nucleation and as a result, it requires an induction period for the generation of NCs that can further grow through OR. Therefore, the growth function for conventional OR must yield a unimodal size distribution that will constantly shift to larger size values while broadening throughout the growth. Special cases can produce a bimodal distribution,[77] however; they will not be discussed here.

All three growth mechanisms CNT, non-classical growth–aggregative, and OR (Figure 1.11) can overlap in time and are not restricted to occur in a sequential fashion. This is another factor to consider when trying to unravel the mechanisms of nucleation and growth in the colloidal synthesis of inorganic NCs. As detailed herein, many advances have been made to further understand each of the classical and non-classical formation mechanisms through

kinetic studies. These theory developments will allow the methodical control of the final NC size distribution.

1.5 Goals and Scope

Throughout the next chapters, the use of nanostructured ZnO MOx SC and carbon-based photosensitizers for solar-to-chemical energy conversion will be discussed. In addition, the formation mechanism of kesterite NCs is evaluated, and the composition and size distribution are discussed in detail.

Specifically, Chapter 2 presents the growth of ZnO NWs on a conductive substrate which are further functionalized with blue-absorbing CDs. This heterogenous photocatalyst is used to drive organic transformations under visible light irradiation. The energetics of the device are studied in detail to provide insight about the electron transfer steps throughout the reaction. Consecutively, Chapter 3 explores the possible nucleation and growth mechanism in the hot-injection and microwave syntheses of kesterite NCs. A combination of CNT and non-classical growth is proposed as the formation mechanism for this quaternary structure.

Chapter 2 Carbon Dot-Sensitized Photoanodes for Visible Light-Driven Organic Transformations

Coupling reactions that involve heteroaromatic compounds and amines are a key component in the synthesis of organic SCs,[78-79] anion exchange membrane fuel cells,[80] and pharmaceuticals.[81] Photocatalytic devices engineered from Earth-abundant elements that can drive such reactions are an inexpensive alternative to traditional methods in synthetic organic chemistry and, therefore, highly desired. Heterogeneous photocatalytic surfaces such as nanostructured semiconducting MOx, although more difficult to study with respect to mechanism elucidation are typically stable and readily recyclable.[82] Furthermore, heterogeneous photoredox systems are comparable in performance with molecular ones; however, they have the advantage of being easily extractable from solution.[83] For these catalysts to be industrially viable, they must be simple and economical to prepare/operate relative to well-established synthetic methodologies (e.g. palladium mediated cross-coupling reactions).[84-86] Many photocatalytic mechanisms in organic synthesis leverage the inherent reactivity of oxygen species and other radicals.[87-88] For instance, Stache *et al*. have activated C-O bonds through a photocatalytic mechanism using $[Ir(dFMeppy)_2(dtbbpy)][PF_6]$ [dFMeppy = 2-(2,4-difluorophenyl)-5-methylpyridine, dtbbpy = 4,4′-di-tert-butyl-2,2′-bipyridine] via the generation of phosphoranyl radicals.[89] In another illustrative example, Cai *et al.* have made use of a graphitic-C_3N_4 photocatalyst to generate α-tertiary and α-secondary aminoalkyl radicals, in high yield, as precursors for different organic transformations.[90] Nonetheless, these radical driven reactions have some drawbacks, including long reaction times, sensitizer photobleaching, unwanted by-products, and mass transfer limitations between the radical and the substrate.[91-92] Camussi *et al.*, showed how a g-C_3N_4 photocatalyst can

sensitize $^1O_2$ to drive cycloaddition reactions albeit with low chemoselectivity due to two proposed mechanisms with which $^1O_2$ could react with the substrates.[93] Acknowledging these limitations, and by employing lessons learned from the design of materials for solar fuels generation, we envisioned that it should be possible to drive clean and chemoselective coupling reactions with a photoelectrode (acting as a heterogeneous photocatalyst) in an air-free environment to generate valuable products in high yield.

Many semiconducting materials have been explored to drive solar energy conversion including metal oxides,[94] sulfides,[95] and organic polymers.[96] Few, if any, of these materials fully meet the requirements to maximize the absorption of sunlight (e.g. narrow bandgap, low cost, long-term stability, and minimal pathways for charge recombination).[97] Zinc oxide nanowires (NWs) have emerged as promising materials for these photoelectrochemical applications because of their shortened charge carrier collection pathways, large surface area, and charge-steering capabilities.[1, 98] However, ZnO has a wide bandgap (3.37 eV) limiting the absorption of visible light and subsequently, the quantum efficiency.[99] To increase the incident photon to converted electron ratio, developing new ways of sensitizing ZnO NMs to absorb wavelengths in the visible portion of the solar spectrum is of particular interest.

Efforts have been devoted to the sensitization of ZnO NWs through doping, attachment of plasmonic structures, and dye and quantum dot sensitization.[100-102] Kadi *et al.* have previously doped ZnO NWs with fluorine in order to decrease the bandgap energy of the material and to further employ the resulting device as a heterogeneous catalyst for the photodegradation of malachite green dye using visible light.[103] Guo *et al*. have sensitized ZnO NWs with graphene quantum dots to perform water splitting,[104] and Lee *et al.* have coupled a ruthenium-based dye to ZnO in order to increase the absorption of light throughout the visible

spectrum (in a strategy analogous to those employed in dye sensitized solar cells).[105] Although these sensitization methods vary in their degree of efficiency, some of the aforementioned sensitizers are costly while others make use of heavy metals which are significantly harder to recycle.[106]

Recently, CDs have emerged as candidates for various applications due to their low cost and chemical toxicity, optical properties, and stability.[107-109] The implementation of CDs for light-conversion applications as a new generation of photosensitizers has also increased as a result of their high photostability and tunable light absorption.[110-111] Moreover, these NMs have shown photocatalytic activity for the degradation of organic contaminants, water splitting/hydrogen production, and the redox catalysis of different organic reactions to produce high value-added chemicals by visible light.[112-114] The latter has been relatively underexplored with greater focus on the degradation of organic dyes likely owing to the logistical simplicity regarding reaction monitoring and product isolation/characterization.[115-116] In a marriage of the two materials discussed (*vida supra*), we anticipate that the surface functionalization of ZnO NWs with CDs will open new avenues for the engineering and development of "green" nanohybrid devices.[104, 117-118] To date, the design of such devices is partially hindered by fast electron-hole recombination kinetics,[119] device stability,[120] low quantum yields,[121] and a general lack of understanding about the molecular processes occurring at the interface of such heterogeneous photoelectrodes.[116]

Here, we report the fabrication of a metal oxide-carbon dot nanohybrid photoelectrode for the photocatalytic α-heteroarylation of tertiary amine 1-phenylpyrrolidine (**1**) and the production of a high value-added benzylic amine pharmacophore (Figure 2.1) as well as offer insight into possible mechanisms of electron transfer between the photoelectrode and organic

substrate. The photoelectrode is formed via the growth of ZnO NWs on a fluorine-doped tin oxide (FTO) on glass substrate through a hydrothermal reaction and subsequent functionalization with previously unreported visible light absorbing carbon dots prepared from citric acid and propylenediamine (**PD2-CDs**) through attachment of anchoring surface groups on the **PD2-CDs**. The photoelectrodes prepared in this fashion exhibit an enhanced photocurrent under visible light irradiation and a further increase upon exposure to tertiary amines.

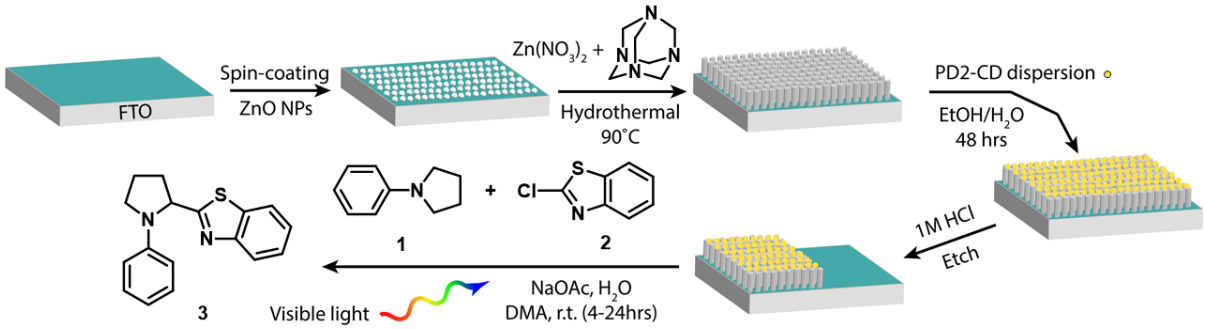

Figure 2.1 Fabrication protocol for the photoelectrodes described in this work along with the proposed reaction scheme for the α-heteroarylation of 1-phenylpyrrolidine (1) with 2-chlorobenzothiazole (2) via irradiation of a carbon dot functionalized ZnO NW photoelectrode.

2.1 Experimental

2.1.1 Materials

Zinc chloride ($ZnCl_2$), zinc nitrate hexahydrate [$Zn(NO_3)_2 \cdot 6H_2O$], hexamethylenetetramine (HMTA), linoleic acid, sodium hydroxide (NaOH), citric acid, propylenediamine (PD2), glutathione, formamide, and fluorine doped tin oxide (FTO) on glass were purchased from Sigma-Aldrich and used as received. Tetrabutylammonium hexafluorophosphate ($TBAPF_6$) was purchased from Tokyo Chemical Industry Co. (TCI) and recrystallized three times from ethanol (99%) before use. 1-Phenylpyrrolidine (**1**) and 2-chlorobenzothiazole (**2**) were purchased from Alfa Aesar and used without further purification. *N,N*-Dimethylacetamide (DMA) was purchased from Fisher Scientific and used as received.

2.1.2 General Procedures

Transmission electron microscopy (TEM) images were collected using a benchtop LVEM5 microscope from Delong Instruments (Brno, Czech Republic) operating at 5 kV for the ZnO NPs and a JEM-2100F (Jeol Ltd) analytical electron microscope operating under 200 kV for the **PD2-CDs**. Three 2 µL aliquots of a 500 µg mL^{-1} ZnO NP dispersion in 95% ethanol were pipetted onto a Cu-300HD grid (Pacific Grid-Tech). **PD2-CDs** were also casted onto Cu-300HD grids by immersing the grid in a 1 mg mL^{-1} dispersion in 18 MΩ water. Images were processed using Fiji imaging software where the ZnO NP size was determined (average of ca. 200 particles). The morphology of the ZnO NWs was characterized through scanning electron microscopy (SEM) using a FEI Quanta 3D FEG Dual Beam instrument working at 5 kV. The films were sputter-coated with Pt before all measurements.

A K-Alpha X-ray photoelectron spectrometer (Thermo Scientific) in standard lens mode was used to obtain the XPS spectra of the PD2-CDs. A 400 mm spot size was analyzed using a CAE analyser with a 50.0 eV pass energy and a 0.100 eV energy step. The measurements were performed in triplicate with 10 runs for each scan. The average of the triplicates was used to plot both the survey and the HR spectra.

Powder X-ray diffraction (PXRD) measurements were performed using a 2nd Gen D2 Phaser X-ray diffractometer with monochromatized Cu Kα radiation with a nickel filter (Bruker AXS). The X-ray source was set to a power of 30 kV and 10 mA in a continuous PSD fast scan mode. Diffraction patterns were recorded in 2θ ranging from 20 to 70° with a step increment of 0.05° and scan speed of 1 s $step^{-1}$ with a PSD opening of 4.7970°. The data analysis was performed with XPert Highscore software.

Attenuated Total Reflectance (FTIR-ATR) analysis was performed using a Thermo Scientific Nicolet iS5 equipped with an iD5 ATR accessory. The spectra were acquired in 64 scans, with a resolution of 0.4 cm^{-1}, a gain of 1, an optical velocity of 0.4747 cm s^{-1}, and an aperture setting of 100. The Omic 9 software package was used to process the raw data. UV-Visible absorption spectra were obtained from 200-800 nm using a Cary 5000 Series UV-Vis-NIR Spectrophotometer (Agilent Technologies) and a 1 cm quartz cuvette or a film sample holder. A 5.0 nm bandwidth with a wavelength changeover at 350 nm and a scan speed of 600 nm s^{-1} with a resolution of 1 nm were used for analysis. Diffuse reflectance spectroscopy (DRS) spectra were collected from 350-800 nm using a Cary 6000 Series UV-Vis-NIR spectrophotometer (Agilent Technologies) coupled with an integrating sphere. A 5.0 nm bandwidth with a wavelength changeover at 350 nm and a scan speed of 600 nm s^{-1} with a resolution of 1 nm were used for analysis. Photoelectrode thickness was analyzed using a Dektak XT contact profilometer with a stylus force of 10 mg.

Electrochemical measurements were performed on a WaveDriver 20 Integrated Bipotentiostat/Galvanostat workstation (Pine Research Instrumentation, Inc.). A three-electrode system was employed to measure the photoelectrochemical response of ZnO NW films as a working electrode (WE) with a platinum wire as a counter electrode (CE) and a Ag/AgCl (3 M KCl) reference electrode (RE) in 0.1 M KOH solution. All potentials were measured against the reference electrode. ZnO films without functionalization were irradiated with a 4 W UV lamp (λ_{ex} = 365 nm) at a distance of ca. 10 cm. The electrochemical properties of the **PD2-CDs** were determined using a three-electrode system by drop-casting **PD2-CDs** from 95% ethanol onto a platinum button WE (2 mm diameter) with a platinum wire as a CE

and a Ag wire pseudo-reference electrode in 0.1 M $TBAPF_6$ in acetonitrile. All potentials were referenced against ferrocene as an internal standard.

2.1.3 Photocatalysis

All photocatalysis measurements were performed in a homemade photoreactor setup. In a representative procedure, a glass vessel loaded with 1-phenylpyrrolidine (**1**, 276 μL, 1.875 mmol), 2-chlorobenzothiazole (**2**, 163 μL, 1.25 mmol), sodium acetate (205 mg, 1 mmol), H_2O (18 MΩ, 225 μL, 2.5 mmol) and a stir bar was sparged with argon for 10 min. DMA (5 mL) was transferred into a vial under argon and sonicated for 45 min while bubbling argon. Subsequently, the solvent was transferred to the reaction vessel with a three-electrode setup (the film acting as the WE), to monitor the photocurrent produced over the course of the reaction. This vessel was placed on a stir plate and inside a homebuilt photoreactor with four white light LEDs (Cree XP-G3 Cool White) for 4–24 hrs. A fan was placed on top of the reactor to maintain the reaction temperature at ca. 23 °C (see Appendix, Figure A1). The product of the reaction was isolated and purified as described in the Supporting Information.

2.1.4 Synthesis of Zinc Oxide Nanowires (ZnO NWs)

NWs were synthesized from zinc nitrate hexahydrate and HMTA in a hydrothermal reaction by a procedure optimized in our lab (see Appendix). Five fluorine-doped tin oxide (FTO) on glass substrates (ca. 2 cm × 1 cm) were first cleaned by immersing them separately in soapy water (10 min), distilled water (10 min), and 95% ethanol (10 min) under sonication. The cleaned substrates were dried in an oven at 80 °C for at least 4 hours prior to deposition and then were spin-coated (3×, 1500 rpm, 2 s) with two drops of a dispersion of ZnO NPs (see Appendix) in 95% ethanol (1 mg mL^{-1}). After the casting process, the slides were placed

upside down inside a centrifuge tube for the addition of the growing solution. An aliquot of aqueous $Zn(NO_3)_2 \cdot 6H_2O$ solution (17 mL, 0.13 M) was combined with aqueous HMTA (13 mL, 0.2 M) and transferred to the centrifuge tube containing the ZnO NP substrates. The tube was left in an oven at 90 °C for 3 hrs for the NWs to grow on the slides. Then, the sides were rinsed thoroughly with distilled water and 95% ethanol and left to air dry for further experiments.

2.1.5 Carbon Dot Synthesis (PD2-CDs)

The **PD2-CDs** were synthesized through the hydrothermal reaction of citric acid and propylenediamine (PD2). Citric acid (0.960 g, 500 mmol) and PD2 (0.320 mL, 375 mmol) were added to 10 mL of water in a hydrothermal reactor. The solution was heated to 210 °C for a period of 4 hrs with stirring at 300 rpm. The product was a dark brown solution that was subjected to dialysis for 5 days in Milli-Q water, using a 1 kDa MWCO dialysis bag (Spectra/Por®6 RC – Spectrum Laboratories), and changing the water every 24 hrs to remove the unreacted material. Then, the sample was placed in an oven at 70 °C overnight to concentrate it to ~5 mL, followed by three organic washes with 40 mL of acetone (99%) to further purify the **PD2-CDs**. Once the **PD2-CD** solution was concentrated, 40 mL of acetone was added, the sample was vortexed for 30 s and centrifuged at room temperature at 10 kG for 10 min. The supernatant was discarded, and two more acetone washes were performed on the sample. It is important to note that the fluorescence of the supernatant was evaluated after every wash to make sure the sample was free from any impurities and unreacted fluorophores. By the third wash the fluorescence of the supernatant was insignificant, meaning that the product is pure. The purified product was dried in an oven at 80 °C overnight, crushed into a fine powder and dispersed in water or 95% ethanol for further experiments.

2.1.6 ZnO NW|PD2-CD Film Preparation

The **ZnO NW|PD2-CD** heterostructures were prepared by a simple reaction in ethanolic solution. In a typical procedure, two films of ZnO NWs were placed in a 50 mL beaker, immersed in a dispersion of **PD2-CDs** (7 mL, 150 μL mL^{-1}), and covered by aluminum foil. The dispersion of **PD2-CDs** was prepared by adding 525 μL of a 2 mg mL^{-1} dispersion of **PD2-CDs** in Milli-Q water (18 MΩ) to 6.5 mL of 95% ethanol. The films were left in this dispersion under constant stirring for a period of 48 hrs for the **PD2-CDs** to attach and cover the whole surface. Additionally, after the reaction period the films were rinsed thoroughly with 95% ethanol to remove any unattached **PD2-CDs** and left to air dry. Finally, one edge of the film was immersed in a 1 M HCl solution to etch and normalize the active surface of the film to ca. 1.5 cm^2. The films were rinsed with 95% ethanol and left to air dry in the dark prior to further analysis.

2.2 Results and Discussion

The ZnO NWs were prepared by spin-coating a ZnO NP dispersion onto an FTO on glass slide, followed by hydrothermal reaction of $Zn(NO_3)_2 \cdot 6H_2O$ and HMTA at 90 °C. From transmission electron microscopy (TEM) investigations (Figure 2.2a), the ZnO NPs used as seeds for nanowire growth are spherical and monodisperse with an average size of 32 ± 4.7 nm. The crystallinity of the NPs was evaluated through powder X-ray diffraction (PXRD) which shows crystalline reflections for the (100), (002), (101), (102), (110), (103), and (112) planes (Figure A2) in agreement with previously reported values.[122] Scanning electron microscopy (SEM) of the as-grown ZnO NWs shows highly oriented and tightly packed hexagonal wires with a calculated average diameter of 130 ± 28.2 nm (Figure 2.2b). These wires produce films of an average thickness of 1.3 µm as measured by profilometry. The PXRD pattern for the NWs (Figure 2.2c) displays characteristic peaks for wurtzite ZnO: (100), (101), and a prominent (002) signal corresponding to the preferred orientation of the nanowires on the surface.[123] The bandgap of this SC film was calculated to be 3.22 eV from the band edge of the diffuse reflectance spectrum (DRS; inset Figure 2.2c).

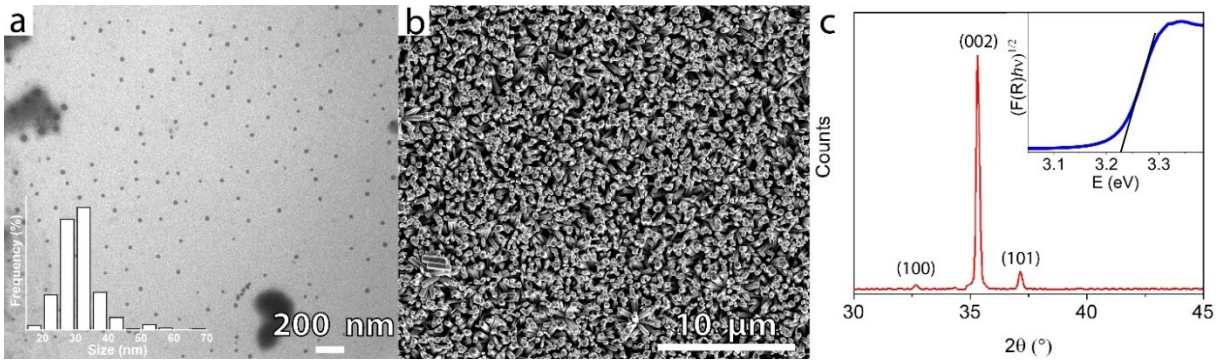

Figure 2.2 a) TEM micrograph of the ZnO NPs. b) SEM micrograph of the ZnO NWs grown on an FTO substrate. The image depicts highly oriented wires with hexagonal heads and a low degree of aggregation. c) PXRD spectrum for the ZnO NW films on FTO. The preferred orientation for the growth is observed through the (002) plane as this peak is significantly greater than the ones for the other phases. (c, inset) Diffuse reflectance spectrum plotted using the Kubelka-Munk function.

The **PD2-CD** photosensitizers were synthesized from citric acid and propylenediamine in a hydrothermal reaction effectively highlighting the low cost and simplicity of the synthesis of this class of NMs.[124-125] We expect these starting materials to yield CDs that are N-doped, where heteroatom doping in CDs is considered to be a form of passivation to enhance the optical properties of the material.[110, 126] The presence of amide groups in CDs has previously been shown to increase the quantum yield of emission in this family of nanoparticles.[127] TEM analysis (Figure 2.3a) of the prepared and purified **PD2-CDs** shows an average size of 10.7 ± 1.5 nm. PXRD analysis (Figure 2.3b) confirms the amorphous nature of the **PD2-CDs** and the X-ray photoelectron spectroscopy (XPS) survey scan (Figure 2.3c) shows three different binding energies: 285, 400, and 531 eV that correspond to C1s, N1s, and O1s, respectively. These data correlate with the expected CD elemental composition from citric acid and propylenediamine. The data extracted from high resolution XPS (HR-XPS) spectra were assigned to the respective bonds in the **PD2-CDs**, where the deconvolution for C1s (Figure A3a) shows the presence of C-C/C=C (284.3 eV), C-O (286.3 eV), and C-N/C=O (287.6 eV) bonds; for N1s (Figure A3b), the deconvolution shows two peaks corresponding to N-C/N-C (399.8 eV), and N-O (402.3 eV) bonds; and for O1s (Figure A3c) the spectra can be deconvoluted into two binding energies representing C=O (530.7 eV), and C-OH/C-O-C (531.8 eV) bonds. The elemental composition of the **PD2-CDs** was extracted from the HR-XPS by comparing the integrated peak areas for C, N and O and was found to be 71.95%, 11.61%, and 16.45%, respectively. The ability to optimize the optical properties of CDs based on the materials they are synthesized from to maximize the absorption of light in the visible part of the spectrum is of particular interest, and the absorption spectrum of the **PD2-CDs** (Figure 2.3d) in an aqueous dispersion shows a maximum absorption peak centered at 352 nm

and a wide shoulder that extends deep into the visible region (from ca. 380 to 550 nm). The maximum at λ_{abs} = 352 nm is attributed to a $\pi \rightarrow \pi^*$ transition, while the shoulder is assigned to the $n \rightarrow \pi^*$ transition from the aromatic sp^2 domains of the C=O and C=N bonds, respectively.[128] The Fourier transform infrared (FTIR) spectrum of the **PD2-CDs** (Figure 2.3e) shows bands between 3500-3000 cm^{-1} corresponding to -OH surface groups, as well as stretching modes at 2977 cm^{-1} for alkyl C-H groups, 1632 and 1532 cm^{-1} for amide and carboxyl C=O groups, 1556 cm^{-1} for amide C=N, 1364 cm^{-1} for the C-N, and 1213 cm^{-1} for acyl C-O (Table A1).

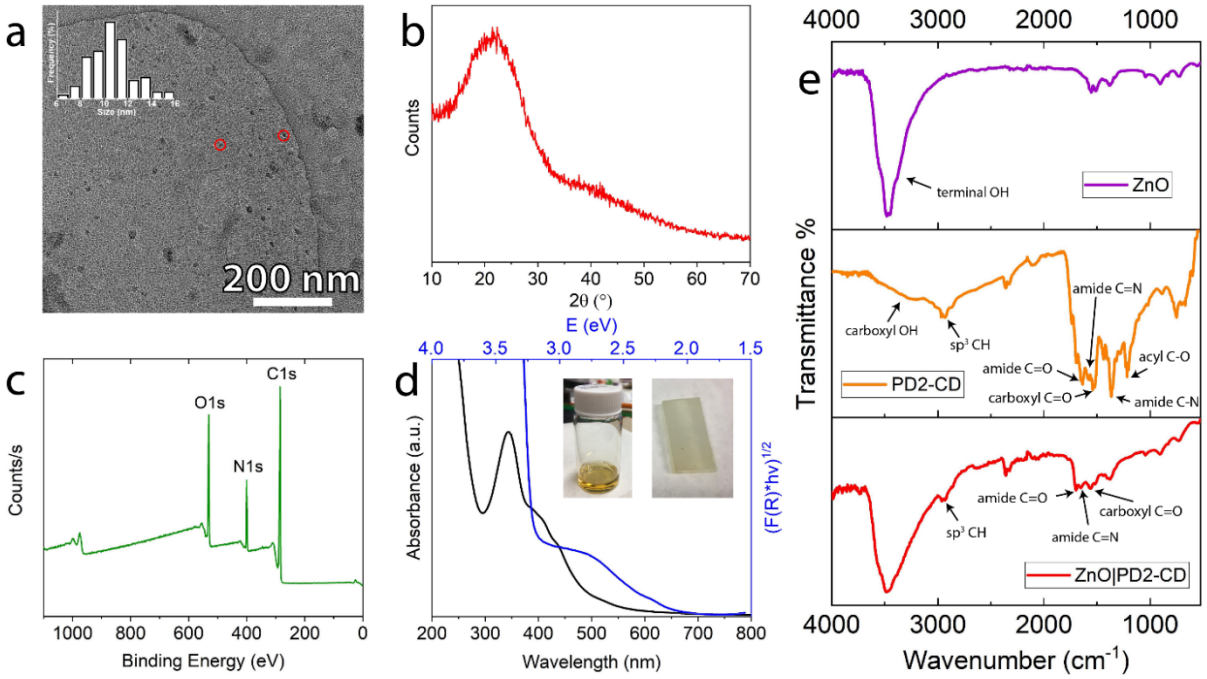

Figure 2.3 a) TEM spectrograph of the PD2-CDs with two representative carbon dots highlighted (red circles). b) PXRD diffractogram for the PD2-CDs in powder form, which confirms the amorphous nature of the material. c) XPS survey scan indicating the presence of carbon, nitrogen and oxygen. d) UV-vis (black trace) spectrum and Kubelka-Munk plot (blue trace) for PD2-CDs dispersed in water and the functionalized films, respectively. The Kubelka-Munk plot corroborates the presence of PD2-CDs on the films with a broad peak that extends from 2.0 to 2.75 eV. d, inset) Ethanolic solution of PD2-CDs used for film functionalization and a ZnO NW film after exposure to the PD2-CD solution. e) FTIR spectra for the ZnO NWs (top), PD2-CDs (middle), and ZnO NW|PD2-CD scraped from the substrate (bottom). The functionalized film displays bands for the alkyl -CH and amide bond stretches over the ZnO bands that further confirms the attachment of the PD2-CDs onto the films.

Attachment between the ZnO NWs and the **PD2-CDs** was achieved by immersing the NW films in an ethanolic dispersion of **PD2-CDs** for 48 hrs. After the attachment process the color of the films changed from white to pale orange (Figure 2.3d, inset). Optical characterization of the sensitized films by diffuse reflectance spectroscopy shows that the electronic properties of the pristine ZnO NWs are unaffected by the addition of the **PD2-CDs** as the bandgap absorption edge at 3.22 eV can still be observed (Figure 2.3d) while a significant increase in visible light absorption is observed, stemming from a broad band that extends from 2.0 to 2.75 eV. These values correlate to the optical bandgap values for the **PD2-CDs** in water (Figure 2.3d). In addition, diffuse reflectance FTIR spectroscopy (DRIFTS) confirms the presence of the **PD2-CDs** on the ZnO NWs where the stretch for the amide group can be distinguished at 1700 cm^{-1} (Figure A4). To determine the nature of the interaction between the **PD2-CDs** and ZnO NWs, FTIR spectroscopy on material scraped from the functionalized films (Figure 2.3e) was carried out. The broad band between 3600 to 3100 cm^{-1} is attributed to terminal -OH bond stretching, which becomes broader once the **PD2-CDs** are adsorbed onto the film. FTIR spectra for both the **PD2-CDs** alone and the **PD2-CDs** with the NWs show a band for the alkyl C-H stretch at 2971 and 2933 cm^{-1} confirming the presence of the **PD2-CDs** on the film. The band centered at 1562 cm^{-1}, assigned to the C=O stretch of the amide shifts from 1532 cm^{-1} in the free CDs. The band centered at 1378 cm^{-1} for the C-N bond also exhibits a shift from 1364 cm^{-1}. These fluctuations in the stretching vibrations can be correlated to the change in the dielectric environment between the aggregated **PD2-CDs** in the solid state and rigidified on ZnO.[129] The attachment of different functional groups to the surface of ZnO NMs has been well documented in the literature through experimental and computational methods.[130] Carboxyl groups usually have a tight binding mode to ZnO

according to computational studies where this functional group coordinates via two asymmetric bonds between the -COOH oxygens.[131-132] Likewise, -SH and -NH_2 groups are also known to bind to ZnO.[130]

Cyclic voltammetry was used to estimate the HOMO/LUMO energies of the **PD2-CDs** (Figure 2.4a). When the potential was scanned through the oxidative side, two oxidative waves were observed; a non-reversible wave with an onset value of E_{ox} = +1.1 V (all potentials reported versus NHE) and one with an onset potential of E_{ox} = +1.6 V. Conversely, once the reductive side of the cyclic voltammogram was analyzed, a wave with a reductive onset of E_{red} = −2.4 V was observed. These values suggest a HOMO-LUMO gap of 3.5 eV (352 nm) that correlates to the absorption peak from the UV-Vis of the **PD2-CDs** dispersed in water (λ_{max} = 342 nm).

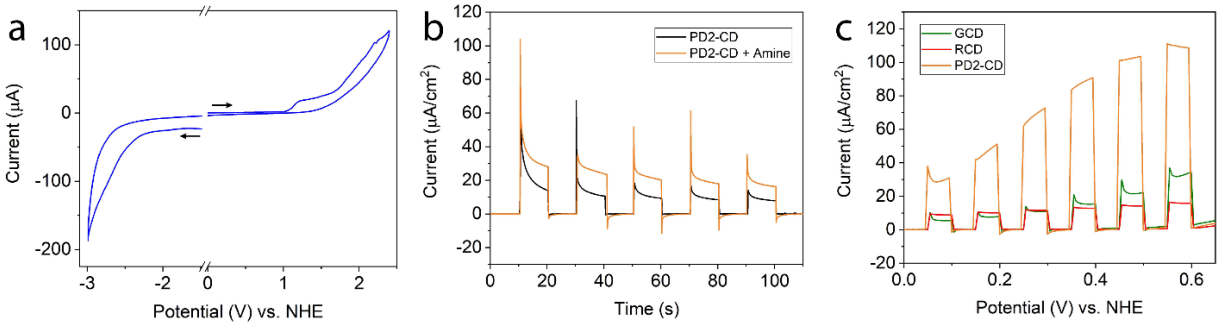

Figure 2.4 a) Cyclic voltammograms for the calculation of the HOMO and LUMO positions from both the non-reversible peak and the oxidative onset potential and from the reductive onset potential, respectively. b) Chronoamperograms of the chopped-light experiment with white LEDs on the films with (orange trace) and without (black trace) 1. c) Linear sweep voltammograms comparing the electrochemical behavior of different types of CDs (GCD and RCD) with the PD2-CDs used in this study (orange trace) upon 1-phenylpyrrolidine addition. RE: Ag wire; CE: Pt wire; WE: ZnO NW|PD2-CD film, 0.1 M TBAPF6 in dimethylformamide (Scan rate: 100 mV s−1).

The photocurrent of the nanostructured ZnO NW photoelectrode was first characterized using chronoamperometry (CA) in a three-electrode system before taking measurements on

the sensitized films to confirm the semiconducting properties of the composite material. These photocurrent measurements were performed under chopped UV light illumination (λ_{ex} = 365 nm) in a 0.1 M solution of KCl without any sacrificial agents (Figure A5). A current increase and a capacitive effect due to the build-up of charges at the solid-liquid interface was observed on irradiation. Chopped-light CA with no applied bias was also used to investigate the production of photocurrent over time upon white light irradiation of the **ZnO NW|PD2-CD** films (Figure 2.4b). There is a clear current increase on irradiation that suggests the injection of electrons from the excited state of the **PD2-CDs** into the conduction band of the ZnO NWs according to the proposed band alignment of the LUMO (−2.44 V) of the **PD2-CDs** and the literature value for the conduction band of ZnO (−0.3 V).[133] In this regard, the ZnO NWs are acting as a support and stabilizer of the reduced **PD2-CDs** and as a sink for reducing equivalents, harvesting electrons that could then be used in follow-on single electron transfer (SET) processes. The stability of the connection between the **PD2-CDs** and the NWs was evaluated by performing five chopped-light chronoamperometric experiments on a **ZnONW|PD2CD** film. Each experiment was performed in a fresh electrolyte solution and the photocurrent was recorded upon white light illumination (Figure A6). It was observed that the current density diminishes to 70% of its original value in the fifth solution and after being exposed to 25 on-off illumination cycles (Table A2). Thus, we conclude that the interaction between the NWs and the **PD2-CDs** must be of a reasonable strength for the **PD2-CDs** to inject electrons into ZnO, surviving multiple solvent exchange and light irradiation cycles.

The oxidation of 1-phenylpyrrolidine (**1**) by the ground state of the **PD2-CDs** is feasible based on the predicted electron injection mechanism established from the calculated position of the HOMO level for the **PD2-CDs** (Step 1, Figure 2.5) and the oxidation potential of the **1**

(Figure A7). From our data, we estimate that SET from 1-phenylpyrrolidine (**1**) to the HOMO of the **PD2-CD** (Step 1, Figure 2.5) is energetically feasible ($\Delta G° = -0.14$ kcal mol^{-1}, Eq. A1.1). Such an electron transfer would create a radical centered on the nitrogen of the tertiary amine while replenishing the ground state of the **PD2-CD** that can be leveraged as an oxidant ($E_{ox} = +1.1$ V).

Considering that the energetics of the photoelectrode are well understood, we proceeded to evaluate the photocatalytic behavior of **ZnO NW|PD2-CDs** towards the photooxidation of **1**. The photocurrent observed upon white light irradiation of the films increases after the addition of one drop of **1** into the electrolyte solution in comparison to the photocurrent observed without the amine in solution (Figure 2.4b). This rise in current can be explained by the single electron photooxidation of **1** by the oxidized **PD2-CDs** on the ZnO surface, (Step 1, Figure 2.5). We anticipate that the charge carrier density of the ZnO NWs would not only be increased by injection of electrons originating on the **PD2-CDs** themselves, but also from the subsequent replenishment of the **PD2-CD** ground state by **1**, thus producing an increase in current passing through the film. The need for an applied bias was evaluated via the photooxidative performance of the CDs upon the addition of **1** with respect to a linear sweep voltammetry (Figure 2.4c) experiment. For contrast, the **PD2-CDs** reported here were compared to two other types of visible-light absorbing CDs (**GCDs** and **RCDs**, Figs. A8, A9 and Table A3) to see which CD system would be competent to drive the photooxidation of **1**. **GCDs** were synthesized from glutathione and formamide, thus, functional groups including carboxylic acids, amines, amides, and thiols are expected to be found on the surface,[37] while the **RCDs** (previously unreported), were prepared by reacting citric acid and formamide to yield mainly carboxylic acid and amine groups on the carbon dot surface (Figure A9).

Therefore, these somewhat different surface environments are expected to create variations in the excited state redox potentials of the CDs, along with imparting them with different optical properties. Surprisingly, the **PD2-CDs** significantly outperformed the other two types of CDs, despite the other CDs having clear absorption maxima in the visible region (Figure A8), allowing them to harvest more visible light, while the **PD2-CDs** only have a shoulder that extends into the visible region. There was no photooxidation observed for the **RCDs** even at high potentials and we observed minimal photooxidation by the **GCDs** starting at a potential of +0.35 V. Conversely, the **PD2-CDs** used in our device showed significant photooxidation of **1** at virtually no applied bias. Therefore, an organic transformation using the oxidized form of **1** should be plausible by employing this film as a heterogeneous photocatalyst. From our analysis, all the CDs reported here are capable of oxidizing **1** from their respective excited states, somewhat at odds with what we observed in the LSV (Figure 2.4c). One possible explanation for the increased catalytic performance of the PD2-CDs is related to matching the emission of the LEDs used in our photocatalytic experiments and the absorbance maxima of the different CDs (Figure A10). We note that the blue emission component of the LEDs aligns well with the absorption shoulder of the **PD2CDs**, increasing the number of available excited states to drive the formation of the radical of **1**. Somewhat significantly, this comparison demonstrates the flexibility and tunability of CDs for solar energy conversion purposes. By simply varying the starting materials of CD synthesis or by surface treatment one can achieve different optical and electronic properties that can be tailored to catalyze specific transformations.[109, 134]

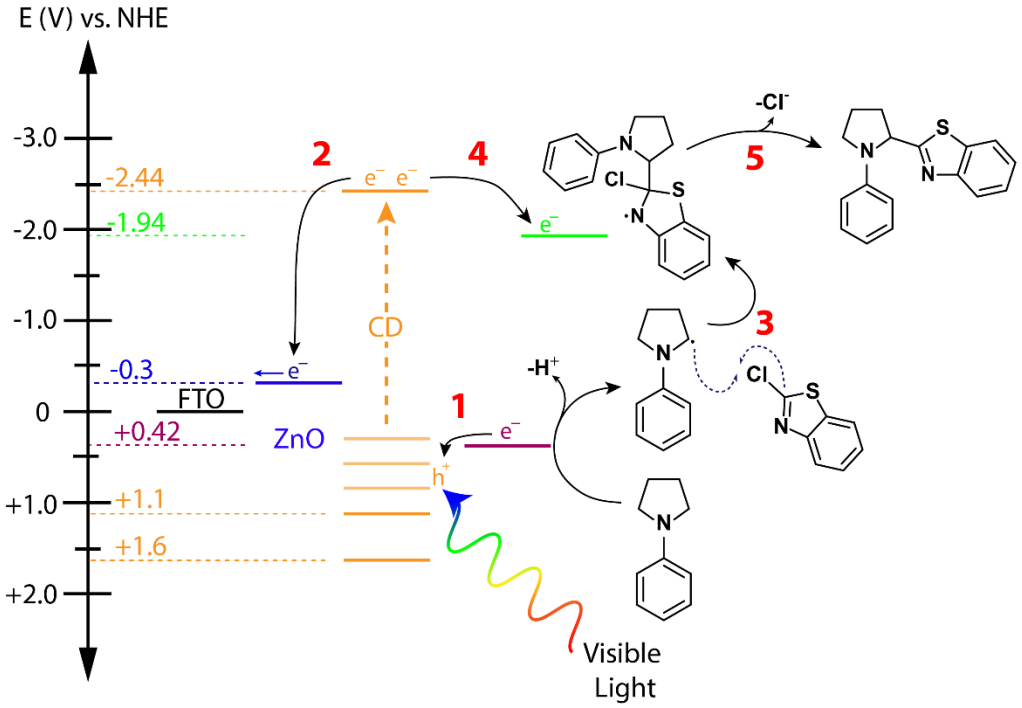

Figure 2.5 Proposed reaction scheme and suggested mechanism for the photocatalytically driven reaction of 1-phenylpyrrolidine (1) and 2-chlorobenzothiazole (2) with the respective redox potentials for the active species.

Coupling heteroaromatic molecules to the α-carbon position of tertiary amines is an interesting catalytic conversion due to the generation of high value-added products, particularly in the pharmaceutical industry.[135-137] Considering the importance of these transformations in the production of relevant medicinal drugs,[138-140] they have been rather underexplored. With this in mind, we decided to catalyze a direct α-heteroarylation of **1** and **2** using the **ZnO NW|PD2-CD** photoelectrodes. To our knowledge, this photocatalytic transformation has only been reported twice by the same group employing a molecular iridium photocatalyst and obtaining yields of 75-87% depending on the reaction conditions.[141-142] Prier and MacMillan performed the direct α-heteroarylation of different amines using $[Ir(ppy)_2(dtbbpy)][PF_6]$ (ppy = 2-phenylpyridine), where they promoted a mechanism that avoids the use of cyanoarenes and the associated radical anion pathway. Our photocatalytic

system is expected to follow the same mechanistic steps while replacing the molecular catalysts with a heterogeneous photocatalyst created from Earth-abundant elements as the key components of the system. Since the reaction conditions have previously been optimized by Prier *et al.* we decided to employ the highest yield conditions and optimize them for our catalytic system.[141]

The reaction of **1** and **2** was performed in an inert atmosphere by mixing the starting materials with sodium acetate and water in dimethylacetamide (DMA) and exposing this solution to the film and white light irradiation at room temperature. As reported in Table 1 (Entry 5), the highest yield was obtained after 24 hrs (97% yield). However, film degradation was observed beginning at approximately 10 hrs into the reaction period, likely due to an increasing HCl concentration over the course of the reaction and/or photocorrosion of the ZnO NWs.[143] Therefore, 10 hrs was established as an optimal reaction time to yield significant product while preserving the integrity of the films (Table 1 Entry 2) as confirmed by DRIFTS and SEM of the films pre- and post-reaction (Figures A4 and A11). The recyclability of the films was evaluated by performing the reaction for 10 hrs, rinsing the used film thoroughly, and using it for another 10 hr reaction period. On the second reaction we observed a yield of 55%. As expected, our device does not provide satisfactory results for a reaction that produces higher concentrations of acid as a by-product, highlighting one key area for optimization in future devices. The reaction was monitored through a bulk electrolysis (BE) experiment with no applied bias and UV-Vis spectroscopy in order to monitor the kinetics of the transformation. The current versus time plot (Figure A12) shows that there is a notable increase in charge density over the course of the first 30 min of the reaction, followed by stabilization after 1 hr. We postulate that this rapid initial current increase is due to the efficient oxidation of **1** through

a SET process involving the **PD2-CDs** on the surface of the NWs (Step 1, Figure 2.5) and a subsequent buildup of the radical product. Analysis of the UV-Vis spectra (Figure A13) over the course of the reaction reveals that product **3** is generated at a steady rate following zero-order kinetics, which is expected for heterogeneous catalysts where the reactants saturate the active surface.[144] Additionally, the initial generation and successive buildup of the 1-phenylpyrrolidine radical was also investigated through UV-Vis (Figure A14). In this case, the reaction was conducted without the addition of **2** and showed a rapid decrease in the concentration of **1** in the first fifteen minutes of reaction followed by a slow and stable consumption that correlates with the current observed in the BE experiment. The oxidation of the amine is accompanied by the deprotonation of the α-C-H bond that shifts the radical to the α-C (Step 3, Figure 2.5). As previously reported, this neutral radical can react with highly electrophilic **2** through a homolytic aromatic substitution (Step 3, Figure 2.5).[141] Then, a second SET from the excited state of a proximal **PD2-CD** (−2.44 V) to the activated complex (Step 4, Figure 2.5) may reduce the resulting radical σ-complex by eliminating the chlorine (as Cl^-) and yielding the desired α-heteroarylation product (Step 5, Figure 2.5). Therefore, the only anticipated by-product of this reaction is HCl.

Table 1. Assessment of multiple α-heteroarylation conditions.

Entry	*Catalyst*	*NaOAc (equiv.)*	*Reaction time (hrs)*[a]	*Yield (%)*[b]
1	ZnO NW|PD2-CD	1.0	4	32
2	ZnO NW|PD2-CD	2.0	10	82
3	ZnO NW|PD2-CD	1.0	12	60
4	ZnO NW|PD2-CD	1.0	24	82
5	ZnO NW|PD2-CD	2.0	24	97
6	PD2-CD dispersion	1.0	4	8
7	PD2-CD dispersion	1.0	24	56
8	ZnO NWs	1.0	24	50
9	ZnO NW|PD2-CD[c]	1.0	24	0

[a] All reactions were performed with 10 equiv. of water in 0.25 M dimethylacetamide at room temperature under white light irradiation. [b] The yield was calculated from an average of three reactions with 1,3,5-trimethoxybenzene as an internal standard for ^{1}H NMR. [c] Reaction performed in the dark.

The crude product of the reaction was extracted with ethyl acetate, purified, and isolated for characterization by column chromatography following the procedures detailed in the Supplementary Information. The isolated product was characterized, and determined to be the desired 2-(1-phenylpyrrolidin-2-yl)benzo[d]thiazole (Figure 2.1; **3**), through ^{1}H NMR (Figure A15), ^{13}C NMR (Figure A16) and high-resolution mass spectrometry (HRMS, Figure A17). The crude reaction yield was calculated through ^{1}H NMR using 1,3,5-trimethoxybenzene as an internal standard. It is worth noting the yield of the control experiments where the **PD2-CD** dispersions are expected to generate the product owing to their excited state redox potentials which suffice to catalyze the reaction. When compared to the **ZnO NW|PD2-CD** films, we still observed a lower yield for the unsupported **PD2-CDs** (8% after 4 hrs) due to a lack of an electron sink and stabilizer. In contrast, the bare ZnO NWs somewhat unexpectedly produced

a yield of 50% (24 hrs) that may be attributed to formation of a radical ion pair via reductive quenching of the excited state of **2** by **1** (we note **2** absorbs light at the blue edge of the visible spectrum, λ_{ex} = 390–400 nm, Figure A18, enabling excitation by the white light LEDs). From our work, it is unclear whether electron injection into the ZnO NWs occurs from this radical pair or prior to its formation, however we anticipate that either process will enable entrance into the proposed catalytic cycle. Overall, our observed yields approach or surpass those previously reported for this transformation with the molecular photocatalyst $[Ir(ppy)_2(dtbbpy)][PF_6]$.[141]

2.3 Conclusion

We have successfully engineered a heterogeneous catalytic photoelectrode from Earth-abundant elements for the α-heteroarylation of 1-phenylpyrrolidine (**1**) with 2-chlorobenzothiazole (**2**) at room temperature to produce 2-(1-phenylpyrrolidin-2-yl)benzo[d]thiazole (**3**). The photoelectrode makes use of ZnO NWs grown on an FTO substrate as a support and electron sink and is further sensitized to visible light by the attachment of **PD2-CDs** onto the surface. The energetics of the system at the heterojunctions were investigated and compared, and it was determined that the energy levels were aligned in a way that maximizes the efficiency of photocatalysis by promoting forward electron transfer. From optical spectroscopy and electrochemistry investigations, the mechanism for the electron transfer at the ZnO/CD interface was also explored to get insight on the role of **PD2-CDs** in photocatalytic processes, a subject that is usually obviated in the field. It was concluded that these specific CDs participate in both the oxidation and reduction reactions and thus, are a crucial component of the photocatalysis. Also, the presence of the ZnO NWs was determined

to be necessary to promote the flow of electrons from and into the **PD2-CDs** and to achieve higher reaction yields.

The system described in this work can surpass the performance of precious metal-containing photocatalysts and is built from inexpensive elements having the characteristics of a heterogeneous photocatalyst. Therefore, it may render itself more practical and advantageous than classical molecular systems. This work establishes a proof-of-concept to elucidate the underlying charge transfer mechanisms on the interaction between CDs and SC nanostructures.

We foresee the engineering of similar CD-based photocatalysts to produce value-added chemicals through solar-to-chemical energy conversion based on the study of the energetics of the components coming together. In fact, preliminary data shows that this device could be a viable photocatalyst for water splitting purposes where we see evidence for the generation of O_2 at pH < 12 (Figure A22). In addition, we have tested the possibility for such a system to sensitize singlet oxygen for radical-driven catalysis upon white light illumination. The degradation of dihydronaphtalene (DHN) by CDs demonstrates the production of singlet oxygen in solution (Figure A23) expanding the applications of this heterogeneous system in the photocatalysis field. Work to optimize the photocatalyst described in this Chapter and the other two systems is underway.

Chapter 3 Investigation of Nucleation and Growth in the Formation Mechanism of Kesterite Nanocrystals

The development of semiconductor nanocrystals (NCs) for various applications has attracted significant attention due to their tunable optical and electronic properties.[145] Hence, different materials including $CuInSe_2$ and CdTe have been suggested for applications in photovoltaics and photocatalysis.[146-147] To be sustainable, however, future technologies should make use of Earth-abundant elements with low degrees of environmental toxicity.[148] In this regard, kesterite $Cu_2ZnSn(S,Se)_4$ (CZTS) has emerged as a promising p-type semiconductor to address these needs owing to its favourable optoelectronic properties. CZTS materials have a direct band gap energy of 1.0-1.5 eV with a high absorption coefficient (10^4 cm^{-1}, Figure 3.1b), that renders the material optimal for solar energy conversion.[149] For instance, the application of CZTS materials as thin films in photovoltaics has resulted in remarkable power conversion efficiencies of up to 11.0%.[150]

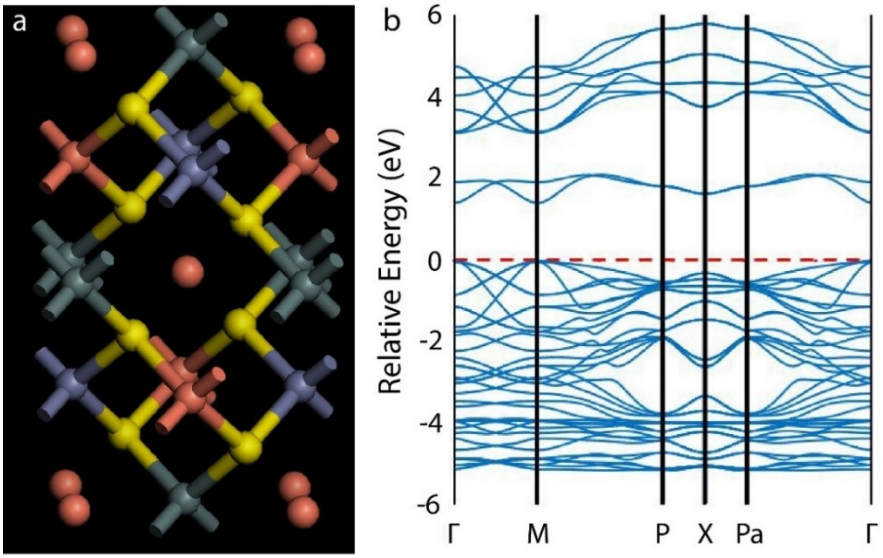

Figure 3.1 (a) Crystal lattice for two kesterite unit cells ($Cu_4Zn_2Sn_2S_8$), Cu: red, Zn: blue, Sn: grey, and S: yellow. (b) Density functional theory calculation of the density of states of kesterite. This plot shows a direct band gap with an energy of 1.42 eV.

The preparation of CZTS NCs has been explored through various synthetic methods including hot-injection,[151] microwave-assisted,[152] ball-milling,[153] and solvothermal reactions[154] with an emphasis on exploiting the quantum confinement effect to tailor the light absorption properties of the resulting material.[155] One major challenge that has emerged in the synthesis of these NCs is the formation of undesired binary (Cu_xS, SnS, and ZnS), ternary (Cu_2SnS_3), and wurtzite CZTS phases.[156-157] The formation of these phases ultimately affects the performance of the final material creating shorts in solar cells and defects that act as exciton recombination centers.[151, 158] Considering that the performance of the material is closely related to the structure and size of the NC, recent investigations have tried to unravel the formation mechanism of CZTS NCs through spectroscopic and computational methods to obtain a better understanding of their growth, phase evolution, and size distributions.[159-160] It is well known that increasing the temperature and the time of the reaction promotes the formation of larger NCs,[152, 161] therefore, mechanistic studies have focused on the effects of solvent, capping groups, sulfur sources, salt precursors, and the reaction stoichiometry on the formation pathway, phase purity, and size dispersity of kesterite CZTS NCs.

The roles of solvent and capping agents in the formation mechanism and morphology of CZTS NCs have previously been established by different groups.[162-164] However, it still requires a more profound understanding given that the solvent and other additives perform the crucial role of activation and stabilization of the metal precursors (often either an acid/base or redox process).[165-166] These processes are key to the formation of the desired kesterite phase as the metal ions have a specific stoichiometry in the final crystal according to their oxidation states and ionic radii.[167] As an example, Hou *et al.* demonstrated that oleylamine reduces Cu^{2+} ions and forms the corresponding imine at temperatures above 130 °C, rendering this “solvent”

vital for the creation of intermediates before CZTS nucleation in this particular reaction.[168] Other studies have shown the crucial effect of solvent pH in such transformations. Suryawanshi *et al.* observed the formation of mixed CZTS phase with Cu_2SnS_3 and copper sulfide crystals at low pH, phase pure CZTS NCs at neutral pH, and mixed CZTS phase with tin sulfide crystals at higher pHs.[154]

The identity of the sulfur source has likewise been shown to perturb the formation of pure kesterite to wurtzite phase in some cases. In fact, it is understood that the use of elemental sulfur in long hydrocarbon solvents favors the formation of kesterite,[162, 169] while the use of alkylthiols promotes the formation of wurtzite in CZTS NCs.[170-171] Zou *et al.* reported the phase-controlled synthesis of either kesterite or wurtzite by tuning the reactivity of the sulfur precursor towards the Zn^{2+} ions.[172] In this regard, Li *et al.* also tested sulfur reactivity towards the formation of specific CZTS crystalline phases and found that highly reactive sulfur compounds easily form H_2S that triggers the direct formation of the kesterite phase, while less reactive species would yield wurtzite through a copper sulfide intermediate, contrary to Zou *et al.*[173] In brief, the sulfur source of choice can strongly influence the outcome of the reaction by creating different metal-sulfur interactions and crystalline intermediates or by simply generating highly reactive H_2S. Taken together, this illustrates how challenging and non-trivial it is to direct the crystalline structure of a quaternary lattice.

While progress has been made in directing the formation of pure kesterite phases by varying the reaction parameters, there is still a knowledge gap regarding the formation mechanism of these NCs and how to control their final size. Work should focus on the metal-sulfur activation steps, the nucleation of binary and ternary structures to control the size dispersity, and the stability of the kesterite structure considering that Cu^+ and Zn^{2+} have a

similar ionic radius and can interchange positions in the lattice. Some groups have observed the immediate precipitation of kesterite CZTS NCs using elemental S activated by oleylamine, and the formation of Cu sulfide binary structures with alkylthiols.[173-174] However, most mechanistic studies report a multistep reaction going from Cu sulfide crystals to Cu_2SnS_3 and finally forming CZTS NCs after the incorporation of Zn^{2+} through cation exchange.[151, 156, 161, 169, 172, 175] The generation of these intermediate crystals is governed by thermodynamic and reactivity factors. For instance, the formation of SnS is disfavored due to its borderline hard Lewis acid nature compared to its copper counterpart, while the formation of CuS takes place over ZnS since it is more thermodynamically stable and prone to react with S^{2-} through a soft Lewis acid/base reaction.[160, 176] Wang *et al.* performed *in-situ* Raman spectroscopy on aliquots taken throughout the course of the formation of the NCs.[177] They showed that the nucleation of Cu_xS starts at room temperature until 170 °C when the kesterite phase starts forming. A three-step mechanism was suggested by Tan *et al*. where the generation of Cu sulfide species early in the reaction was observed, followed by the diffusion of Sn^{4+} into the crystals to form Cu_2SnS_3 as high temperatures make Cu atoms highly mobile, facilitating a cation exchange.[151] In the last step, Zn^{2+} diffuses into the ternary crystal to form CZTS. In other procedures, wurtzite CZTS NCs have been annealed in a post-reaction treatment to induce the phase transformation to the more thermodynamically stable kesterite structure giving insights about the stability between quaternary phases and the effects of surface ligands on phase transformations.[178] Furthermore, computational studies have been conducted to get information about the thermodynamic stability of the possible binary, ternary, and quaternary (wurtzite and stannite) phases that could occur towards the formation of kesterite CZTS

NCs.[160] It was shown that all three phases have comparable enthalpies of formation with the kesterite phase being the lowest in energy and most thermodynamically stable.

Much of what has been learned from these systems can be employed towards the understanding of a nucleation and growth mechanism.[159, 176] Although there are currently no growth models for quaternary NCs, some approximations can be made from LaMer theory for the formation of monodispersed colloids.[54] The generation of a homogeneous nucleation can be understood in terms of the energetic instability of a supersaturated solution that draws the nucleation towards a thermodynamic minimum.[179] This theory follows three steps. As a first step, there is an increase in the ion concentration due to the precursor decomposition (usually reduction) and free atom supersaturation. This increase in concentration triggers a fast self-nucleating process where the solute building blocks create nuclei from which the final NCs will grow. In the second step, there is equilibration between the formation of new nuclei and the decrease in the solute concentration. Lastly, the NC seeds growth becomes diffusion-controlled and happens at the expense of the remaining solute building blocks or from smaller nuclei (Ostwald ripening) until the surface energy is minimized. Therefore, to obtain a narrow NC size distribution, the first nucleation must be considerably fast. If the CZTS NC formation happens after the diffusion of Zn^{2+} into Cu_2SnS_3 NCs or the diffusion of both Zn^{2+} and Sn^{4+} into Cu_xS NCs,[180] then, the final concentration and dispersity should follow the classical interpretation of nucleation and growth. Thus, understanding the formation of either Cu_xS Cu_2SnS_3 towards the generation of kesterite CZTS NCs can provide better tools to control their synthesis.

Hot-injection-type (HI) reactions are an optimal method to study nucleation and growth mechanisms as the solution can be sampled *in-situ* and the promotion of a stepwise NC

formation mechanism can be controlled manually. In this chapter hot-injection synthesis is employed to demonstrate the stepwise nucleation and growth mechanism of kesterite CZTS NCs. Furthermore, considering that this synthetic method becomes impractical for mass scale production, a simple microwave-assisted reaction is provided for the high-throughput synthesis of kesterite CZTS NCs.

3.1 Experimental

3.1.1 Materials

Copper (II) acetylacetonate [$Cu(acac)_2$], oleylamine (OA 50%), and 1-dodecanethiol (DDT) were purchased from TCI. Zinc acetate dihydrate [$Zn(OAc)_2 \cdot H_2O$], tin chloride ($SnCl_2$), elemental sulfur (purum ≥ 99%), hexane (≥ 99%), ethanol (99%) were purchased from Sigma Aldrich. All chemicals were used as received without further purification.

3.1.2 General Procedures

TEM images were collected using a benchtop LVEM5 microscope from Delong Instruments (Brno, Czech Republic) operating at 5 kV and a JEM-2100F (Jeol Ltd) analytical electron microscope operating under 200 kV. The Cu-300HD grids (Pacific Grid-Tech) were cast by immersing them in a 1 mg mL^{-1} dispersion of CZTS NCs in hexanes and dried under air. The NC size distribution was determined over an average of 200 particles using a Fiji imaging software to process the images.

Powder X-ray diffraction data was collected using a 2nd Gen D2 Phaser X-ray diffractometer with monochromatized Cu Kα radiation with a nickel filter (Bruker AXS). The power of the X-ray source was set to 30 kV and 10 mA in a continuous PSD fast scan mode. The spectra

were collected in 2θ ranging from 20 to 70° with a step increment of 0.05° and scan speed of 1 s $step^{-1}$ with a PSD opening of 4.7970°. The data analysis was performed with XPert Highscore software.

Raman Spectroscopy measurements were performed using a Renishaw Invia spectrometer. A 514 nm diode laser with ~5 mW power was utilized. A software algorithm was used to remove cosmic ray interference. The spectra were collected over a period of 1-2 minutes.

3.1.3 General CZTS Synthesis (HI)

CZTS NCs were synthesized from salts of copper, zinc, and tin using elemental sulfur as a sulfur source. Briefly, $Cu(acac)_2$ (1 mmol), $Zn(OAc)_2 \cdot 2H_2O$ (0.5 mmol), $SnCl_2$ (0.5 mmol), and 5 mL of OA were placed in a three-neck round bottom flask. The flask was connected to a Schlenk line where the reaction was degassed three times at room temperature and left under N_2 atmosphere. The sulfur source was prepared from elemental sulfur (4 mmol) in OA (2 mL) by sonicating the solution for 25 minutes. Then, the flask was heated to 240 °C in a sand bath where the sulfur solution was injected, the solution is left to react for 10 minutes and then it is rapidly quenched and cooled using an ice bath. The solution is then transferred to a 50 mL centrifuge tube and washed three times using 5 mL of hexanes and 35 mL of ethanol (99%) while centrifuging and discarding the supernatant between washes. The product is left to air dry under air overnight for further experiments.

3.1.4 General CZTS Synthesis (Microwave-Assisted)

CZTS NCs were synthesized from the same precursors used in for hot-injection method. The elemental sulfur (4 mmol) was placed in a 10 mL microwave reaction vessel along with OA (4 mL) and the solution was sonicated for 20 min to dissolve the sulfur. Subsequently, the

$Cu(acac)_2$ (1 mmol), $Zn(OAc)_2 \cdot 2H_2O$ (0.5 mmol), and $SnCl_2$ (0.5 mmol) were added into the vessel containing the sulfur precursor. This solution was sonicated while shaking for 5 minutes to disperse the salts evenly throughout the solution. The mixture was pre-stirred for 5 more minutes before placing it in the microwave reactor (Discover SP microwave from CEM Corporation) to avoid the formation of clumps. Once in the reactor, the solution was rapidly heated to 240 °C and held at that temperature for 10 minutes. The product was washed using hexanes and ethanol following the HI purification procedure and dried overnight for further testing.

3.2 Results and Discussion

Kesterite CZTS NCs were synthesized *via* HI and microwave reactions in a 160–260 °C temperature range for 1–40 minutes. The solvent of choice for the reactions was OA because it is not only a high boiling point hydrocarbon, but it also stabilizes the metal salt precursors and prevents them from decomposing at lower temperatures, a detrimental process that would generate undesired phases.[181]

It is anticipated that the size evolution as a function of time of the synthesis of Cu_xS NCs could provide evidence for the proposed mechanism. If the size evolution function follows the same growth rate as the one observed in the growth of kesterite CZTS NCs, then this would suggest that the final size dispersity of NCs will be governed by the nucleation and growth of the intermediate species (Cu_xS) before the incorporation of the other two cations into the lattice. Furthermore, the formation of kesterite CZTS NCs reveals a color change from a pale-yellow to brownish after the injection of the sulfur (Figure 3.2), that provides qualitative evidence for the formation of Cu_xS NCs as reported previously.[159] This pale-brown color rapidly changes to dark-brown denoting the formation of kesterite CZTS NCs.

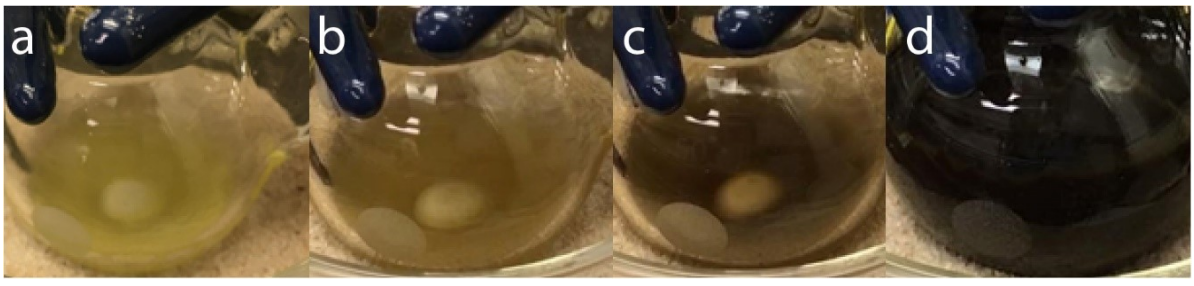

Figure 3.2 Photographs illustrating the color change of the reaction solution from the moment the sulfur precursor is injected (a) until the end of the reaction at 10 min (d). The pale-yellow and brownish colors seen in (b) and (c) hint the formation of a Cu_xS intermediate.

The critical radius for the nucleation onset of this intermediate and the duration of this phase will vary according to thermodynamic and kinetic parameters that will ultimately regulate the size dispersity of the NCs. These factors can be controlled by choosing the right reaction conditions including solvent, capping agents, and saturation. The faster the nucleation burst, the narrower the final size dispersity will be because this will avoid the nucleation of early and late comer nuclei. Increasing the saturation of solute will allow it to start nucleating once it reaches a smaller critical radius. Likewise, changing the solvent will modify the dielectric constant of the environment and will produce a direct effect on the surface energy on the nuclei. Hence, these synthetic handles could help tailor the size distribution of the Cu_xS intermediate and thus, the final kesterite CZTS NC size distribution as well.

To gain information about the morphology and size evolution, aliquots should be taken at different times (5 s, 30 s, 1 min, 2 min, 5 min, 10 min) after the injection of the sulfur precursor. Based on the expected growth mechanisms, the size distribution of the NCs should show small nuclei at short reaction times (5-30 s) followed by an increase in size as these nuclei grow. There may exist a plateau in the size as the solute is consumed by the formation of NCs above the critical radius for nucleation. If the size dispersity shows a unimodal size distribution, then growth through OR may be occurring. However, growth by OR requires nuclei to dissolve, followed by the precipitation of the dissolved material onto larger crystals. This behavior does not agree with the expected mechanism for CZTS NC formation that is speculated to happen through the generation of a Cu_xS intermediate followed by the diffusion of Sn^{4+} and Zn^{2+} into the lattice. In the proposed mechanism, the formation of the intermediate will dictate the final size of the NCs where further growth if any, will be governed by aggregative mechanisms. Nonetheless, OR could be at play in the formation of the Cu_xS

intermediate if this process is slow enough. Conversely, if a multimodal size distribution is observed, it may be due to the formation of undesired binary and ternary phases as well as an irregular aggregative growth. The preliminary TEM images show a spherical morphology and an increase in the size when comparing NCs synthesized at 180 and 260 °C (Figure 3.3).

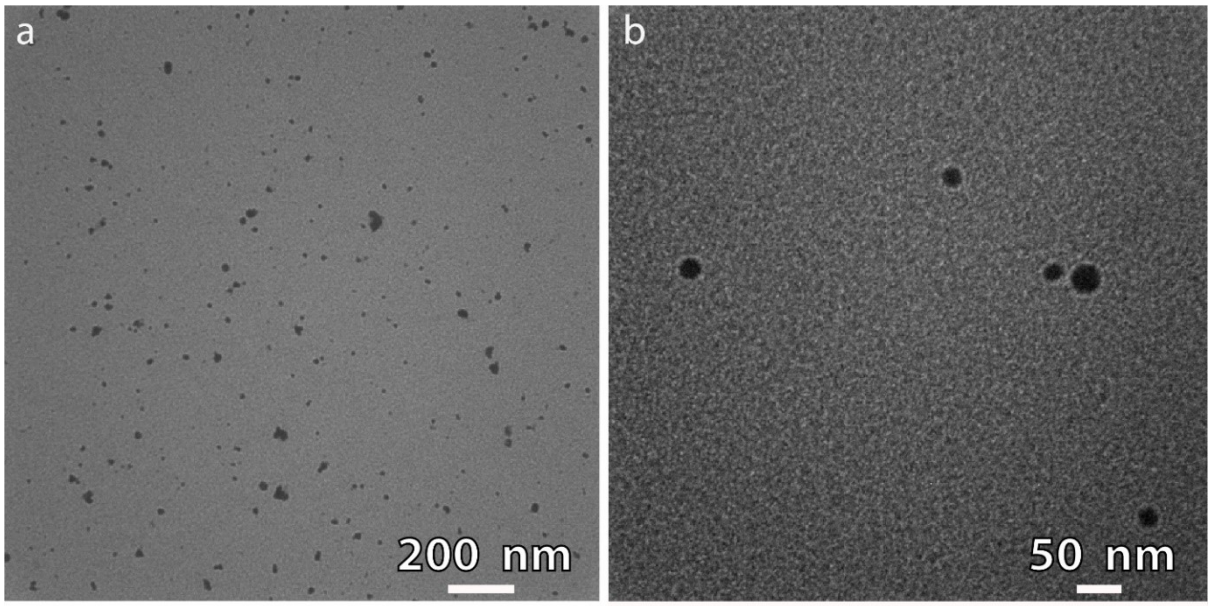

Figure 3.3 TEM images for kesterite NCs synthesized through a microwave-assisted reaction at 180 (a) and 260 °C (b). The NCs appear to have a spherical morphology with average sizes of 8.5 ± 2.8 and 22.7 ± 8.1 nm, respectively.

The PXRD diffractogram for the final NCs synthesized at 240 °C is displayed in Figure 3.4a. This pattern shows three main reflections at 2Θ = 28.8°, 47.6°, and 56.4° corresponding to the (112), (220), and (312) planes respectively. Other reflections can be observed at 2Θ = 33.3° (200), 69.5° (008), and 76.6° (332) correlating to literature values.[178] The size of the crystals in the powder are related to the full width at half maximum (FWHM) from the diffraction peaks through the Scherrer equation[176]:

$$\tau = \frac{k\lambda}{\beta \cos(\theta)} \qquad \textbf{Eq. 3.1}$$

This equation allows the estimation of the size of the NCs from the PXRD patterns. The calculated sizes for the NCs synthesized at different temperatures are shown on Figure 3.4b and range from 2.5–23 nm based on the first major peak at 28.8°. There is a significant increase in the size of the NCs as the synthesis temperature goes from 180 to 260 °C due to the increment in the reaction rate and collisions between NCs. Additionally, the PXRD spectra for the aliquots taken at 5 and 30s should show a pattern corresponding to a Cu_xS structure. The spectra for the subsequent aliquots might exhibit patterns for some sort of ternary structure (*i.e.* Cu_2SnS_3) depending on the rate of the cation exchange reaction.

In the absence of corroborating data, much of the following represents a presumptive discussion regarding the mechanism of NC formation. The NC size estimates for this reaction should show a rapid increase in the size for the speculative formation of Cu_xS intermediate at early reaction times. Then, the growth rate should decrease due to the consumption of available solute. Thus, there should be no significant NC growth at that point. This trend should also be noticeable when the salt precursors are injected in a stepwise fashion assuming that the formation of the intermediate and the cation exchange reactions are separated in time. Furthermore, the Cu_2S and Cu_2SnS_3 NCs synthesized under the same conditions should follow a similar growth trend and final size upon the completion of the reaction. This could also suggest that the nucleation and growth of the kesterite CZTS NCs is governed solely by the former generation of either Cu_2S or Cu_2SnS_3 with the Sn^{4+} and/or Zn^{2+} ions only diffusing into the crystal without affecting the size.

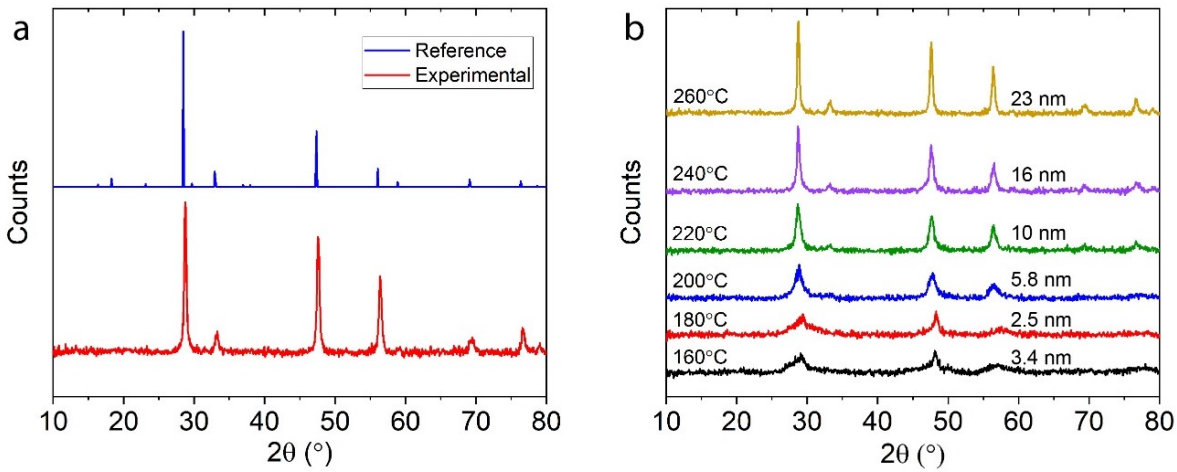

Figure 3.4 (a) PXRD spectra for the synthesis of kesterite CZTS NCs through a microwave-assisted reaction at 240 °C for 10 min. The experimental pattern matches the reference spectrum for the kesterite crystalline structure. (b) PXRD spectra showing the narrowing and increase in peak intensity for the kesterite CZTS NCs synthesized through a microwave-assisted reaction at different temperatures.

Energy-dispersive X-ray spectroscopy (EDS) can be conducted on the CZTS aliquots taken at different reaction intervals to demonstrate that the NCs are mainly composed of Cu and S at the beginning of the reaction (5 s and 30 s). The ratio of the Cu to S would give insight about the nature of the intermediate species. For instance, intermediates including CuS, Cu_2S, Cu_7S_4 have been observed in the literature.[156, 182-183] These species vary in chemical composition and reactivity towards a cation exchange mechanism for the formation of CZTS NCs. It has been reported that a cation exchange is favorable in Cu_2S crystals since the S-S bonds in the anionic network would remain intact.[169] As the reaction proceeds, signals for the Sn^{4+} and Zn^{2+} cations should be seen as they get incorporated into the lattice (1–2 min) to form the kesterite CZTS NCs. These results could hint at an onset for the incorporation of the two cations into the Cu_xS lattice, which could be correlated to the copper precursor concentration or the stoichiometry of the intermediate species. In addition, the diffusion mechanism could be investigated by EDS to see if there are any preferred phases for the cation exchange as it has

been done before for copper sulfide-based nanostructures.[184] The formation of other transient intermediate species (*i.e.* SnS and ZnS) could be evaluated upon cation exchange as well. Therefore, elemental ratios of the aliquots could not only offer further evidence for the two-step formation mechanism proposed in this work, but it could also help unravel the diffusion mechanism of the cations during the exchange.

Raman spectroscopy was performed (λ_{ex} = 514 nm) on the samples synthesized *via* the microwave method to gain an understanding of the compositions present. The most typical Raman active mode observed for kesterite CZTS is the A mode at 338 cm^{-1} due to the symmetric vibrations of the S atoms in the crystal.[185] Peaks are also expected at 258, 288, and 358 cm^{-1}.[186] The Raman peaks for possible contaminating binary phases can be found at 472 (Cu_2S), 314 (SnS_x), and 351 cm^{-1} (ZnS), while ternary phase modes may appear at 303, 318, and 355 cm^{-1} (Cu_2SnS_3) for tetragonal, orthorhombic, and cubic phases respectively.[186-187] The Raman spectra for the time-interval aliquots should show a peak at 472 cm^{-1} for short reaction times (5 and 30s) that corresponds to Cu_2S NCs. It is speculated that the peak at 472 cm^{-1} will be observed for short reaction times at low temperatures (180 °C) but not at temperatures above 200 °C. This hypothesis comes from temperature-dependent Raman experiments where these results show a peak at 472 cm^{-1} assigned to the Cu_2S nuclei when the reaction temperature is kept below 200 °C (Figure 3.5a). However, this peak is no longer observed once the temperature rises above 200 °C. This observation corroborates the experiments performed by Wang *et al.* where they also observe the disappearance of the 472 cm^{-1} peak above 200 °C.[177] The peak for these nuclei completely disappears once the reaction is performed at 200 °C which was regarded as the onset for "direct" CZTS formation through a microwave reaction. Other peaks arise at 289 (Cu_2SnS_3), 330 (wurtzite CZTS), and 338 and 361 cm^{-1} (kesterite CZTS) at

160 °C and start to decrease as the temperature rises suggesting the formation of multiple phases at temperatures below 200 °C. When the reaction is performed at temperatures between 200–220 °C, the most prominent mode observed is centered at 338 cm^{-1} with a small shoulder at 328 cm^{-1}. The peaks that correspond to ternary and wurtzite phases are almost completely absent at 240 °C and disappear entirely at 260 °C, leaving the 338 cm^{-1} peak corresponding to the predominant phase in the material.

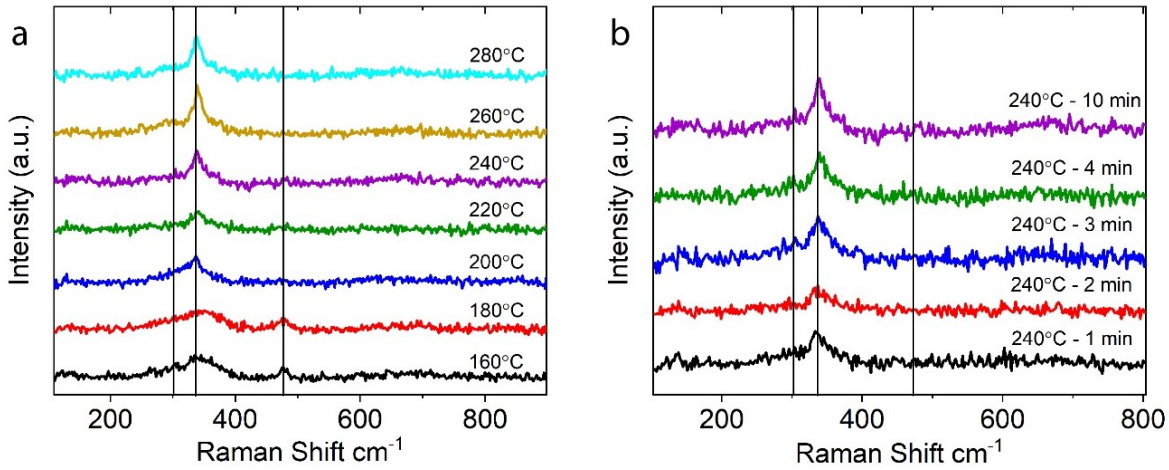

Figure 3.5 (a) Raman spectra for the microwave-synthesized kesterite CZTS NCs at different temperatures. The signal for the Cu_2S NC intermediates is observed at 474 cm^{-1} at temperatures below 200 °C. This peak disappears as the temperature increases above 200 °C. (b) Raman spectra for the time-evolution experiment at 240 °C. The signal for the Cu_2S intermediate is not observed even at short reaction times (1 min). These results suggest that the formation of intermediate species could be temperature dependent and might be bypassed at higher temperatures (>200 °C).

The A mode can be clearly distinguished in the time-dependent Raman measurements at longer reaction times through peaks at 338 cm^{-1} with a shoulder at 358 cm^{-1} as well as at 288 cm^{-1}, coinciding with literature values for CZTS. These signals appear broader for smaller NCs due to phonon confinement.[186] There are no distinguishable signals for binary and ternary phases at this point (10 min). While the absence of these signals suggests a high degree of purity in the material, this does not confirm the formation of pure kesterite CZTS NCs since

the broad Raman peaks for this structure could be overlapping with those of binary and ternary phases.

The formation of Cu_xS nuclei is strongly dictated by the temperature of the reaction given that the formation rate (j_n) is related to the monomer diffusion constant (D) and molecular volume (v_0) of the NCs through Eq. 3.2.[64, 188] The other variables include the temperature (T), the gas constant (R), the molar (V_M) volume of the NC, and the surface tension (γ).

$$j_n = \frac{2D}{v_0^{\frac{5}{3}}} \exp\left(-\frac{16\pi\gamma^3 V_m^2}{3(RT)^3(lnS)^2}\right) \qquad \textbf{Eq. 3.2}$$

Thus, higher temperatures will increase the diffusion rate of the monomers and will result in faster nucleation and growth kinetics. It is important to note that the temperature-dependent measurements show the data for the final products at each of the featured temperatures. In this regard, the only experiment that allow us to partly confirm this hypothesis is time-dependent Raman spectra collected at 240 °C (Figure 3.5b). Conversely, if we are still able to observe a Cu_xS signal at short reaction times and high temperatures, a kesterite peak at 338 cm^{-1} could be simultaneously observed as the final CZTS NC formation by cation exchange is accelerated by the increase in temperature. Of value would be to investigate if the formation of the Cu_xS intermediate could be bypassed by increasing the temperature further. Temperatures of 280 °C and above could destabilize the formation of binary metal chalcogenide intermediates and kesterite CZTS NCs could be directly precipitated as previously shown in the literature.[173-174] Another alternative would be to couple a microwave reactor or HI reaction setup with a Raman microscope to do *in-situ* measurements and resolve the formation of binary structures in time.

Surprisingly, time variation experiments at 240 °C showed similar results between experiments with no substantial changes in the Raman spectra (Figure 3.5b). The peaks for Cu_2SnS_3 and wurtzite-CZTS at 302 and 328 cm^{-1}, respectively, are noticeable throughout the entire time range (1–10 min) though they decrease in intensity. Furthermore, there was no detectable peak at 474 cm^{-1} to confirm the formation of Cu_xS possibly suggesting that either the nucleation of this binary phase is too fast to be resolved or the formation mechanism of kesterite CZTS proceeds through the direct nucleation of Cu_2SnS_3 bypassing the generation of Cu_xS at 240 °C. On the other hand, when the same reaction was performed at 180 °C, the phase transformation could be tracked in time (Figure 3.6). The formation of Cu_xS and Cu_2SnS_3 is observed at the beginning of the reaction (5 min) with identifiable peaks at 278, 328, and 477 cm^{-1} as well as the formation of wurtzite CZTS with a major peak at 328 cm^{-1}. The shoulder at 338 cm^{-1} is assigned to the pre-formation of the kesterite phase. As the reaction progresses, the peaks for the binary and ternary phases decrease as the signal for the kesterite CZTS mode A rises. However, after 40 minutes, the peaks for the binary and ternary structures can still be seen illustrating that temperatures below 200 °C are inadequate for the full conversion of precursors into kesterite CZTS NCs.

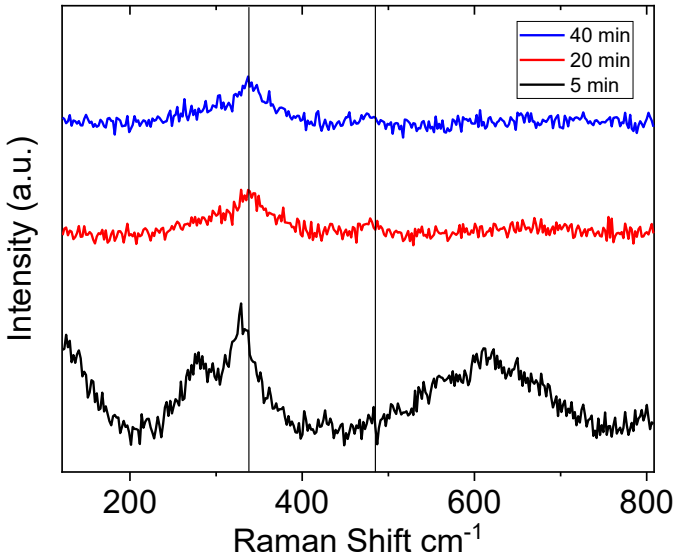

Figure 3.6 Raman spectra for the time evolution experiments at 180°C in a microwave-assisted reaction. There are binary, ternary and wurtzite phases that can be distinguished at short reaction times (5 min). Some of these phases decrease in intensity, while others vanish as the reaction proceeds for longer times. However, the Cu_2S signal at 472 cm^{-1} can still be seen even after 40 min of reaction. This data suggests that 180°C is an inappropriate temperature for the synthesis of pure kesterite phase.

During hot injection synthesis, varying the sequence of precursor injection into the reaction vessel can give more insight into the formation of binary and ternary phases. It is possible that modes for the formation of Cu_xS and Cu_2SnS_3 (472 and 355 cm^{-1}, respectively) will be seen in the reaction where the Zn precursor is injected after the sulfur injection. These modes will most likely decrease slowly in intensity following the Zn injection, while the kesterite CZTS mode at 338 cm^{-1} will rise due to the incorporation of Zn^{2+} into the ternary structure. The three-step reaction going from all phases towards the formation of kesterite CZTS NCs can be evaluated when the Sn and Zn are injected in a stepwise fashion after the addition of the sulfur precursor. The mode for Cu_2S at 472 cm^{-1} should be identified when the other metal ions are not present. Upon the addition of Sn, the modes at 318 and 355 cm^{-1} would

start to rise suggesting the formation of Cu_2SnS_3. Lastly, the injection of Zn into the solution would yield the desired kesterite CZTS phase showing the expected peak at 338 cm^{-1}.

The effects of temperature and time on the size of the NCs was evaluated in the microwave-assisted reactions. An increase in temperature from 200 to 240 °C provoked a significant increase in the NC size from 5 to 20 nm, respectively (Figure 3.4b). There should be less of a temperature influence in the size of the NCs at more dilute concentrations since there will be a lower concentration of NCs and thus, less collisions to promote growth. It is expected that two-fold dilution experiments will show that there is a slower increase in the size as well as a narrower size distribution when the temperature of the reaction is increased. Though, the increment in size should not be as prominent when the time of the reaction is varied as it is observed in the reactions performed at 180 °C (Figure 3.7a). This behavior should correlate with what is expected from CNT where the reaction and diffusion-controlled mechanisms can be separated in time at dilute concentrations.[188] In a concentrated regime, there is no way of separating these processes in time as the amount of collisions are increased, leading to a broader size distribution due to a stronger temperature dependence.

Experiments using DDT and thiourea as sulfur sources can be conducted to confirm the effect of the reactivity of the sulfur source in the final phase of the CZTS NCs.[165] Reactions employing alkylthiols as sulfur sources should yield wurtzite CZTS NCs as reported by several groups before.[151, 165, 178] In fact, the use of DDT always yields wurtzite in both HI and microwave-assisted reactions showing a sharp peak at 328 cm^{-1} corresponding to the wurtzite CZTS phase (Figure 3.7b). This is explained by the slower release of sulfur in alkylthiols compared to the use of elemental sulfur in OA. In alkylthiols S is covalently bonded to a C and an H atom, making it more stable in comparison to H_2S. Also, alkylthiols can disrupt the

interaction and reactivity between Cu^{+} and S, creating Zn rich monomers that favor the formation of wurtzite.[165, 172] In terms of reactivity, the affinity strength of the anion ligand for the cation in the salt precursors has been demonstrated to play a non-negligible effect in regulating the kinetics of wurtzite CZTS NC formation.[151] While this reactivity consideration could be playing a role in the formation of metal chalcogenide NCs, it is believed that it will have a minimal effect on the kinetics of the reaction when compared to concentration, temperature, and additive effects.

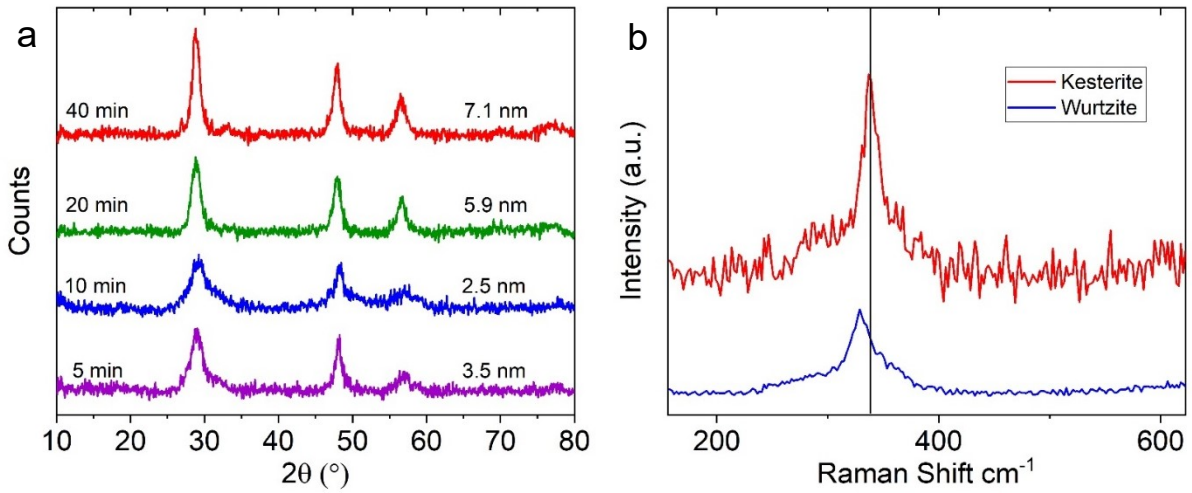

Figure 3.7 (a) Time-dependent PXRD spectra for the kesterite NCs synthesized at 180C through a microwave-assisted reaction. The increment in the NC size is slow when the reaction time is increased from 5 to 40 min. (b) Raman spectrum for the HI synthesis of CZTS NCs using elemental sulfur (red trace) and DDT (blue trace) as sulfur sources. The use of alkylthiols yields wurtzite CZTS NCs with a predominant peak at 328 cm^{-1} instead of the kesterite phase (338 cm^{-1}).

3.2.1 Formation mechanism

The preferential formation of Cu_xS nuclei over SnS and ZnS species can be partially explained by the principles of hard and soft Lewis acids and bases.[189] Lewis acids will be electron pair acceptors while bases will behave as electron pair donors. The hard or soft character will be defined from their donating or accepting strength that is strictly related to the

charge density of the ion and electronic polarizability. At the beginning of the reaction and prior to the sulfur injection, Cu^{+}, Sn^{4+}, and Zn^{2+} cations will be present in solution forming complexes with OA. This coordinating solvent being a hard base will form a chemically stable and less reactive complex with Sn^{4+}, which is a hard acid. The other two cations will form more labile complexes with OA with the Cu-OA complex being more reactive than the Zn-OA. In this regard, the Cu-OA complex would be the first one to decompose and react at high temperature. Likewise, upon the decomposition of the cation-OA complexes and injection of the sulfur precursor, the Cu^{+} ions will be the first ones to react with the S^{2-} through a soft acid-soft base interaction, respectively.

The formation of the Cu_xS nuclei appears to act as a template that dictates the number and size dispersity of the final kesterite CZTS NCs. However, the nature of these nuclei (*i.e.* CuS vs. Cu_2S or Cu_4S_7) should be considered when proposing a viable cation exchange mechanism. For instance, it is known that Cu^{+} has a higher lattice mobility in Cu_2S through the anionic framework provided by S^{2-}.[169] Thus, a cation exchange mechanism is more likely in Cu_2S than in CuS since the crystal of the latter contains S-S bonds in its framework. This bond is of substantial strength (430 kJ/mol)[190] and its cleavage would provoke a significant re-arrangement of the anionic structure. It is unknown if the ternary phase Cu_2SnS_3 forms in parallel with the Cu_xS nuclei, after their generation as a second metastable intermediate, or if it forms at all at higher temperatures. In any case, it seems unlikely that such a ternary phase is playing a crucial role in the formation mechanism for kesterite NCs other than indicating the cation exchange event.

3.3 Conclusion

The mechanism of nucleation and growth for the formation of kesterite CZTS NCs was investigated from experimental results and literature information. This reaction is speculated to happened through the formation of a copper sulfide-based metastable intermediate that provides a local minimum in the growth-dependent free energy landscape. This intermediate is hypothesized to act as a template for the incorporation of Sn^{4+} and Zn^{2+} by cation exchange to generate the quaternary kesterite structure. Furthermore, the nucleation step of the intermediate could govern the quantity and final size dispersity of the CZTS NCs. Therefore, the size distribution could be narrowed by accessing and controlling the formation of these structures through variations in the temperature, additives, and concentration. Time-dependent studies on the size of the intermediate species will help uncover if their formation follows a classical picture or not. These results highlight the complexity in the formation of phase pure quaternary NCs with narrow size distributions and give insight into possible ways of achieving better synthetic control in such processes.

The incorporation of additives (*i.e.* amines) into the reaction mixture can disrupt the formation of intermediate species promoting the direct formation of the quaternary structure. These studies will allow the comparison of two formation pathways (two-step through intermediate generation vs. direct precipitation) in order to optimize the synthesis of quaternary NCs, favoring phase purity to decrease exciton recombination. The optimization and control of such syntheses will enhance the performance of these materials in photocatalytic applications and other optoelectronic devices.

Chapter 4 Conclusion and Future Directions

Solar-to-chemical energy conversion is a viable option in conjunction with the field of photovoltaics towards meeting the increasing human needs for clean and renewable energy. In this regard, the area of photocatalysis using devices engineered from Earth-abundant materials has made great progress in the last two decades optimizing the production of so-called solar fuels including H_2 from water splitting, short hydrocarbons from the reduction of CO_2, and valuable pharmacophores through the catalysis of organic reactions. The nanostructuring of their constituent materials has been proven as an effective strategy to increase the performance and efficiency of such devices, in particular MOx SCs and inorganic NCs. This scaling regime grants materials high surface areas and short carrier collection pathways to maximize the catalytic activity and reduce exciton recombination. Additionally, quantum confinement can be exploited in metal chalcogenide NCs and other nanoscale systems to tailor the redox potential to the desired chemical transformation, highlighting the superior photocatalytic performance of NMs in comparison to their bulk counterparts.

Although being suitable platforms for photocatalysis, some SCs still suffer shortcomings that stem from their intrinsic properties. Their composition makes them prone to undesired decomposition pathways and their limited light absorption in the visible part of the solar spectrum is impractical for the generation of solar fuels. These drawbacks cannot be resolved through nanoscaling alone. Thus, photosensitizers can improve the stability and performance of these devices by preventing photocorrosion and extending the light absorption range into the visible and infrared regions of the solar spectrum. In this work, carbon-based NM photosensitizers are shown to be excellent candidates to functionalize SC because they are

not only made from Earth-abundant elements, but their absorption and redox potentials can be tuned by doping or surface treatments to target specific photocatalytic transformations. Here, the engineering of a ZnO NW-CD heterogenous photocatalyst to drive an α-arylation reaction was demonstrated. The energetics of the system were studied to align the redox potential of the interfaces coming together in order to conceive a favorable driving force for the electron transfer processes, an approach often overlooked in the application of CD materials.

Due to their cost effectiveness and tunable optical properties, carbon-based photosensitizers render themselves advantageous over the use of bare SCs in devices. However, there are some complications when it comes to the tuning of their optical properties since these materials have unknown formation pathways. Gaining an understanding of their formation mechanism is a key factor that will play a major role in their final structure and thus, their optical properties. The use of inorganic metal chalcogenide NCs for photocatalytic purposes has been explored recently as a new approach to work in conjunction with carbon-based devices. Such materials can have additional advantages over carbon-based sensitizers due to their known crystalline composition and accessible formation mechanisms. The understanding of their formation mechanisms can help inform the design of better synthetic tools to tune their properties and catalytic efficiencies given the strict relationship between structure and function.

The LaMer burst nucleation or CNT provides the foundation to understanding homogeneous nucleation and growth of a narrow size distribution of colloids.[54] Sugimoto extended this theory and predicted that the number of nuclei generated during phase II of CNT depends solely on the solute supply rate and growth rate.[63] Nonetheless, nucleation kinetics were not taken into account in this model. Chu, Owen and Peters revealed that the number of

nuclei generated does not depend on size considerations only, as suggested by CNT, but it is strictly related to the concentration of solute.[67] Also, they demonstrated how the nucleation kinetics determine the final size distribution of NCs. On the other hand, heterogenous nucleation usually follows non-classical formation mechanisms through the formation of metastable intermediates. These pathways include the formation of magic-sized clusters and pre-nucleation clusters, growth through aggregation or oriented attachment, Ostwald ripening, or a combination between CNT and a non-classical mechanism. At the same time, these intermediates generate free energy minima in the energetic landscape towards the formation of the final NCs.

The work in this thesis has contributed to the general understanding of the formation mechanisms in colloidal synthesis of inorganic NCs based on the synthesis of quaternary kesterite CZTS NCs. The reaction mechanism is speculated to happen through the generation of a copper sulfide-based intermediate. Subsequent cation exchange reactions form the final kesterite CZTS phase where Sn^{4+} and Zn^{2+} replace Cu^{+} ions in the lattice. Hence, the copper sulfide intermediate is acting as a template for the final NCs. In this regard, the intermediate could follow a classical nucleation picture while the cation exchange and NC growth step would involve the non-classical mechanism. This work demonstrates the significance and difficulty of synthesizing NMs with narrow size distributions. Furthermore, it highlights viable strategies to attain better control in such syntheses. Finally, the understanding of the formation mechanisms of NMs will open new avenues in the design and modification of photocatalyst for the production of solar fuels.

References

1. Osterloh, F. E., Inorganic Nanostructures for Photoelectrochemical and Photocatalytic Water Splitting. *Chem. Soc. Rev.* **2013,** *42* (6), 2294-2320.
2. Kelly, N. A., Hydrogen Production by Water Electrolysis. In *Advances in Hydrogen Production, Storage and Distribution*, Basile, A.; Iulianelli, A., Eds. Woodhead Publishing: 2014; pp 159-185.
3. Kunene, T.; Xiong, L.; Rosenthal, J., Solar-Powered Synthesis of Hydrocarbons from Carbon Dioxide and Water. *Proc. Natl. Acad. Sci.* **2019,** *116* (20), 9693-9695.
4. Zhou, H.; Yu, F.; Zhu, Q.; Sun, J.; Qin, F.; Yu, L.; Bao, J.; Yu, Y.; Chen, S.; Ren, Z., Water Splitting by Electrolysis at High Current Densities Under 1.6 volts. *Energy Environ. Sci.* **2018,** *11* (10), 2858-2864.
5. Smestad, G. P.; Steinfeld, A., Review: Photochemical and Thermochemical Production of Solar Fuels from H2O and CO2 Using Metal Oxide Catalysts. *Ind. Eng. Chem. Res.* **2012,** *51* (37), 11828-11840.
6. Spitler, M. T.; Modestino, M. A.; Deutsch, T. G.; Xiang, C. X.; Durrant, J. R.; Esposito, D. V.; Haussener, S.; Maldonado, S.; Sharp, I. D.; Parkinson, B. A.; Ginley, D. S.; Houle, F. A.; Hannappel, T.; Neale, N. R.; Nocera, D. G.; McIntyre, P. C., Practical Challenges in the Development of Photoelectrochemical Solar Fuels Production. *Sustain. Energy Fuels* **2020,** *4* (3), 985-995.
7. Walter, M. G.; Warren, E. L.; McKone, J. R.; Boettcher, S. W.; Mi, Q.; Santori, E. A.; Lewis, N. S., Solar Water Splitting Cells. *Chem. Rev.* **2010,** *110* (11), 6446-6473.
8. Varadhan, P.; Fu, H.-C.; Kao, Y.-C.; Horng, R.-H.; He, J.-H., An Efficient and Stable Photoelectrochemical System with 9% Solar-to-Hydrogen Conversion Efficiency via InGaP/GaAs Double Junction. *Nat. Commun.* **2019,** *10* (1), 5282.
9. Khaselev, O.; Turner, J. A., A Monolithic Photovoltaic-Photoelectrochemical Device for Hydrogen Production via Water Splitting. *Science* **1998,** *280* (5362), 425-427.
10. Peharz, G.; Dimroth, F.; Wittstadt, U., Solar Hydrogen Production by Water Splitting with a Conversion Efficiency of 18%. *Int. J. Hydrogen Energy* **2007,** *32* (15), 3248-3252.
11. Moniz, S. J. A.; Shevlin, S. A.; Martin, D. J.; Guo, Z.-X.; Tang, J., Visible-Light Driven Heterojunction Photocatalysts for Water Splitting – A Critical Review. *Energy Environ. Sci.* **2015,** *8* (3), 731-759.
12. Gong, J.; Sumathy, K.; Qiao, Q.; Zhou, Z., Review on Dye-Sensitized Solar Cells (DSSCs): Advanced Techniques and Research Trends. *Renew. Sust. Energ. Rev.* **2017,** *68*, 234-246.
13. Bard, A. J.; Faulkner, L. R., *Electrochemical Methods: Fundamentals and Applications*. Wiley: 2000.
14. Sivula, K.; van de Krol, R., Semiconducting Materials for Photoelectrochemical Energy Conversion. *Nat. Rev. Mater.* **2016,** *1* (2), 15010.
15. Saito, K.; Koga, K.; Kudo, A., Lithium Niobate Nanowires for Photocatalytic Water Splitting. *Dalton Trans.* **2011,** *40* (15), 3909-3913.
16. Yan, S.; Wan, L.; Li, Z.; Zou, Z., Facile Temperature-Controlled Synthesis of Hexagonal Zn2GeO4 Nanorods with Different Aspect Ratios Toward Improved Photocatalytic Activity for Overall Water Splitting and Photoreduction of CO2. *Chem. Commun.* **2011,** *47* (19), 5632-5634.
17. Alonso-Vante, N.; Ern, V.; Chartier, P., Spectral Sensitization of Semiconductors by Copper (I) Complexes in Photoelectrochemical Systems. *Nouv J Chim* **1983,** *7*, 3-5.
18. O'Regan, B.; Grätzel, M., A Low-Cost, High-Efficiency Solar Cell Based on Dye-Sensitized Colloidal TiO2 Films. *Nature* **1991,** *353* (6346), 737-740.
19. Cowan, A. J.; Tang, J.; Leng, W.; Durrant, J. R.; Klug, D. R., Water Splitting by Nanocrystalline TiO2 in a Complete Photoelectrochemical Cell Exhibits Efficiencies Limited by Charge Recombination. *J. Phys. Chem. C* **2010,** *114* (9), 4208-4214.

20. Amano, F.; Nogami, K.; Tanaka, M.; Ohtani, B., Correlation Between Surface Area and Photocatalytic Activity for Acetaldehyde Decomposition Over Bismuth Tungstate Particles with a Hierarchical Structure. *Langmuir* **2010,** *26* (10), 7174-7180.
21. Wu, J.; Chen, S.; Seeds, A.; Liu, H., Quantum Dot Optoelectronic Devices: Lasers, Photodetectors and Solar Cells. *J. Phys. D: Appl. Phys.* **2015,** *48* (36), 363001.
22. Holmes, M. A.; Townsend, T. K.; Osterloh, F. E., Quantum Confinement Controlled Photocatalytic Water Splitting by Suspended CdSe nanocrystals. *Chem. Commun.* **2012,** *48* (3), 371-373.
23. Marcus, R. A., Chemical and Electrochemical Electron-Transfer Theory. *Annu. Rev. Phys. Chem.* **1964,** *15* (1), 155-196.
24. Würfel, P., *Physics of Solar Cells: From Basic Principles to Advanced Concepts*. Wiley: 2009.
25. Cesar, I.; Sivula, K.; Kay, A.; Zboril, R.; Grätzel, M., Influence of Feature Size, Film Thickness, and Silicon Doping on the Performance of Nanostructured Hematite Photoanodes for Solar Water Splitting. *J. Phys. Chem. C* **2009,** *113* (2), 772-782.
26. Liu, R.; Zheng, Z.; Spurgeon, J.; Yang, X., Enhanced Photoelectrochemical Water-Splitting Performance of Semiconductors by Surface Passivation Layers. *Energy Environ. Sci.* **2014,** *7* (8), 2504-2517.
27. Hodes, G., Nanocrystalline Photoelectrochemical Cells. *J. Electrochem. Soc.* **1992,** *139* (11), 3136.
28. Section 10 - Solar. In *Handbook of Energy*, Cleveland, C. J.; Morris, C., Eds. Elsevier: Amsterdam, 2013; pp 405-450.
29. Harlang, T. C. B.; Liu, Y.; Gordivska, O.; Fredin, L. A.; Ponseca, C. S.; Huang, P.; Chábera, P.; Kjaer, K. S.; Mateos, H.; Uhlig, J.; Lomoth, R.; Wallenberg, R.; Styring, S.; Persson, P.; Sundström, V.; Wärnmark, K., Iron Sensitizer Converts Light to Electrons with 92% Yield. *Nature Chem.* **2015,** *7* (11), 883-889.
30. Zeng, W.; Cao, Y.; Bai, Y.; Wang, Y.; Shi, Y.; Zhang, M.; Wang, F.; Pan, C.; Wang, P., Efficient Dye-Sensitized Solar Cells with an Organic Photosensitizer Featuring Orderly Conjugated Ethylenedioxythiophene and Dithienosilole Blocks. *Chem. Mater.* **2010,** *22* (5), 1915-1925.
31. Mubeen, S.; Hernandez-Sosa, G.; Moses, D.; Lee, J.; Moskovits, M., Plasmonic Photosensitization of a Wide Band Gap Semiconductor: Converting Plasmons to Charge Carriers. *Nano Lett.* **2011,** *11* (12), 5548-5552.
32. Wang, C.-I.; Wu, W.-C.; Periasamy, A. P.; Chang, H.-T., Electrochemical Synthesis of Photoluminescent Carbon Nanodots from Glycine for Highly Sensitive Detection of Hemoglobin. *Green Chem.* **2014,** *16* (5), 2509-2514.
33. Reyes, D.; Camacho, M.; Camacho, M.; Mayorga, M.; Weathers, D.; Salamo, G.; Wang, Z.; Neogi, A., Laser Ablated Carbon Nanodots for Light Emission. *Nanoscale Res. Lett.* **2016,** *11* (1), 424.
34. Su, Y.; Xie, M.; Lu, X.; Wei, H.; Geng, H.; Yang, Z.; Zhang, Y., Facile Synthesis and Photoelectric Properties of Carbon Dots with Upconversion Fluorescence Using Arc-Synthesized Carbon By-Products. *RSC Advances* **2014,** *4* (10), 4839-4842.
35. Zhang, Y.; Li, K.; Ren, S.; Dang, Y.; Liu, G.; Zhang, R.; Zhang, K.; Long, X.; Jia, K., Coal-Derived Graphene Quantum Dots Produced by Ultrasonic Physical Tailoring and Their Capacity for Cu(II) Detection. *ACS Sustain. Chem. Eng.* **2019,** *7* (11), 9793-9799.
36. Liu, H.; Ye, T.; Mao, C., Fluorescent Carbon Nanoparticles Derived from Candle Soot. *Angew. Chem. Int. Ed.* **2007,** *46* (34), 6473-6475.
37. Yarur, F.; Macairan, J.-R.; Naccache, R., Ratiometric Detection of Heavy Metal Ions Using Fluorescent Carbon Dots. *Environ. Sci. Nano* **2019,** *6* (4), 1121-1130.
38. Xia, J.; Chen, S.; Zou, G.-Y.; Yu, Y.-L.; Wang, J.-H., Synthesis of Highly Stable Red-Emissive Carbon Polymer Dots by Modulated Polymerization: from the Mechanism to Application in Intracellular pH Imaging. *Nanoscale* **2018,** *10* (47), 22484-22492.

39. Wang, Y.; Chang, X.; Jing, N.; Zhang, Y., Hydrothermal Synthesis of Carbon Quantum Dots as Fluorescent Probes for the Sensitive and Rapid Detection of Picric Acid. *Anal. Methods* **2018,** *10* (23), 2775-2784.
40. Wang, S.; Chen, Z.-G.; Cole, I.; Li, Q., Structural Evolution of Graphene Quantum Dots During Thermal Decomposition of Citric Acid and the Corresponding Photoluminescence. *Carbon* **2015,** *82*, 304-313.
41. Essner, J. B.; Baker, G. A., The Emerging Roles of Carbon Dots in Solar Photovoltaics: A Critical Review. *Environ. Sci. Nano* **2017,** *4* (6), 1216-1263.
42. Kagan, C. R.; Lifshitz, E.; Sargent, E. H.; Talapin, D. V., Building Devices from Colloidal Quantum Dots. *Science* **2016,** *353* (6302), aac5523.
43. H. Sargent, E., Infrared Quantum Dots. *Adv. Mater.* **2005,** *17* (5), 515-522.
44. Qiu, F.; Han, Z.; Peterson, J. J.; Odoi, M. Y.; Sowers, K. L.; Krauss, T. D., Photocatalytic Hydrogen Generation by CdSe/CdS Nanoparticles. *Nano Lett.* **2016,** *16* (9), 5347-5352.
45. Ghorpade, U.; Suryawanshi, M.; Shin, S. W.; Gurav, K.; Patil, P.; Pawar, S.; Hong, C. W.; Kim, J. H.; Kolekar, S., Towards Environmentally Benign Approaches for the Synthesis of CZTSSe Nanocrystals by a hot Injection Method: a Status Review. *Chem. Commun.* **2014,** *50* (77), 11258-11273.
46. Nitsche, R.; Sargent, D. F.; Wild, P., Crystal Growth of Quaternary 12_246_4 Chalcogenides by Iodine Vapor Transport. *J. Cryst. Growth* **1967,** *1* (1), 52-53.
47. Simya, O. K.; Geetha Priyadarshini, B.; Balachander, K.; Ashok, A. M., Formation of a Phase Pure Kesterite CZTSe Thin Films Using Multisource Hybrid Physical Vapour Deposition. *Mater. Res. Express* **2020,** *7* (1), 016419.
48. Liu, F.; Huang, J.; Sun, K.; Yan, C.; Shen, Y.; Park, J.; Pu, A.; Zhou, F.; Liu, X.; Stride, J. A.; Green, M. A.; Hao, X., Beyond 8% Ultrathin Kesterite Cu2ZnSnS4 Solar Cells by Interface Reaction Route Controlling and Self-Organized Nanopattern at the Back Contact. *NPG Asia Mater.* **2017,** *9* (7), e401-e401.
49. Khattak, Y. H.; Baig, F.; Toura, H.; Harabi, I.; Beg, S.; Soucase, B. M., Single Step Electrochemical Deposition for the Fabrication of CZTS Kesterite Thin Films for Solar Cells. *Appl. Surf. Sci.* **2019,** *497*, 143794.
50. Stroyuk, O.; Raevskaya, A.; Selyshchev, O.; Dzhagan, V.; Gaponik, N.; Zahn, D. R. T.; Eychmüller, A., "Green" Aqueous Synthesis and Advanced Spectral Characterization of Size-Selected Cu2ZnSnS4 Nanocrystal Inks. *Scientific Reports* **2018,** *8* (1), 13677.
51. Green, P. B.; Narayanan, P.; Li, Z.; Sohn, P.; Imperiale, C. J.; Wilson, M. W. B., Controlling Cluster Intermediates Enables the Synthesis of Small PbS Nanocrystals with Narrow Ensemble Line Widths. *Chem. Mater.* **2020,** *32* (9), 4083-4094.
52. Gary, D. C.; Terban, M. W.; Billinge, S. J. L.; Cossairt, B. M., Two-Step Nucleation and Growth of InP Quantum Dots via Magic-Sized Cluster Intermediates. *Chem. Mater.* **2015,** *27* (4), 1432-1441.
53. Wang, F.; Richards, V. N.; Shields, S. P.; Buhro, W. E., Kinetics and Mechanisms of Aggregative Nanocrystal Growth. *Chem. Mater.* **2014,** *26* (1), 5-21.
54. LaMer, V. K.; Dinegar, R. H., Theory, Production and Mechanism of Formation of Monodispersed Hydrosols. *J. Am. Chem. Soc.* **1950,** *72* (11), 4847-4854.
55. Chow, M. K.; Zukoski, C. F., Gold Sol Formation Mechanisms: Role of Colloidal Stability. *J. Colloid Interface Sci.* **1994,** *165* (1), 97-109.
56. Zheng, H.; Smith, R. K.; Jun, Y.-w.; Kisielowski, C.; Dahmen, U.; Alivisatos, A. P., Observation of Single Colloidal Platinum Nanocrystal Growth Trajectories. *Science* **2009,** *324* (5932), 1309-1312.
57. Finney, E. E.; Shields, S. P.; Buhro, W. E.; Finke, R. G., Gold Nanocluster Agglomeration Kinetic Studies: Evidence for Parallel Bimolecular Plus Autocatalytic Agglomeration Pathways as a Mechanism-Based Alternative to an Avrami-Based Analysis. *Chem. Mater.* **2012,** *24* (10), 1718-1725.

58. Tang, Z.; Kotov, N. A.; Giersig, M., Spontaneous Organization of Single CdTe Nanoparticles into Luminescent Nanowires. *Science* **2002,** *297* (5579), 237-240.
59. Erdemir, D.; Lee, A. Y.; Myerson, A. S., Nucleation of Crystals from Solution: Classical and Two-Step Models. *Acc. Chem. Res.* **2009,** *42* (5), 621-629.
60. Gebauer, D.; Völkel, A.; Cölfen, H., Stable Prenucleation Calcium Carbonate Clusters. *Science* **2008,** *322* (5909), 1819-1822.
61. Baronov, A.; Bufkin, K.; Shaw, D. W.; Johnson, B. L.; Patrick, D. L., A Simple Model of Burst Nucleation. *PCCP* **2015,** *17* (32), 20846-20852.
62. Jiang, Z.-J.; Kelley, D. F., Role of Magic-Sized Clusters in the Synthesis of CdSe Nanorods. *ACS Nano* **2010,** *4* (3), 1561-1572.
63. Sugimoto, T., Preparation of Monodispersed Colloidal Particles. *Adv. Colloid Interface Sci.* **1987,** *28*, 65-108.
64. Sugimoto, T.; Shiba, F.; Sekiguchi, T.; Itoh, H., Spontaneous Nucleation of Monodisperse Silver Halide Particles from Homogeneous Gelatin Solution I: Silver Chloride. *Colloid. Surface. A.* **2000,** *164* (2), 183-203.
65. Hendricks, M. P.; Campos, M. P.; Cleveland, G. T.; Jen-La Plante, I.; Owen, J. S., A Tunable Library of Substituted Thiourea Precursors to Metal Sulfide Nanocrystals. *Science* **2015,** *348* (6240), 1226-1230.
66. Campos, M. P.; Hendricks, M. P.; Beecher, A. N.; Walravens, W.; Swain, R. A.; Cleveland, G. T.; Hens, Z.; Sfeir, M. Y.; Owen, J. S., A Library of Selenourea Precursors to PbSe Nanocrystals with Size Distributions near the Homogeneous Limit. *J. Am. Chem. Soc.* **2017,** *139* (6), 2296-2305.
67. Chu, D. B. K.; Owen, J. S.; Peters, B., Nucleation and Growth Kinetics from LaMer Burst Data. *J. Phys. Chem. A* **2017,** *121* (40), 7511-7517.
68. Grogan, J. M.; Rotkina, L.; Bau, H. H., In Situ Liquid-Cell Electron Microscopy of Colloid Aggregation and Growth Dynamics. *Phys. Rev. E.* **2011,** *83* (6), 061405.
69. Evans, J. E.; Jungjohann, K. L.; Browning, N. D.; Arslan, I., Controlled Growth of Nanoparticles from Solution with In Situ Liquid Transmission Electron Microscopy. *Nano Lett.* **2011,** *11* (7), 2809-2813.
70. Xin, H. L.; Zheng, H., In Situ Observation of Oscillatory Growth of Bismuth Nanoparticles. *Nano Lett.* **2012,** *12* (3), 1470-1474.
71. Lee, J.; Yang, J.; Kwon, S. G.; Hyeon, T., Nonclassical Nucleation and Growth of Inorganic Nanoparticles. *Nat. Rev. Mater.* **2016,** *1* (8), 16034.
72. Huang, F.; Zhang, H.; Banfield, J. F., Two-Stage Crystal-Growth Kinetics Observed during Hydrothermal Coarsening of Nanocrystalline ZnS. *Nano Lett.* **2003,** *3* (3), 373-378.
73. Zhang, J.; Lin, Z.; Lan, Y.; Ren, G.; Chen, D.; Huang, F.; Hong, M., A Multistep Oriented Attachment Kinetics: Coarsening of ZnS Nanoparticle in Concentrated NaOH. *J. Am. Chem. Soc.* **2006,** *128* (39), 12981-12987.
74. Lee Penn, R.; Tanaka, K.; Erbs, J., Size Dependent Kinetics of Oriented Aggregation. *J. Cryst. Growth* **2007,** *309* (1), 97-102.
75. Burrows, N. D.; Hale, C. R. H.; Penn, R. L., Effect of Ionic Strength on the Kinetics of Crystal Growth by Oriented Aggregation. *Cryst. Growth Des.* **2012,** *12* (10), 4787-4797.
76. Liao, H.-G.; Cui, L.; Whitelam, S.; Zheng, H., Real-Time Imaging of Pt_3Fe Nanorod Growth in Solution. *Science* **2012,** *336* (6084), 1011-1014.
77. Zheng, X., Simulation of Bimodal Size Distributions for Coarsening. *Z. Phys. B. Condens. Matter.* **1994,** *93* (4), 501-507.
78. Sanzone, A.; Mattiello, S.; Garavaglia, G. M.; Calascibetta, A. M.; Ceriani, C.; Sassi, M.; Beverina, L., Efficient synthesis of organic semiconductors by Suzuki–Miyaura coupling in an aromatic micellar medium. *Green Chem.* **2019,** *21* (16), 4400-4405.
79. Jiang, W.; Li, Y.; Wang, Z., Heteroarenes as high performance organic semiconductors. *Chem. Soc. Rev.* **2013,** *42* (14), 6113-6127.

80. Mohanty, A. D.; Lee, Y.-B.; Zhu, L.; Hickner, M. A.; Bae, C., Anion Exchange Fuel Cell Membranes Prepared from C–H Borylation and Suzuki Coupling Reactions. *Macromolecules* **2014,** *47* (6), 1973-1980.
81. He, C.; Hao, J.; Xu, H.; Mo, Y.; Liu, H.; Han, J.; Lei, A., Heteroaromatic Imidazo[1,2-a]pyridines Synthesis from C–H/N–H Oxidative Cross-Coupling/Cyclization. *Chem. Commun.* **2012,** *48* (90), 11073-11075.
82. Colmenares, J. C.; Luque, R., Heterogeneous Photocatalytic Nanomaterials: Prospects and Challenges in Selective Transformations of Biomass-Derived Compounds. *Chem. Soc. Rev.* **2014,** *43* (3), 765-778.
83. Artero, V.; Fontecave, M., Solar Fuels Generation and Molecular Systems: Is it Homogeneous or Heterogeneous Catalysis? *Chem. Soc. Rev.* **2013,** *42* (6), 2338-2356.
84. Hooshmand, S. E.; Heidari, B.; Sedghi, R.; Varma, R. S., Recent Advances in the Suzuki–Miyaura Cross-Coupling Reaction Using Efficient Catalysts in Eco-Friendly Media. *Green Chem.* **2019,** *21* (3), 381-405.
85. Pethő, B.; Vangel, D.; Csenki, J. T.; Zwillinger, M.; Novák, Z., Palladium Catalyzed Chloroethoxylation of Aromatic and Heteroaromatic Chlorides: an Orthogonal Functionalization of a Chloroethoxy Linker. *Org. Biomol. Chem.* **2018,** *16* (26), 4895-4899.
86. Jin, B.; Gallou, F.; Reilly, J.; Lipshutz, B. H., ppm Pd-Catalyzed, Cu-Free Sonogashira Couplings in Water Using Commercially Available Catalyst Precursors. *Chem. Sci.* **2019,** *10* (12), 3481-3485.
87. Long, R.; Huang, H.; Li, Y.; Song, L.; Xiong, Y., Palladium-Based Nanomaterials: A Platform to Produce Reactive Oxygen Species for Catalyzing Oxidation Reactions. *Adv. Mater.* **2015,** *27* (44), 7025-7042.
88. Zhang, Z.; Richrath, R. B.; Gansäuer, A., Merging Catalysis in Single Electron Steps with Photoredox Catalysis—Efficient and Sustainable Radical Chemistry. *ACS Catal.* **2019,** *9* (4), 3208-3212.
89. Stache, E. E.; Ertel, A. B.; Rovis, T.; Doyle, A. G., Generation of Phosphoranyl Radicals via Photoredox Catalysis Enables Voltage–Independent Activation of Strong C–O Bonds. *ACS Catal.* **2018,** *8* (12), 11134-11139.
90. Cai, Y.; Tang, Y.; Fan, L.; Lefebvre, Q.; Hou, H.; Rueping, M., Heterogeneous Visible-Light Photoredox Catalysis with Graphitic Carbon Nitride for α-Aminoalkyl Radical Additions, Allylations, and Heteroarylations. *ACS Catal.* **2018,** *8* (10), 9471-9476.
91. Ghogare, A. A.; Greer, A., Using Singlet Oxygen to Synthesize Natural Products and Drugs. *Chem. Rev.* **2016,** *116* (17), 9994-10034.
92. Rehman, S.; Ullah, R.; Butt, A. M.; Gohar, N. D., Strategies of Making TiO2 and ZnO Visible Light Active. *J. Hazard. Mater.* **2009,** *170* (2-3), 560-9.
93. Camussi, I.; Mannucci, B.; Speltini, A.; Profumo, A.; Milanese, C.; Malavasi, L.; Quadrelli, P., g-C3N4 - Singlet Oxygen Made Easy for Organic Synthesis: Scope and Limitations. *ACS Sustain. Chem. Eng.* **2019,** *7* (9), 8176-8182.
94. Xu, X.; Luo, F.; Tang, W.; Hu, J.; Zeng, H.; Zhou, Y., Enriching Hot Electrons via NIR-Photon-Excited Plasmon in WS2@Cu Hybrids for Full-Spectrum Solar Hydrogen Evolution. *Adv. Funct. Mater.* **2018,** *28* (43), 1804055.
95. Yuan, J.; Wen, J.; Gao, Q.; Chen, S.; Li, J.; Li, X.; Fang, Y., Amorphous Co3O4 Modified CdS Nanorods with Enhanced Visible-Light Photocatalytic H2-Production Activity. *Dalton Trans.* **2015,** *44* (4), 1680-1689.
96. Rand, B. P.; Burk, D. P.; Forrest, S. R., Offset Energies at Organic Semiconductor Heterojunctions and their Influence on the Open-Circuit Voltage of Thin-Film Solar Cells. *Phys. Rev. B.* **2007,** *75* (11), 115327.
97. Li, X.; Yu, J.; Jaroniec, M., Hierarchical Photocatalysts. *Chem. Soc. Rev.* **2016,** *45* (9), 2603-2636.

98. Greene, L. E.; Yuhas, B. D.; Law, M.; Zitoun, D.; Yang, P., Solution-Grown Zinc Oxide Nanowires. *Inorg. Chem.* **2006,** *45* (19), 7535-7543.
99. Zhang, Q.; Dandeneau, C. S.; Zhou, X.; Cao, G., ZnO Nanostructures for Dye-Sensitized Solar Cells. *Adv. Mater.* **2009,** *21* (41), 4087-4108.
100. Bora, T.; Zoepfl, D.; Dutta, J., Importance of Plasmonic Heating on Visible Light Driven Photocatalysis of Gold Nanoparticle Decorated Zinc Oxide Nanorods. *Scientific Reports* **2016,** *6*, 26913.
101. Šutka, A.; Käämbre, T.; Pärna, R.; Juhnevica, I.; Maiorov, M.; Joost, U.; Kisand, V., Co Doped ZnO Nanowires as Visible Light Photocatalysts. *Solid State Sci.* **2016,** *56*, 54-62.
102. Unalan, H. E.; Wei, D.; Suzuki, K.; Dalal, S.; Hiralal, P.; Matsumoto, H.; Imaizumi, S.; Minagawa, M.; Tanioka, A.; Flewitt, A. J.; Milne, W. I.; Amaratunga, G. A. J., Photoelectrochemical cell using dye sensitized zinc oxide nanowires grown on carbon fibers. *Appl. Phys. Lett.* **2008,** *93* (13), 133116.
103. Kadi, M. W.; McKinney, D.; Mohamed, R. M.; Mkhalid, I. A.; Sigmund, W., Fluorine Doped Zinc Oxide Nanowires: Enhanced Photocatalysts Degrade Malachite Green Dye Under Visible Light Conditions. *Ceram. Int.* **2016,** *42* (4), 4672-4678.
104. Guo, C. X.; Dong, Y.; Yang, H. B.; Li, C. M., Graphene Quantum Dots as a Green Sensitizer to Functionalize ZnO Nanowire Arrays on F-Doped SnO2 Glass for Enhanced Photoelectrochemical Water Splitting. *Adv. Energy Mater.* **2013,** *3* (8), 997-1003.
105. Lee, C.-P.; Chou, C.-Y.; Chen, C.-Y.; Yeh, M.-H.; Lin, L.-Y.; Vittal, R.; Wu, C.-G.; Ho, K.-C., Zinc Oxide-Based Dye-Sensitized Solar Cells with a Ruthenium Dye Containing an Alkyl Bithiophene Group. *J. Power Sources* **2014,** *246*, 1-9.
106. Zhang, X.; Cappel, U. B.; Jia, D.; Zhou, Q.; Du, J.; Sloboda, T.; Svanström, S.; Johansson, F. O. L.; Lindblad, A.; Giangrisostomi, E.; Ovsyannikov, R.; Liu, J.; Rensmo, H.; Gardner, J. M.; Johansson, E. M. J., Probing and Controlling Surface Passivation of PbS Quantum Dot Solid for Improved Performance of Infrared Absorbing Solar Cells. *Chem. Mater.* **2019,** *31* (11), 4081-4091.
107. Briscoe, J.; Marinovic, A.; Sevilla, M.; Dunn, S.; Titirici, M., Biomass-Derived Carbon Quantum Dot Sensitizers for Solid-State Nanostructured Solar Cells. *Angew. Chem. Int. Ed.* **2015,** *54* (15), 4463-4468.
108. Macina, A.; de Medeiros, T. V.; Naccache, R., A carbon dot-catalyzed transesterification reaction for the production of biodiesel. *J. Mater. Chem. A.* **2019,** *7* (41), 23794-23802.
109. Ding, H.; Yu, S.-B.; Wei, J.-S.; Xiong, H.-M., Full-Color Light-Emitting Carbon Dots with a Surface-State-Controlled Luminescence Mechanism. *ACS Nano* **2016,** *10* (1), 484-491.
110. Manioudakis, J.; Victoria, F.; Thompson, C. A.; Brown, L.; Movsum, M.; Lucifero, R.; Naccache, R., Effects of Nitrogen-Doping on the Photophysical Properties of Carbon Dots. *J. Mater. Chem. C.* **2019,** *7* (4), 853-862.
111. Wang, R.; Lu, K.-Q.; Tang, Z.-R.; Xu, Y.-J., Recent progress in carbon quantum dots: synthesis, properties and applications in photocatalysis. *J. Mater. Chem. A.* **2017,** *5* (8), 3717-3734.
112. Hazarika, D.; Karak, N., Photocatalytic Degradation of Organic Contaminants Under Solar Light Using Carbon Dot/Titanium Dioxide Nanohybrid, Obtained Through a Facile Approach. *Appl. Surf. Sci.* **2016,** *376*, 276-285.
113. Xu, X.; Bao, Z.; Tang, W.; Wu, H.; Pan, J.; Hu, J.; Zeng, H., Surface States Engineering Carbon dots as Multi-Band Light Active Sensitizers for ZnO Nanowire Array Photoanode to Boost Solar Water Splitting. *Carbon* **2017,** *121*, 201-208.
114. Hutton, G. A. M.; Reuillard, B.; Martindale, B. C. M.; Caputo, C. A.; Lockwood, C. W. J.; Butt, J. N.; Reisner, E., Carbon Dots as Versatile Photosensitizers for Solar-Driven Catalysis with Redox Enzymes. *J. Am. Chem. Soc.* **2016,** *138* (51), 16722-16730.
115. Omer, K. M.; Mohammad, N. N.; Baban, S. O., Up-Conversion Fluorescence of Phosphorous and Nitrogen Co-Doped Carbon Quantum Dots (CDs) Coupled with Weak LED Light Source for Full-Spectrum Driven Photocatalytic Degradation via ZnO-CDs Nanocomposites. *Catal. Lett.* **2018,** *148* (9), 2746-2755.

116. Zhu, M.; Deng, X.; Lin, X.; Zhang, L.; Zhang, W.; Lv, Y.; Pan, J., The carbon quantum dots modified ZnO/TiO2 nanotube heterojunction and its visible light photocatalysis enhancement. *J. Mater. Sci.: Mater. Electron.* **2018,** *29* (13), 11449-11456.
117. Barman, M. K.; Mitra, P.; Bera, R.; Das, S.; Pramanik, A.; Parta, A., An Efficient Charge Separation and Photocurrent Generation in the Carbon Dot–Zinc Oxide Nanoparticle Composite. *Nanoscale* **2017,** *9* (20), 6791-6799.
118. Suzuki, K.; Malfatti, L.; Carboni, D.; Loche, D.; Casula, M.; Moretto, A.; Maggini, M.; Takahashi, M.; Innocenzi, P., Energy Transfer Induced by Carbon Quantum Dots in Porous Zinc Oxide Nanocomposite Films. *J. Phys. Chem. C* **2015,** *119* (5), 2837-2843.
119. Low, J.; Yu, J.; Jaroniec, M.; Wageh, S.; Al-Ghamdi, A. A., Heterojunction Photocatalysts. *Adv. Mater.* **2017,** *29* (20), 1601694.
120. Wang, M.; Cai, L.; Wang, Y.; Zhou, F.; Xu, K.; Tao, X.; Chai, Y., Graphene-Draped Semiconductors for Enhanced Photocorrosion Resistance and Photocatalytic Properties. *J. Am. Chem. Soc.* **2017,** *139* (11), 4144-4151.
121. Lim, S. Y.; Shen, W.; Gao, Z., Carbon Quantum Dots and Their Applications. *Chem. Soc. Rev.* **2015,** *44* (1), 362-381.
122. Omri, K.; Alyamani, A.; El Mir, L., Surface morphology, microstructure and electrical properties of Ca-doped ZnO thin films. *J. Mater. Sci.: Mater. Electron.* **2019,** *30* (17), 16606-16612.
123. Tian, Z. R.; Voigt, J. A.; Liu, J.; McKenzie, B.; McDermott, M. J.; Rodriguez, M. A.; Konishi, H.; Xu, H., Complex and Oriented ZnO Nanostructures. *Nat. Mater.* **2003,** *2* (12), 821-826.
124. Dong, Y.; Pang, H.; Yang, H. B.; Guo, C.; Shao, J.; Chi, Y.; Li, C. M.; Yu, T., Carbon-Based Dots Co-doped with Nitrogen and Sulfur for High Quantum Yield and Excitation-Independent Emission. *Angew. Chem. Int. Ed.* **2013,** *52* (30), 7800-7804.
125. Sahu, S.; Behera, B.; Maiti, T. K.; Mohapatra, S., Simple One-Step Synthesis of Highly Luminescent Carbon Dots from Orange Juice: Application as Excellent Bio-Imaging Agents. *Chem. Commun.* **2012,** *48* (70), 8835-8837.
126. Song, Y.; Zhu, S.; Zhang, S.; Fu, Y.; Wang, L.; Zhao, X.; Yang, B., Investigation from chemical structure to photoluminescent mechanism: a type of carbon dots from the pyrolysis of citric acid and an amine. *J. Mater. Chem. C.* **2015,** *3* (23), 5976-5984.
127. Wang, W.; Wang, B.; Embrechts, H.; Damm, C.; Cadranel, A.; Strauss, V.; Distaso, M.; Hinterberger, V.; Guldi, D. M.; Peukert, W., Shedding light on the effective fluorophore structure of high fluorescence quantum yield carbon nanodots. *RSC Advances* **2017,** *7* (40), 24771-24780.
128. Pan, L.; Sun, S.; Zhang, L.; Jiang, K.; Lin, H., Near-Infrared Emissive Carbon Dots for Two-Photon Fluorescence Bioimaging. *Nanoscale* **2016,** *8* (39), 17350-17356.
129. Wang, Y.; Wöll, C., IR Spectroscopic Investigations of Chemical and Photochemical Reactions on Metal Oxides: Bridging the Materials Gap. *Chem. Soc. Rev.* **2017,** *46* (7), 1875-1932.
130. Dominguez, A.; Lorke, M.; Schoenhalz, A. L.; Rosa, A. L.; Frauenheim, T.; Rocha, A. R.; Dalpian, G. M., First principles investigations on the electronic structure of anchor groups on ZnO nanowires and surfaces. *J. Appl. Phys.* **2014,** *115* (20), 203720.
131. Moreira, N. H.; Rosa, A. L. d.; Frauenheim, T., Covalent functionalization of ZnO surfaces: A density functional tight binding study. *Appl. Phys. Lett.* **2009,** *94* (19), 193109.
132. Martsinovich, N.; Troisi, A., Theoretical studies of dye-sensitised solar cells: from electronic structure to elementary processes. *Energy Environ. Sci.* **2011,** *4* (11), 4473-4495.
133. Lu, Q.; Yu, Y.; Ma, Q.; Chen, B.; Zhang, H., 2D Transition-Metal-Dichalcogenide-Nanosheet-Based Composites for Photocatalytic and Electrocatalytic Hydrogen Evolution Reactions. *Adv. Mater.* **2016,** *28* (10), 1917-1933.
134. Shen, J.; Zhu, Y.; Yang, X.; Zong, J.; Zhang, J.; Li, C., One-Pot Hydrothermal Synthesis of Graphene Quantum Dots Surface-Passivated by Polyethylene Glycol and Their Photoelectric Conversion Under Near-Infrared Light. *New J. Chem.* **2012,** *36* (1), 97-101.

135. Pal, A.; Ghosh, I.; Sapra, S.; König, B., Quantum Dots in Visible-Light Photoredox Catalysis: Reductive Dehalogenations and C–H Arylation Reactions Using Aryl Bromides. *Chem. Mater.* **2017,** *29* (12), 5225-5231.
136. Sakai, J.; Miura, I.; Shibata, M.; Yonekura, N.; Hiyoshi, H.; Takagaki, M.; Nagayama, K., Development of a New Fungicide, Benthiavalicarb-Isopropyl. *Pestic. Sci.* **2010,** *35* (4), 488-489.
137. Solanki, P. V.; Uppelli, S. B.; Patil, R. B.; Dhokrat, P. A.; Bembalkar, S. R.; Mathad, V. T., Facile Synthesis of Dabigatran Etexilate Mesylate, an Anticoagulant Drug, Using a Novel Synthon, N-Hexyl-4-nitrophenyl Carbonate. *ACS Omega* **2018,** *3* (5), 5744-5753.
138. Donawho, C. K.; Luo, Y.; Luo, Y.; Penning, T. D.; Bauch, J. L.; Bouska, J. J.; Bontcheva-Diaz, V. D.; Cox, B. F.; DeWeese, T. L.; Dillehay, L. E.; Ferguson, D. C.; Ghoreishi-Haack, N. S.; Grimm, D. R.; Guan, R.; Han, E. K.; Holley-Shanks, R. R.; Hristov, B.; Idler, K. B.; Jarvis, K.; Johnson, E. F.; Kleinberg, L. R.; Klinghofer, V.; Lasko, L. M.; Liu, X.; Marsh, K. C.; McGonigal, T. P.; Meulbroek, J. A.; Olson, A. M.; Palma, J. P.; Rodriguez, L. E.; Shi, Y.; Stavropoulos, J. A.; Tsurutani, A. C.; Zhu, G.-D.; Rosenberg, S. H.; Giranda, V. L.; Frost, D. J., ABT-888, an Orally Active Poly(ADP-Ribose) Polymerase Inhibitor that Potentiates DNA-Damaging Agents in Preclinical Tumor Models. *Clinic. Cancer Res.* **2007,** *13* (9), 2728-2737.
139. Hauel, N. H.; Nar, H.; Priepke, H.; Ries, U.; Stassen, J.-M.; Wienen, W., Structure-Based Design of Novel Potent Nonpeptide Thrombin Inhibitors. *J. Med. Chem.* **2002,** *45* (9), 1757-1766.
140. Reuveni, M., Activity of the New Fungicide Benthiavalicarb Against Plasmopara viticola and its Efficacy in Controlling Downy Mildew in Grapevines. *Eur. J. Plant Pathol.* **2003,** *109* (3), 243-251.
141. Prier, C. K.; MacMillan, D. W. C., Amine α-Heteroarylation Via Photoredox Catalysis: a Homolytic Aromatic Substitution Pathway. *Chem. Sci.* **2014,** *5* (11), 4173-4178.
142. McNally, A.; Prier, C. K.; MacMillan, D. W. C., Discovery of an α-Amino C–H Arylation Reaction Using the Strategy of Accelerated Serendipity. *Science* **2011,** *334* (6059), 1114-1117.
143. Zhang, H.; Zong, R.; Zhu, Y., Photocorrosion Inhibition and Photoactivity Enhancement for Zinc Oxide via Hybridization with Monolayer Polyaniline. *J. Phys. Chem. C* **2009,** *113* (11), 4605-4611.
144. Arnaut, L.; Formosinho, S.; Burrows, H., 4 - Reaction Order and Rate Constants. In *Chemical Kinetics*, Arnaut, L.; Formosinho, S.; Burrows, H., Eds. Elsevier: Amsterdam, 2007; pp 77-113.
145. Kershaw, S. V.; Jing, L.; Huang, X.; Gao, M.; Rogach, A. L., Materials Aspects of Semiconductor Nanocrystals for Optoelectronic Applications. *Mater. Horiz.* **2017,** *4* (2), 155-205.
146. Menezes, S.; Samantilleke, A., Formation of Unique Nanocrystalline Cu-In-Se Bulk pn Homojunctions for Opto-Electronic Devices. *Scientific Reports* **2018,** *8* (1), 11350.
147. Kim, W. D.; Kim, J.-H.; Lee, S.; Lee, S.; Woo, J. Y.; Lee, K.; Chae, W.-S.; Jeong, S.; Bae, W. K.; McGuire, J. A.; Moon, J. H.; Jeong, M. S.; Lee, D. C., Role of Surface States in Photocatalysis: Study of Chlorine-Passivated CdSe Nanocrystals for Photocatalytic Hydrogen Generation. *Chem. Mater.* **2016,** *28* (3), 962-968.
148. Reiss, P.; Carrière, M.; Lincheneau, C.; Vaure, L.; Tamang, S., Synthesis of Semiconductor Nanocrystals, Focusing on Nontoxic and Earth-Abundant Materials. *Chem. Rev.* **2016,** *116* (18), 10731-10819.
149. Hages, C. J.; Koeper, M. J.; Miskin, C. K.; Brew, K. W.; Agrawal, R., Controlled Grain Growth for High Performance Nanoparticle-Based Kesterite Solar Cells. *Chem. Mater.* **2016,** *28* (21), 7703-7714.
150. Todorov, T. K.; Tang, J.; Bag, S.; Gunawan, O.; Gokmen, T.; Zhu, Y.; Mitzi, D. B., Beyond 11% Efficiency: Characteristics of State-of-the-Art Cu2ZnSn(S,Se)4 Solar Cells. *Adv. Energy Mater.* **2013,** *3* (1), 34-38.
151. Tan, J. M. R.; Lee, Y. H.; Pedireddy, S.; Baikie, T.; Ling, X. Y.; Wong, L. H., Understanding the Synthetic Pathway of a Single-Phase Quarternary Semiconductor Using Surface-Enhanced Raman Scattering: A Case of Wurtzite Cu2ZnSnS4 Nanoparticles. *J. Am. Chem. Soc.* **2014,** *136* (18), 6684-6692.

152. Q. Li, A. X. W., , W. K. Tao, J. Liu, Y. Zhao, Z. M. Xiao, Effect of Reaction Temperature and Reaction Time on the Properties of Cu2ZnSnS4 Nanocrystalline Thin Films Prepared by Microwave Irradiation. *Chalcogenide Lett.* **2017,** *14* (11), 465-474.
153. Isotta, E.; Pugno, N. M.; Scardi, P., Nanostructured Kesterite (Cu2ZnSnS4) for Applications in Thermoelectric Devices. *Powder Diffr.* **2019,** *34* (S1), S42-S47.
154. Suryawanshi, M.; Shin, S. W.; Bae, W. R.; Gurav, K.; Kang, M. G.; Agawane, G.; Patil, P.; Yun, J. H.; Lee, J. Y.; Moholkar, A.; Kim, J. H., Kesterite CZTS Nanocrystals: pH-Dependent Synthesis. *Phys. Status Solidi a* **2014,** *211* (7), 1531-1534.
155. Courel, M., An Approach Towards the Promotion of Kesterite Solar Cell Efficiency: The use of Nanostructures. *Appl. Phys. Lett.* **2019,** *115* (12), 123901.
156. Jain, S.; Singh, D.; Vijayan, N.; Sharma, S. N., Time-controlled synthesis mechanism analysis of kesterite-phased Cu2ZnSnS4 nanorods via colloidal route. *Appl. Nanosci.* **2018,** *8* (3), 435-446.
157. Nagoya, A.; Asahi, R.; Wahl, R.; Kresse, G., Defect Formation and Phase Stability of Cu_2ZnSnS_4 Photovoltaic Material. *Phys. Rev. B.* **2010,** *81* (11), 113202.
158. Burton, L. A.; Colombara, D.; Abellon, R. D.; Grozema, F. C.; Peter, L. M.; Savenije, T. J.; Dennler, G.; Walsh, A., Synthesis, Characterization, and Electronic Structure of Single-Crystal SnS, Sn2S3, and SnS2. *Chem. Mater.* **2013,** *25* (24), 4908-4916.
159. Coughlan, C.; Ryan, K. M., Complete Study of the Composition and Shape Evolution in the Synthesis of Cu2ZnSnS4 (CZTS) Semiconductor Nanocrystals. *CrystEngComm* **2015,** *17* (36), 6914-6922.
160. Yu, K.; Carter, E. A., A Strategy to Stabilize Kesterite CZTS for High-Performance Solar Cells. *Chem. Mater.* **2015,** *27* (8), 2920-2927.
161. Aruna-Devi, R.; Latha, M.; Velumani, S.; Santoyo-Salazar, J.; Santos-Cruz, J., Telescoping Synthesis and Goldilocks of CZTS Nanocrystals. *Mater. Res. Bull.* **2019,** *111*, 342-349.
162. S, A.; J, R. K.; S, M. B., Influence of Co-Ordinating and Non-Coordinating Solvents in Structural and Morphological Properties of Cu2ZnSnS4 (CZTS) Nanoparticles. *Optik* **2017,** *130*, 99-105.
163. Kim, Y.; Woo, K.; Kim, I.; Cho, Y. S.; Jeong, S.; Moon, J., Highly Concentrated Synthesis of Copper-Zinc-Tin-Sulfide Nanocrystals with Easily Decomposable Capping Molecules for Printed Photovoltaic Applications. *Nanoscale* **2013,** *5* (21), 10183-10188.
164. Mkawi, E. M.; Al-Hadeethi, Y.; Shalaan, E.; Bekyarova, E., Solution-Processed Sphere-Like Cu2ZnSnS4 Nanoparticles for Solar Cells: Effect of Oleylamine Concentration on Properties. *Appl. Phys. A* **2019,** *126* (1), 50.
165. Xie, R.; Rutherford, M.; Peng, X., Formation of High-Quality I−III−VI Semiconductor Nanocrystals by Tuning Relative Reactivity of Cationic Precursors. *J. Am. Chem. Soc.* **2009,** *131* (15), 5691-5697.
166. Cao, G. A. W., Ying, *Nanostructures and Nanomaterials: Synthesis, Properties, and Applications*. 2004; Vol. 3.
167. Pinto, A. H.; Shin, S. W.; Isaac, E.; Knutson, T. R.; Aydil, E. S.; Penn, R. L., Controlling Cu2ZnSnS4 (CZTS) Phase in Microwave Solvothermal Synthesis. *J. Mater. Chem. A.* **2017,** *5* (44), 23179-23189.
168. Hou, B.; Benito-Alifonso, D.; Kattan, N.; Cherns, D.; Galan, M. C.; Fermín, D. J., Initial Stages in the Formation of Cu2ZnSn(S,Se)4 Nanoparticles. *Chem. Eur. J.* **2013,** *19* (47), 15847-15851.
169. Verma, S. K.; Verma, R.; Xie, Y.; Xiong, D.; Chen, W.; Hu, C.; Emmanuel, T. A.; Wang, M.; Zhao, X., Heat-Up and Gram-Scale Synthesis of Cu-Poor CZTS Nanocrystals with Controllable Compositions and Shapes. *CrystEngComm* **2017,** *19* (15), 2013-2020.
170. Lu, X.; Zhuang, Z.; Peng, Q.; Li, Y., Wurtzite Cu2ZnSnS4 Nanocrystals: A Novel Quaternary Semiconductor. *Chem. Commun.* **2011,** *47* (11), 3141-3143.

171. Singh, A.; Geaney, H.; Laffir, F.; Ryan, K. M., Colloidal Synthesis of Wurtzite Cu2ZnSnS4 Nanorods and Their Perpendicular Assembly. *J. Am. Chem. Soc.* **2012,** *134* (6), 2910-2913.
172. Zou, Y.; Su, X.; Jiang, J., Phase-Controlled Synthesis of Cu2ZnSnS4 Nanocrystals: The Role of Reactivity between Zn and S. *J. Am. Chem. Soc.* **2013,** *135* (49), 18377-18384.
173. Li, Z.; Lui, A. L. K.; Lam, K. H.; Xi, L.; Lam, Y. M., Phase-Selective Synthesis of Cu2ZnSnS4 Nanocrystals using Different Sulfur Precursors. *Inorg. Chem.* **2014,** *53* (20), 10874-10880.
174. Liao, H.-C.; Jao, M.-H.; Shyue, J.-J.; Chen, Y.-F.; Su, W.-F., Facile Synthesis of Wurtzite Copper–Zinc–Tin Sulfide Nanocrystals from Plasmonic Djurleite Nuclei. *J. Mater. Chem. A.* **2013,** *1* (2), 337-341.
175. Collord, A. D.; Hillhouse, H. W., Composition Control and Formation Pathway of CZTS and CZTGS Nanocrystal Inks for Kesterite Solar Cells. *Chem. Mater.* **2015,** *27* (5), 1855-1862.
176. Irkhina, A.; Levcenko, S.; Hinrichs, V.; Plate, P.; Unold, T., Metal Acetate Based Synthesis of Small-Sized Cu2ZnSnS4 Nanocrystals: Effect of Injection Temperature and Synthesis Time. *RSC Advances* **2017,** *7* (19), 11752-11760.
177. Wang, Z.; Elouatik, S.; Demopoulos, G. P., Understanding the Phase Formation Kinetics of Nano-Crystalline Kesterite Deposited on Mesoscopic Scaffolds via in situ Multi-Wavelength Raman-Monitored Annealing. *PCCP* **2016,** *18* (42), 29435-29446.
178. Singh, S.; Brandon, M.; Liu, P.; Laffir, F.; Redington, W.; Ryan, K. M., Selective Phase Transformation of Wurtzite Cu2ZnSn(SSe)4 (CZTSSe) Nanocrystals into Zinc-Blende and Kesterite Phases by Solution and Solid State Transformations. *Chem. Mater.* **2016,** *28* (14), 5055-5062.
179. Nguyen, T.-D.; Do, T.-O., *Size- and Shape-Controlled Synthesis of Monodisperse Metal Oxide and Mixed Oxide Nanocrystals*. 2011; Vol. 49.
180. Tan, J. M. R.; Scott, M. C.; Hao, W.; Baikie, T.; Nelson, C. T.; Pedireddy, S.; Tao, R.; Ling, X.; Magdassi, S.; White, T.; Li, S.; Minor, A. M.; Zheng, H.; Wong, L. H., Revealing Cation-Exchange-Induced Phase Transformations in Multielemental Chalcogenide Nanoparticles. *Chem. Mater.* **2017,** *29* (21), 9192-9199.
181. Jung, Y. K.; Kim, J. I.; Lee, J.-K., Thermal Decomposition Mechanism of Single-Molecule Precursors Forming Metal Sulfide Nanoparticles. *J. Am. Chem. Soc.* **2010,** *132* (1), 178-184.
182. Luo, Q.; Zeng, Y.; Chen, L.; Ma, C., Controllable Synthesis of Wurtzite Cu2ZnSnS4 Nanocrystals by Hot-Injection Approach and Growth Mechanism Studies. *Chem. Asian J.* **2014,** *9* (8), 2309-2316.
183. Dilena, E.; Xie, Y.; Brescia, R.; Prato, M.; Maserati, L.; Krahne, R.; Paolella, A.; Bertoni, G.; Povia, M.; Moreels, I.; Manna, L., CuInxGa1–xS2 Nanocrystals with Tunable Composition and Band Gap Synthesized via a Phosphine-Free and Scalable Procedure. *Chem. Mater.* **2013,** *25* (15), 3180-3187.
184. Liu, Y.; Liu, M.; Yin, D.; Qiao, L.; Fu, Z.; Swihart, M. T., Selective Cation Incorporation into Copper Sulfide Based Nanoheterostructures. *ACS Nano* **2018,** *12* (8), 7803-7811.
185. Khare, A.; Himmetoglu, B.; Johnson, M.; Norris, D. J.; Cococcioni, M.; Aydil, E. S., Calculation of the Lattice Dynamics and Raman Spectra of Copper Zinc Tin Chalcogenides and Comparison to Experiments. *J. Appl. Phys.* **2012,** *111* (8), 083707.
186. Kandare, S. P.; Dahiwale, S. S.; Dhole, S. D.; Rao, M. N.; Rao, R., Order-Disorder Transition in Nano-Cu2ZnSnS4: A Raman Spectroscopic Study. *Mater. Sci. Semicond. Process.* **2019,** *102*, 104594.
187. Berg, D. M.; Djemour, R.; Gütay, L.; Siebentritt, S.; Dale, P. J.; Fontane, X.; Izquierdo-Roca, V.; Pérez-Rodriguez, A., Raman Analysis of Monoclinic Cu2SnS3 Thin Films. *Appl. Phys. Lett.* **2012,** *100* (19), 192103.
188. Talapin, D. V.; Rogach, A. L.; Haase, M.; Weller, H., Evolution of an Ensemble of Nanoparticles in a Colloidal Solution: Theoretical Study. *J. Phys. Chem. B* **2001,** *105* (49), 12278-12285.
189. Pearson, R. G., Hard and Soft Acids and Bases. *J. Am. Chem. Soc.* **1963,** *85* (22), 3533-3539.

190. Steudel, R., Properties of Sulfur-Sulfur Bonds. *Angew. Chem. Int.* **1975,** *14* (10), 655-664.
191. Hu, Y.; Jiang, Z.; Xu, C.; Mei, T.; Guo, J.; White, T., Monodisperse ZnO Nanodots: Synthesis, Charaterization, and Optoelectronic Properties. *J. Phys. Chem. C* **2007,** *111* (27), 9757-9760.
192. Romero, N. A.; Nicewicz, D. A., Organic Photoredox Catalysis. *Chem. Rev.* **2016,** *116* (17), 10075-10166.

Appendix

Synthesis of Zinc Oxide Nanoparticles:
ZnO NPs were synthesized from zinc chloride, linoleic acid and sodium hydroxide in ethanol following a previously reported procedure.[191] $ZnCl_2$ (0.50 g, 3.7 mmol) was dissolved in deionized H_2O (7 mL) through sonication for 5 min. Then, NaOH (0.50 g, 12.5 mmol) and linoleic acid (4 mL, 12.8 mmol) were combined in ethanol (16 mL) and sonicated until the solution was clear. Both solutions were then mixed and held under constant stirring for 30 min. The final product was separated by centrifugation at 7000 rpm and then dispersed (2×) in ethanol to remove any unreacted material, followed by centrifugation. The final product was air dried overnight to yield a white powder.

Optimization of ZnO NW Growth:
The growing time of the ZnO NWs was optimized to minimize the electron-hole recombination and to facilitate the carrier collection pathways. It was observed that NWs achieve their optimal length after 3 hrs of growth (1.3 μm) where the NWs are tightly packed and highly oriented, while less than 3 hrs of growth results in arrays of disordered wires (Figure A19). More than 3 hrs of growth results in taller wires that may diminish the semiconducting properties of the device. In addition, the number of drops of ZnO NPs dispersion used for spin-coating the FTO films was also optimized. It was determined that three cycles of two drops per spin-coating cycle was the optimal number of drops in order to obtain uniform films of wires while keeping the aggregation of particles at minimum (Figures A19 and A20).

Synthesis of other CDs for the comparative study:
The green CDs were synthesized from a previously reported procedure.[37] Briefly, 20 mL of a 0.1 M solution of glutathione in formamide was prepared and sonicated until the solution became clear. A 10 mL sample was then placed in a microwave reaction vessel (35 mL capacity). The solution was heated in a microwave reactor at 180 °C for 5 min. The dark green product was then subjected to dialysis for 5 days in Millipore water to remove impurities. After dialysis, the product was concentrated in vacuo at 50 °C until the volume was reduced to 3 mL. Then three organic washes with acetone (99%) were performed to further purify the CDs. The product was left to air dry and then was resuspended in water or ethanol for further experiments. The red CDs are synthesized from citric acid and formamide. Briefly, citric acid (5 g, 26 mmol) was dissolved in methanol (75 mL) and formamide (25 mL) was added. The solution was homogenized by stirring for 5 min, then, the solution was transferred to a hydrothermal reactor and the reaction was carried out at 180 °C for 4 hrs with stirring at 300 rpm. The product is a black liquid that was dialyzed for 5 days in Millipore water. Then, the solution was concentrated to 5 mL and three organic washes with acetone (99%) were performed to remove impurities. The product was then left in an oven to dry at 70 °C and resuspended in water or ethanol for further experiments.

^{1}H NMR and ^{13}C NMR:
^{1}H and ^{13}C Nuclear Magnetic Resonance (NMR) were collected on a Bruker 500 (500 MHz) instrument. The spectra were referenced to the residual solvent signal ($CDCl_3$) at δ 7.26 ppm and δ 77.16 ppm respectively.

Mass Spectrometry:
High resolution mass spectroscopy was acquired with a Waters Model QTOF Ultima instrument in a positive mode at an energy of 5 V with an electrospray as the ionization source (3.5 kV) using acetonitrile as a solvent.

Work-up procedure for α-heteroarylation:
After the reaction period, the reaction mixture was transferred to a separatory funnel. The reaction vessel was rinsed with 20 mL of ethyl acetate and the organic layer was washed with 25 mL of brine (3×). The brine extractions were in turn washed with 20 mL of ethyl acetate and the combined organic phases were dried over sodium sulfate. The product was then concentrated in vacuo and 1,3,5-trimethoxybenzene (TMB) was added as an internal standard to calculate the yield through ^{1}H NMR. Briefly, TMB (12 mg) was added to the product and the mixture was dissolved with $CDCl_3$. The ^{1}H NMR spectrum was acquired with a 5 s relaxation delay between scans.
The product was isolated from the starting materials through column chromatography using silica (43-60 μm) with toluene as the mobile phase.

Gibbs Free Energy for Photoinduced Electron Transfer:
The Gibbs free energy for photoinduced electron transfer can be computed using the following equation:[192]

$$\Delta G^o_{PET} = E_{D/D^+} - E_{A/A^-} - E_{0,0} - \frac{e^2}{\varepsilon r} \qquad \textbf{Eq. A1.1}$$

where F is the Faraday constant (23.061 kcal V^{-1} mol^{-1}), E_{red} and E_{ox} are the redox potentials for the species undergoing the redox reaction, $E_{0,0}$ is the excited state energy, and $e^2/\varepsilon r$ accounts for the solvent-dependent energy difference due to the Coulombic effect on the charge separation.

$$\Delta G^o_{PET} = +0.42\,V - (-2.44\,V) - 3.00\,V - \frac{(1.602 * 10^{-19}C)^2}{37.8\,Fm^{-1} * (462 * 10^{-12}m)}$$

$$\Delta G^o_{PET} = -0.14\,kcal/mol$$

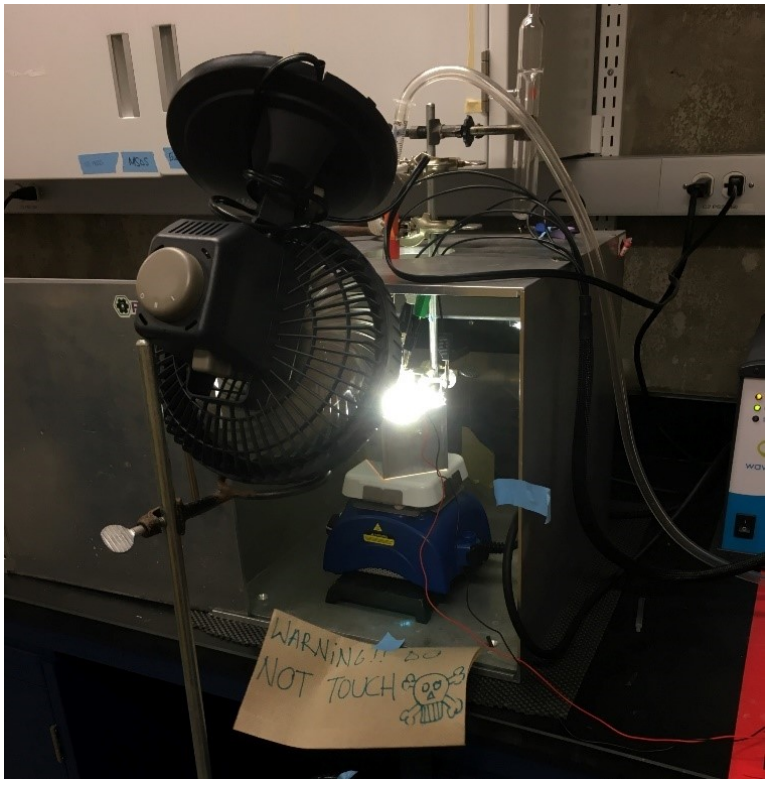

Figure A1. Picture of the reaction setup. The reaction vessel is clamped inside a home build photoreactor and above a stirring plate. A three-electrode system is set up to monitor the reaction through a bulk electrolysis experiment. Argon is bubbled into the solution throughout the whole reaction and a fan is placed in front of the setup to cool the photoreactor and to maintain the temperature of the reaction at 23 °C.

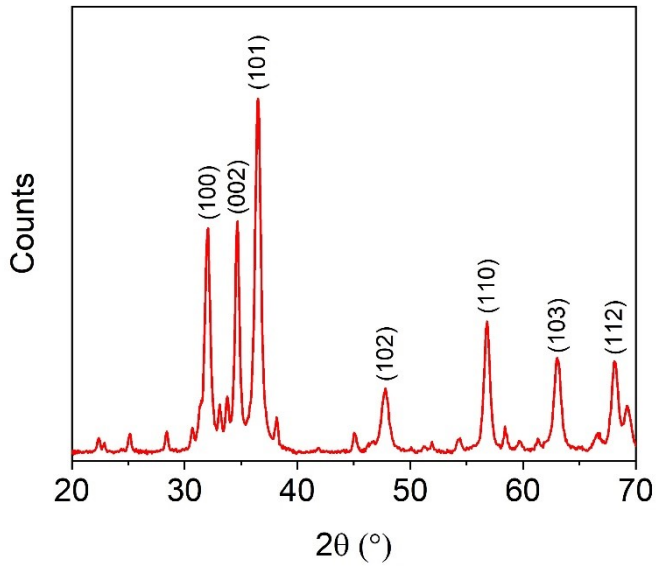

Figure A2. PXRD diffractogram for the ZnO NPs. The diffractogram shows crystalline reflections for the (100), (002), (101), (102), (110), (103), and (112) planes. This pattern agrees with the literature values for wurtzite ZnO.[122]

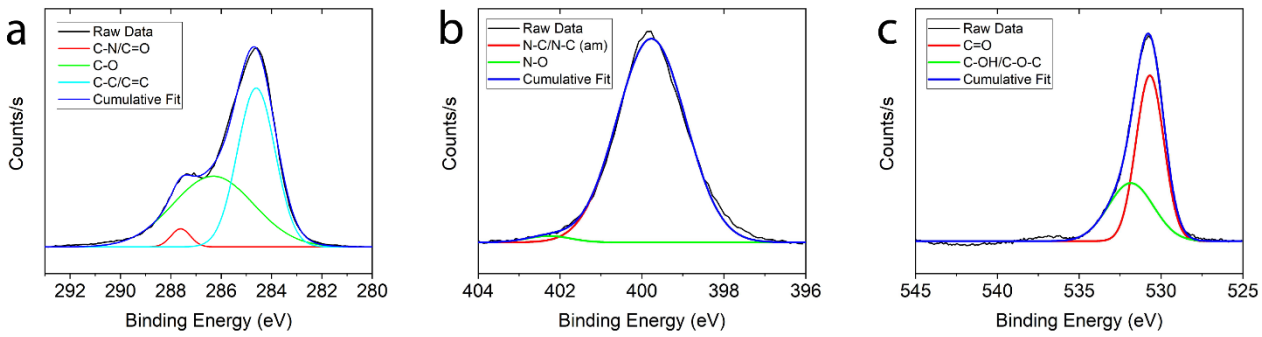

Figure A3. HR-XPS for: a) C1s; b) N1s; and c) O1s

Table A1. Wavenumber assignments for the **PD2-CDs** FTIR

Wavenumber (cm^{-1})	***Assignment***
1213	ν Acyl C-O
1364	ν Amide C-N
1532	ν Carboxyl C=O
1556	ν Amide C=N
1632	ν Amide C=O
2977	ν Alkyl C-H
3500-3000	ν Surface O-H

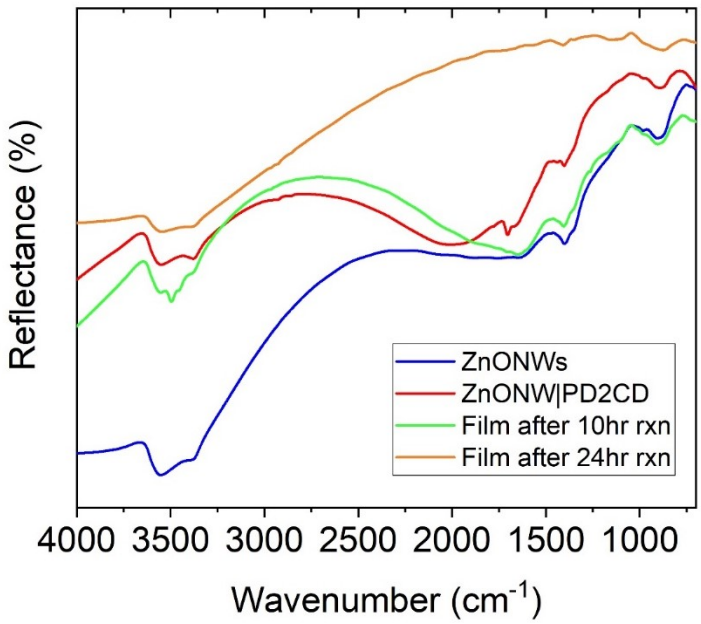

Figure A4. Diffuse reflectance infrared Fourier transform spectra for the ZnO NWs (blue trace) and functionalized films before (red trace) and after a 10 (green trace) and 24 (orange trace) hr reaction.

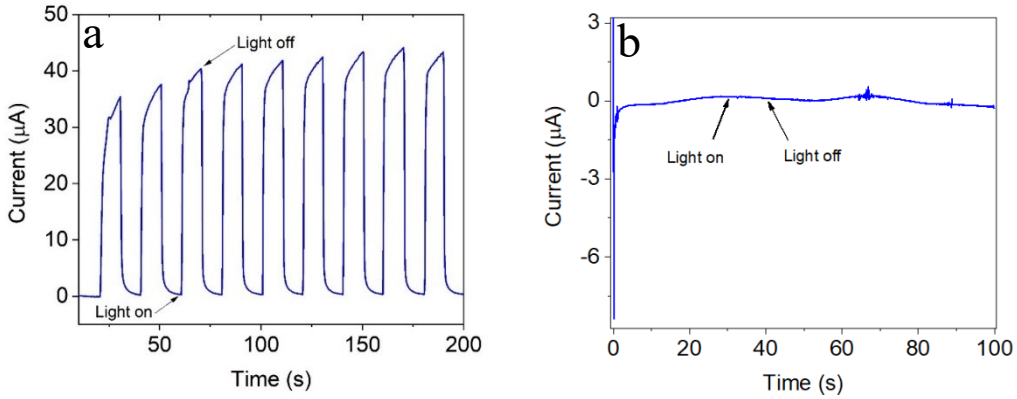

Figure A5. Chronoamperogram for the ZnO NWs upon (a) UV-light (λ_{ex} = 365 nm) and (b) white light illumination. RE: Ag/AgCl, CE: Pt wire, WE: film of ZnO NWs in 0.1 M KCl.

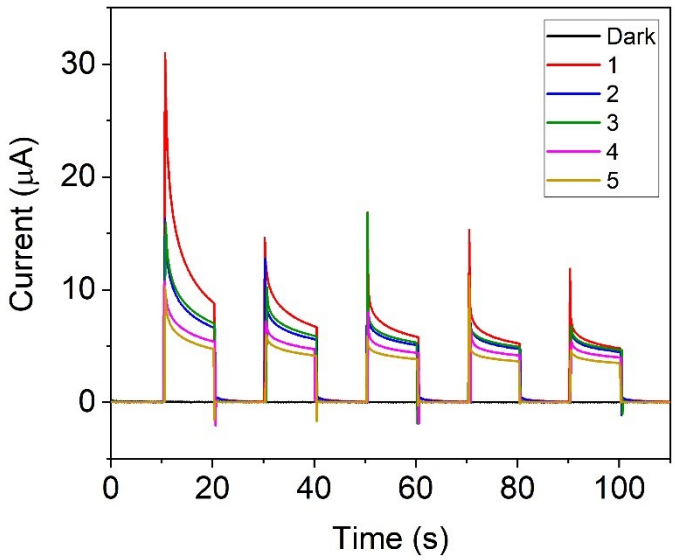

Figure A6. Chronoamperometry experiments in five fresh electrolyte solutions for five light on-off cycles each. There is no significant decrease in current which confirms a strong attachment between the **PD2-CDs** and the ZnO.

Table A2. Current density data for Figure A6.

Solution	Cycle 1 (%)	Cycle 2 (%)	Cycle 3 (%)	Cycle 4 (%)	Cycle 5 (%)
1	100	100	100	100	100
2	68.22	79.97	84.73	88.77	91.84
3	72.12	84.60	88.67	91.76	94.95
4	53.01	66.07	72.40	77.10	80.84
5	46.59	58.05	62.80	66.87	70.32

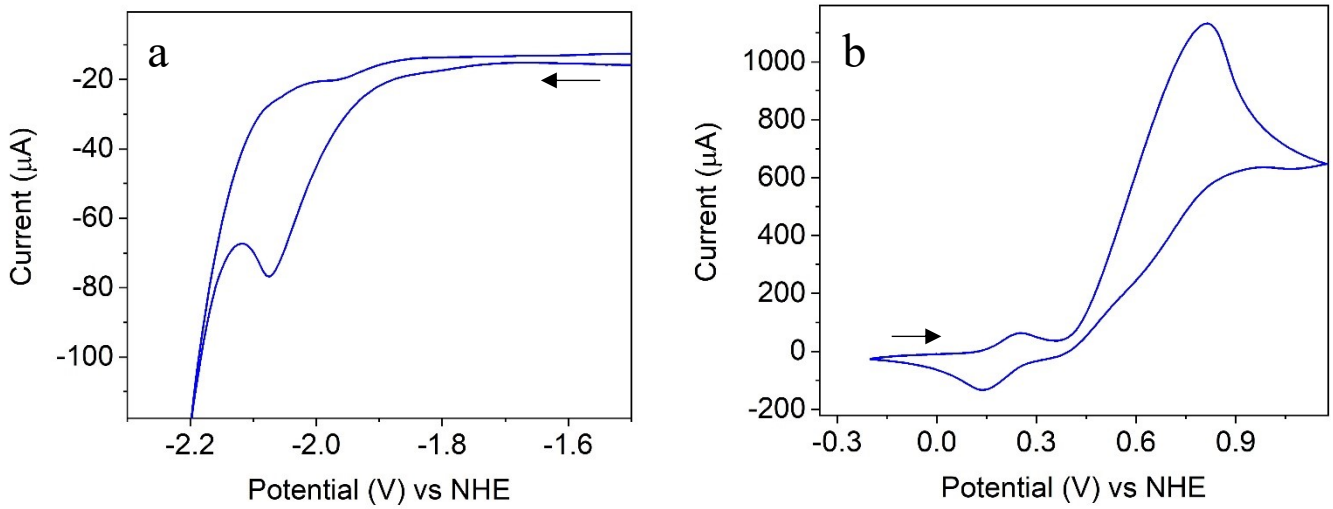

Figure A7. Electrochemical characterization of the starting materials through cyclic voltammetry; a) reduction scan of 2-chlorobenzothiazole; b) oxidation scan of 1-phenylpyrrolidine. RE: Ag wire, CE: Pt wire, WE: glassy carbon, 0.1 M $TBAPF_6$ in acetonitrile (scan rate: 100 mV/s).

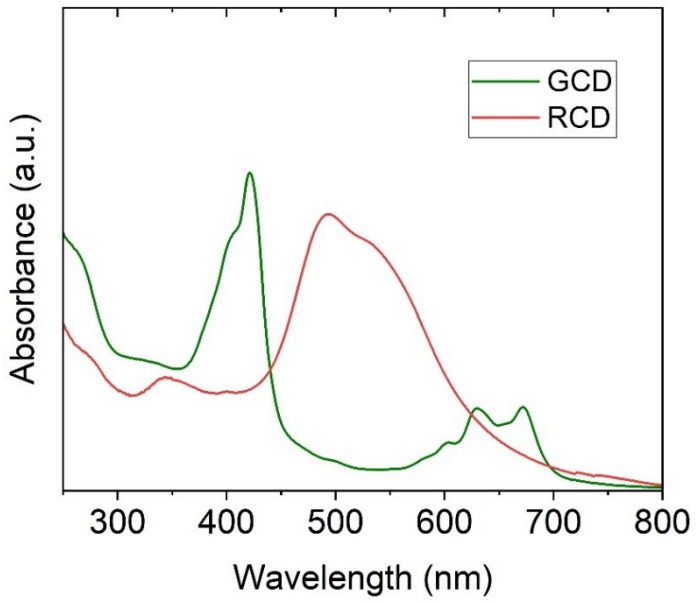

Figure A8. Absorption spectra for the GCDs (green trace) and RCDs (red trace) dispersed in water.

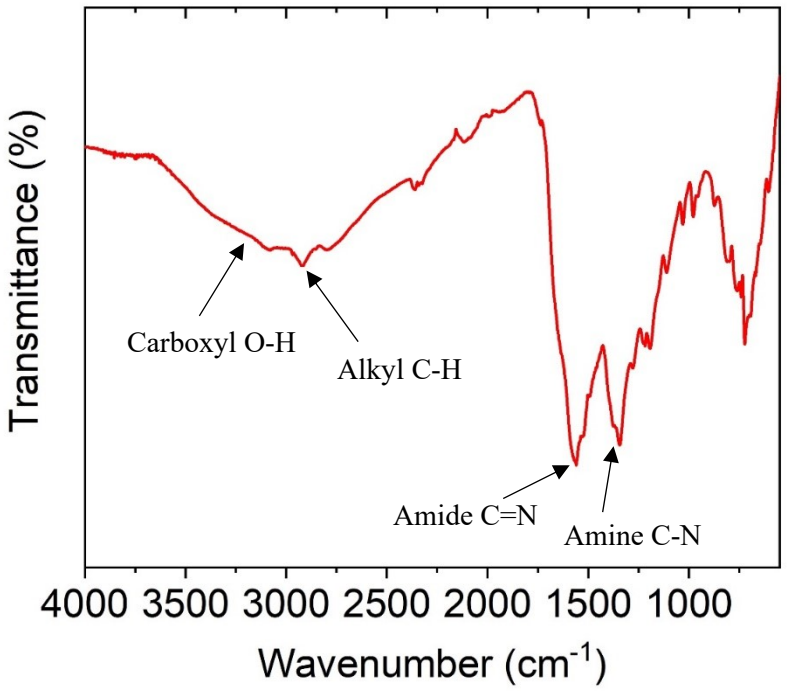

Figure A9. FTIR spectrum for the RCDs.

Table A3. Wavenumber assignments for the FTIR of RCDs

Wavenumber (cm^{-1})	*Assignment*
1374	ν Amine C-N
1562	ν Amide C=N
2923	ν Alkyl C-H
3500-3000	ν Surface O-H

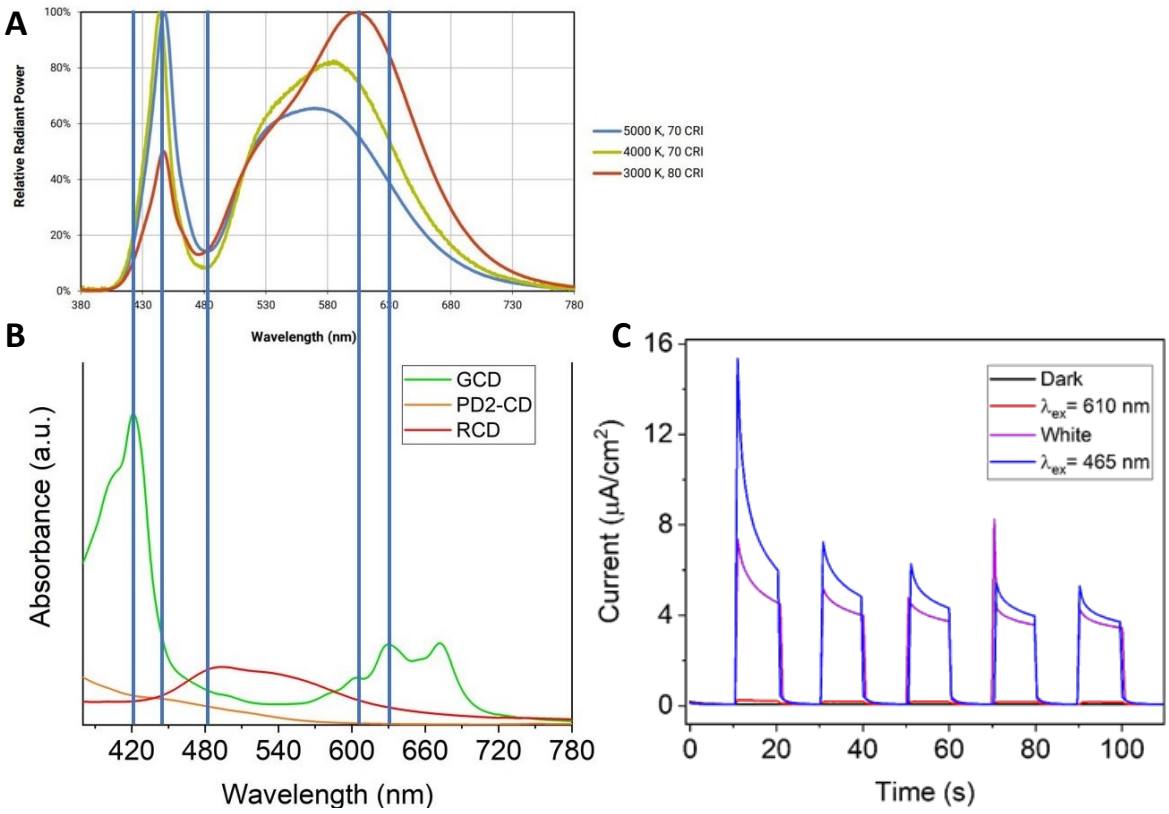

Figure A10. A) The emission profile for the white LEDs is matched to the B) absorbance spectra of the three different types of CDs used in this work. The blue component of the LEDs matches the shoulder of the PD2-CDs. C) Chopped-light chronoamperometry experiment with **ZnO NWs|PD2-CDs** films under varying LED illumination (white light LEDs, purple trace; red LEDs, red trace; blue LEDs, blue trace). Irradiation with red LEDs yields low photocurrent compared to white and blue LEDs.

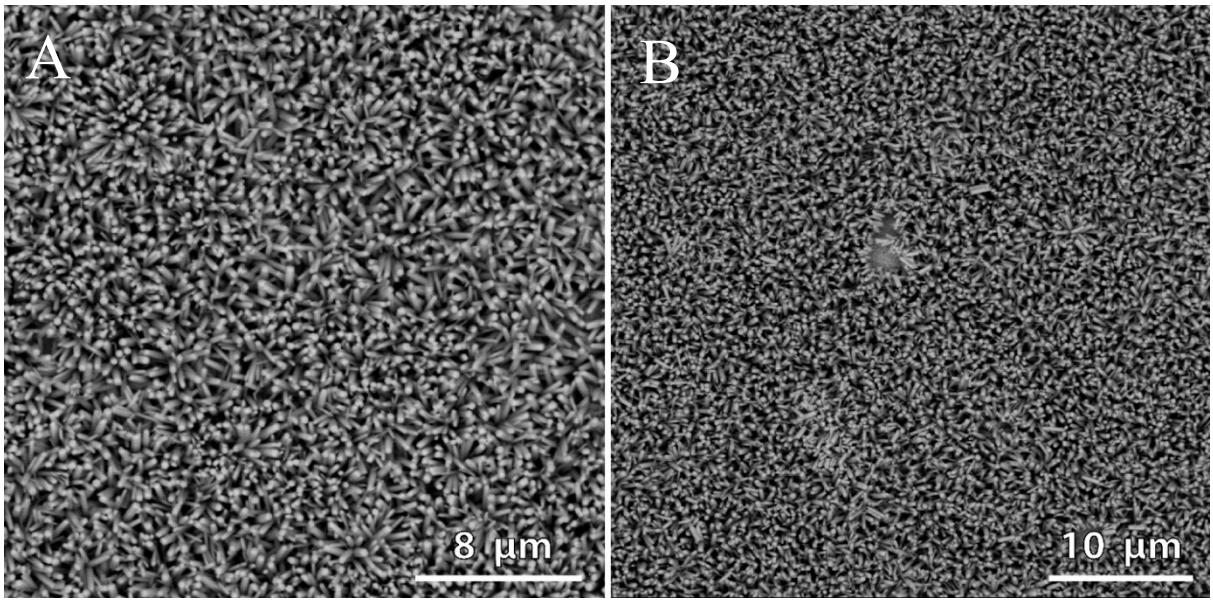

Figure A11. SEM images of the film (a) before and (b) after a 10 hrs reaction. The NWs remain in good condition.

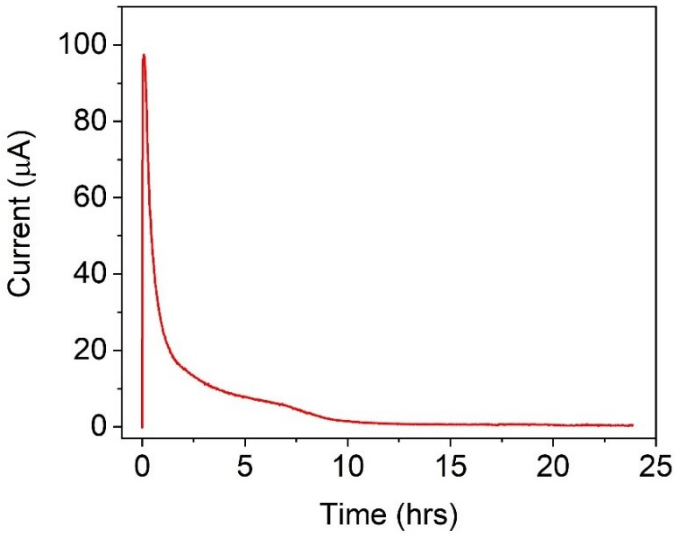

Figure A12. Bulk electrolysis experiment without applied bias. This experiment was performed to monitor the course of the reaction. There is a large increase in current in the first 30 min of the reaction due to a high charge buildup caused by the oxidation of the 1-phenylpyrrolidine at the film/solution interface. The current throughout the film stabilizes after ca. 2.5 hrs and at 10 hrs there is no significant oxidation observed and the reaction is nearing completion.

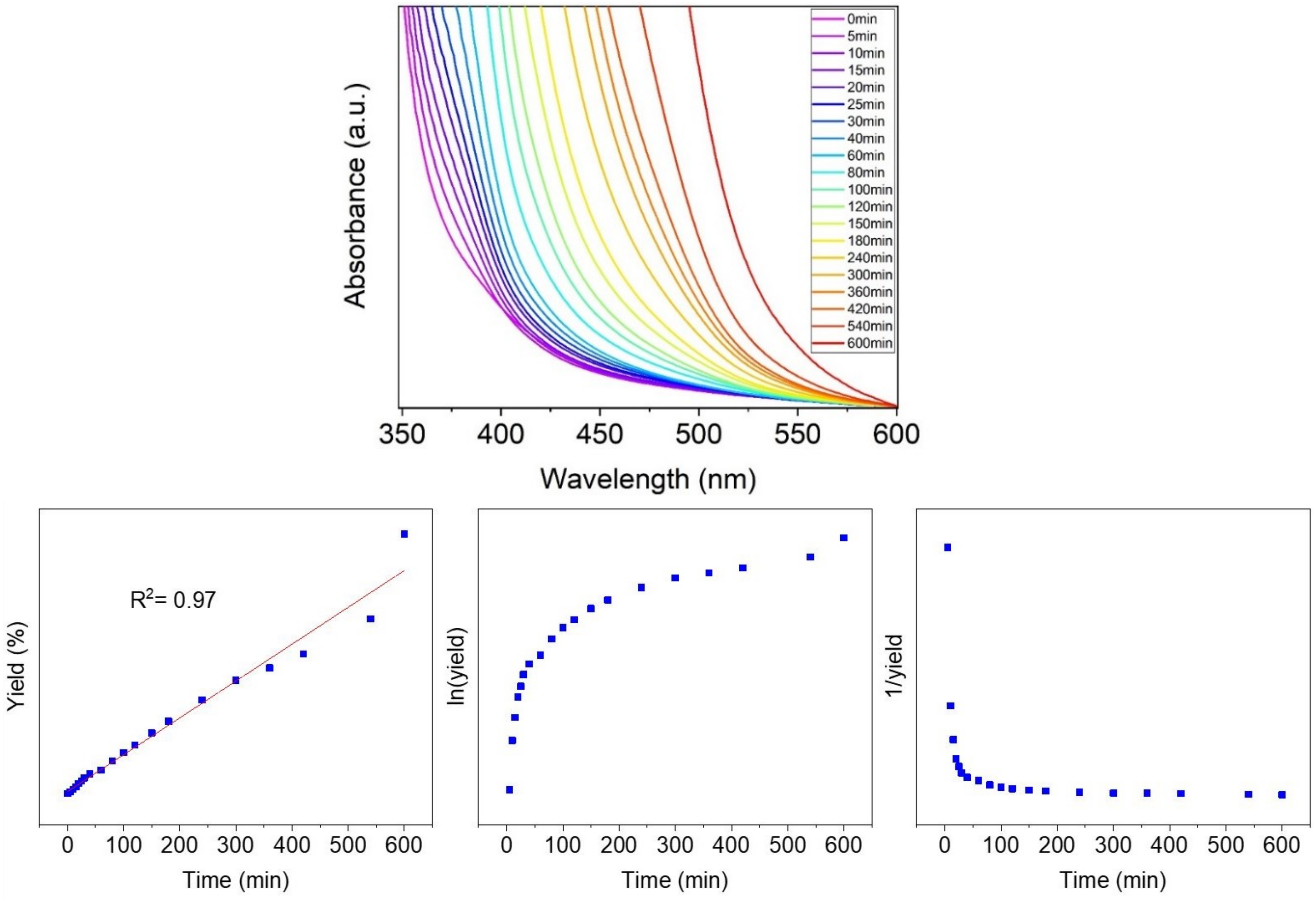

Figure A13. Time-course UV-Vis experiment for the evaluation of the kinetics of the reaction. The reaction proceeds in a steady fashion throughout 10 hr of reaction following zero-order kinetics

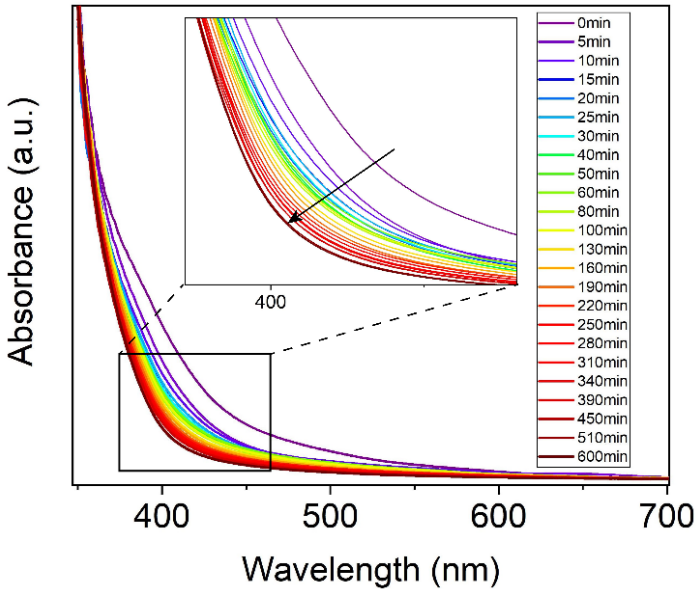

Figure A14. Time-course UV-Vis experiment for the oxidation of 1-phenylpyrrolidine without the presence of 2-chlorobenzothiazole. There is a rapid decrease in the concentration of the amine in the first 15 min correlating to the bulk electrolysis experiment (Figure A12). There is a steady decrease in the absorbance following this rapid decrease in the concentration

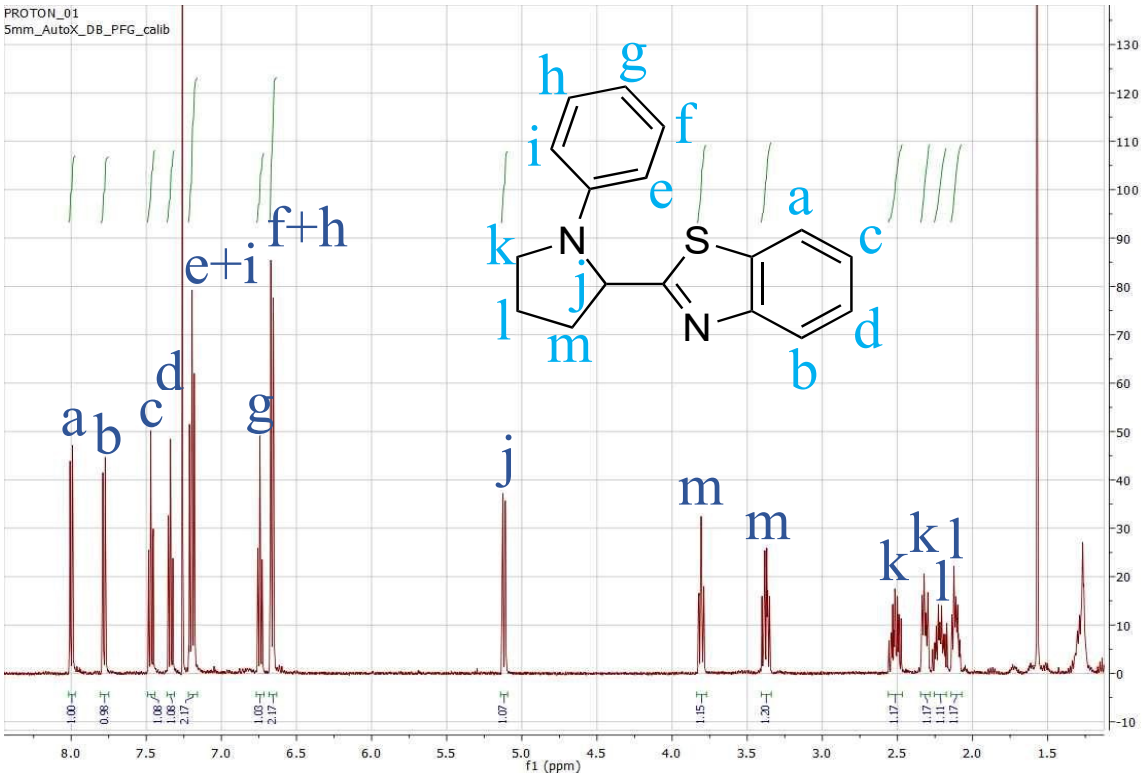

Figure A15. ^{1}H NMR **3** (500 MHz, $CDCl_3$): δ 8.00 (d, 1H$_a$), 7.78 (d, 1H$_b$), 7.48 (dd, 1H$_c$), 7.34 (dd, 1H$_d$), 7.20 (dd, 2H$_e$), 6.75 (t 1H$_f$), 6.66 (d, 2H$_g$), 5.12 (d, 1H$_h$), 3.81 (dd, 1H$_i$), 3.37 (m, 1H$_j$), 2.56 – 2.46 (m, 1H$_k$), 2.32 (m, 1H$_l$), 2.27 – 2.16 (m, 1H$_m$), and 2.11 (m, 1H$_n$).

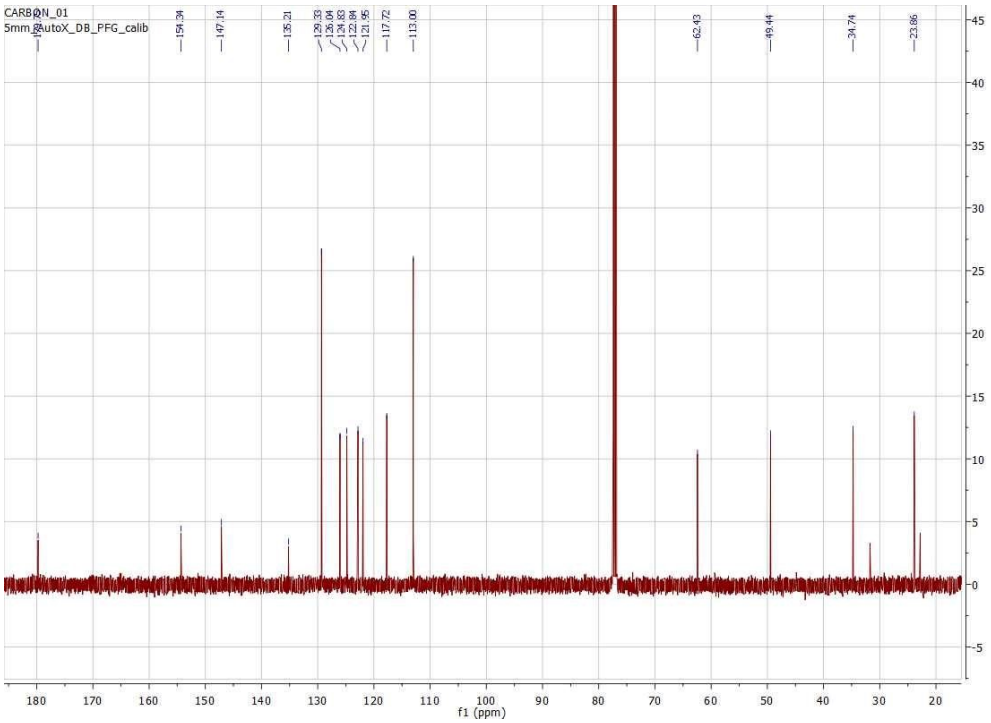

Figure A16. ^{13}C NMR **3** (500 MHz, $CDCl_3$): δ179.8, 154.3, 147.1, 135.2, 129.3, 126.0, 124.8, 122.8, 122.0, 117.7, 113.0, 62.4, 49.4, 34.7, 23.9

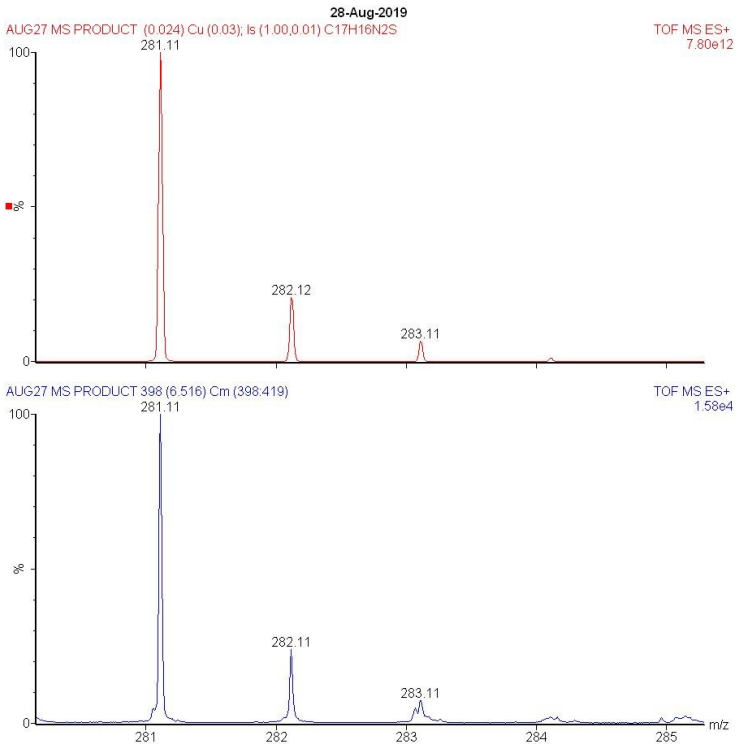

Figure A17. Mass spectrum for the isolated product **3** in acetonitrile. We observe that the predicted pattern in red (top) matches the pattern from **3** in blue (bottom) at $[M+H]^+$=281.11 *m/z*.

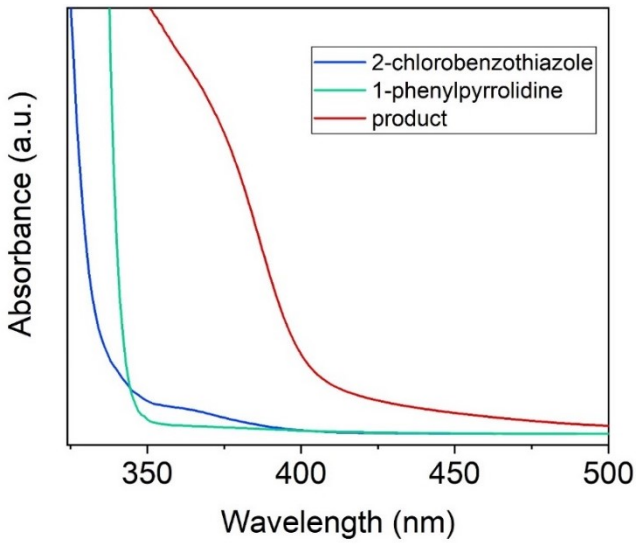

Figure A18. UV-vis spectrum for the starting materials 1-phenylpyrrolidine (**1)** and 2-chlorobenzothiazole (**2)**, and 2-(1-phenylpyrrolidin-2-yl)benzo[d]thiazole (**3**). The spectrum for **2** shows an absorption maximum at 360 nm with a shoulder that extends to 400 nm

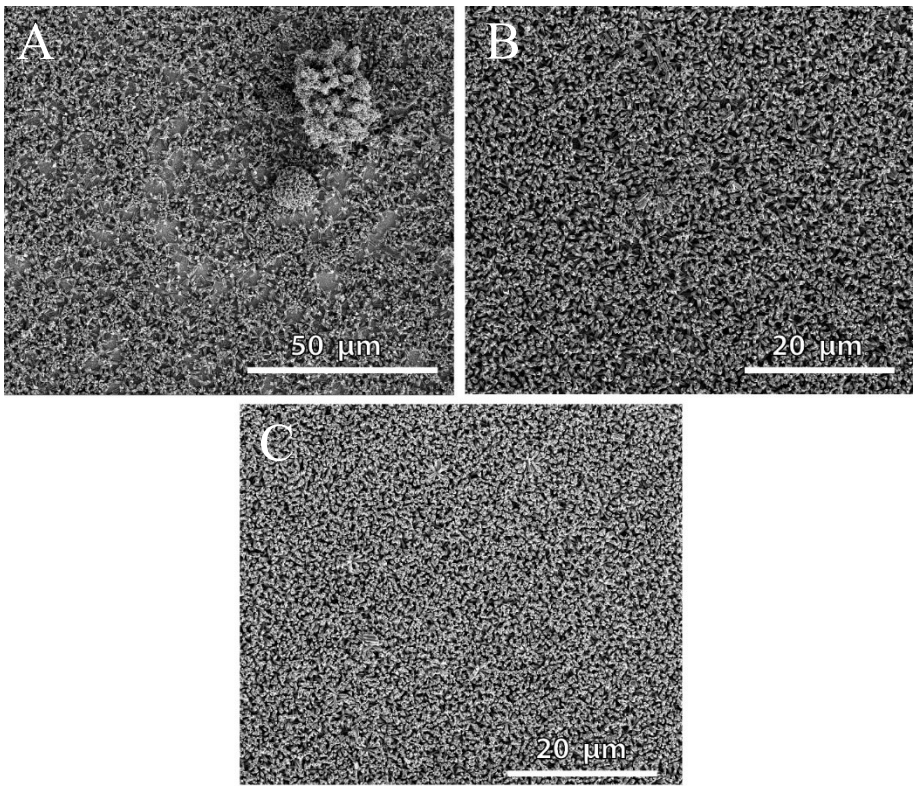

Figure A19. SEM images for ZnO NW films grown from a) 2; b) 4; c) 6; drops of seeding solution. As the number of drops increase, the roughness decreases and wire density/uniformity increase.

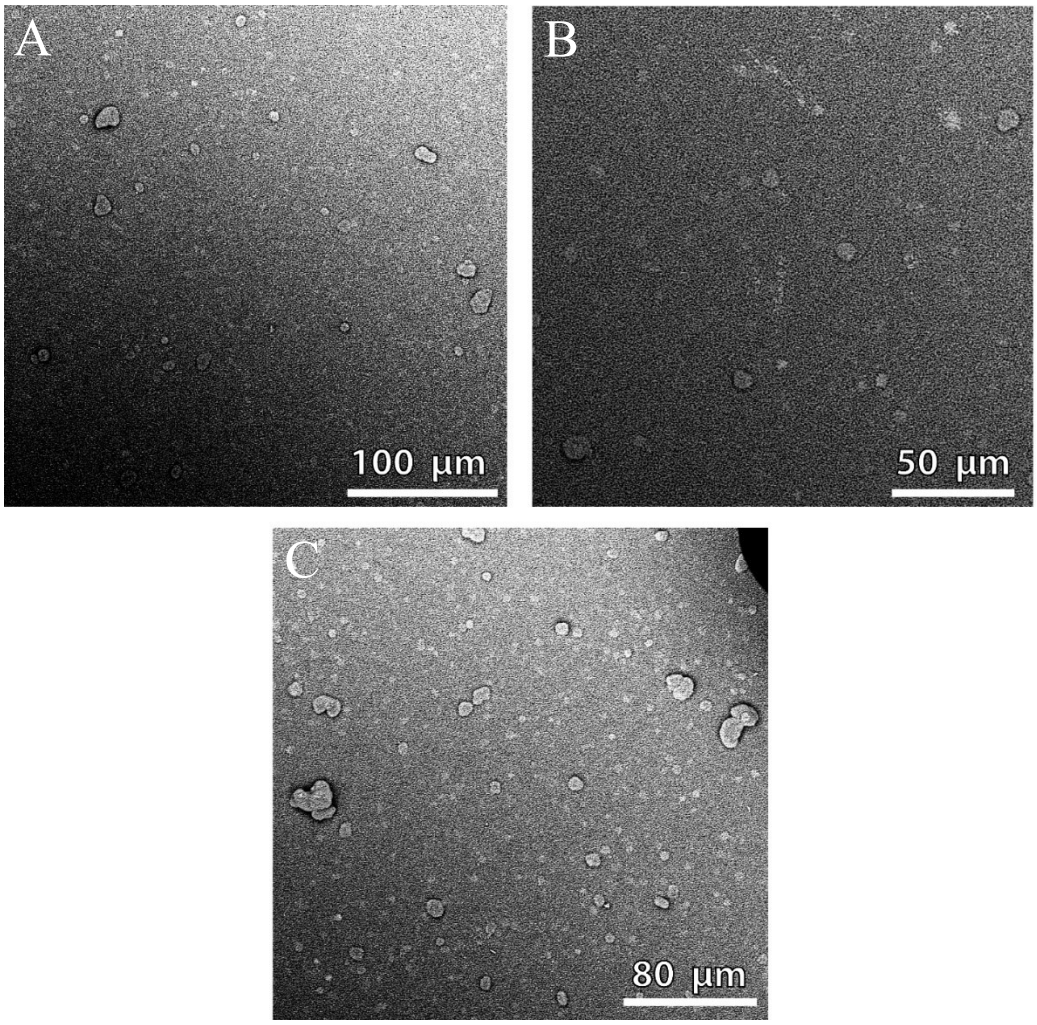

Figure A20. SEM images for ZnO NW films grown from a) 10; b) 20; c) 40 drops of seeding solution. Here the roughness and aggregation increase as the number of seeding solution drops increases.

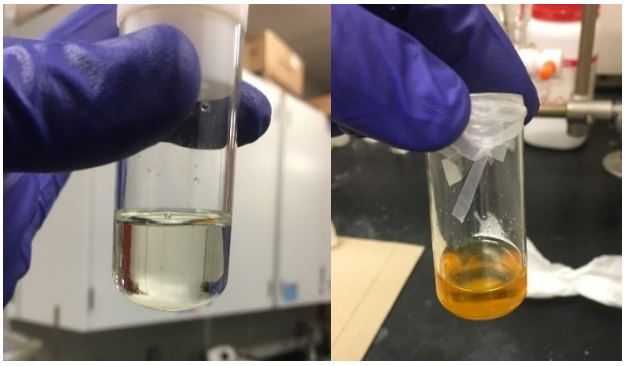

Figure A21. Picture of the solution before and after the reaction of **1** and **2** to form **3**.

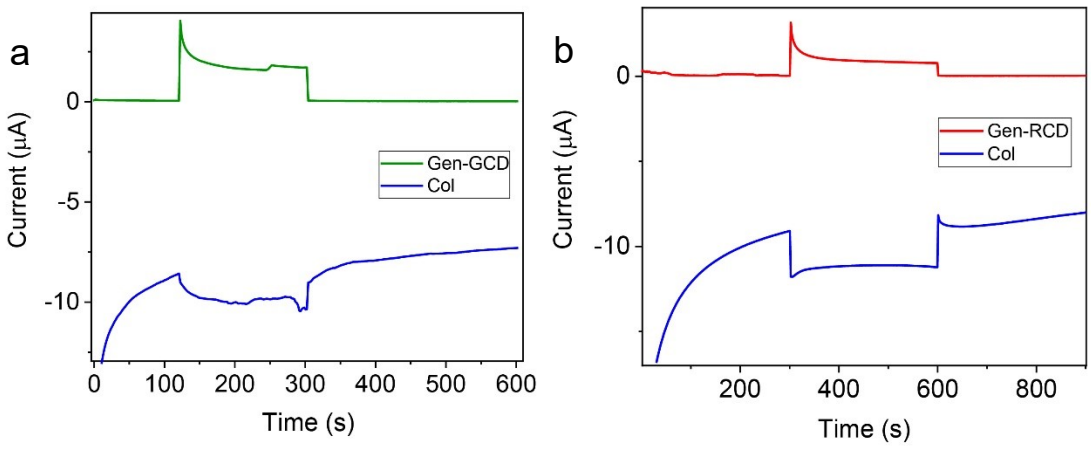

Figure A22. This figure shows the dual-electrode bulk electrolysis experiments for the oxidation of a water splitting catalyst with GCDs (a, green trace) and RCDs (b, red trace) at the generator electrodes. These plots also show the reductive current due to the oxygen evolution from water splitting (a and b, blue traces).

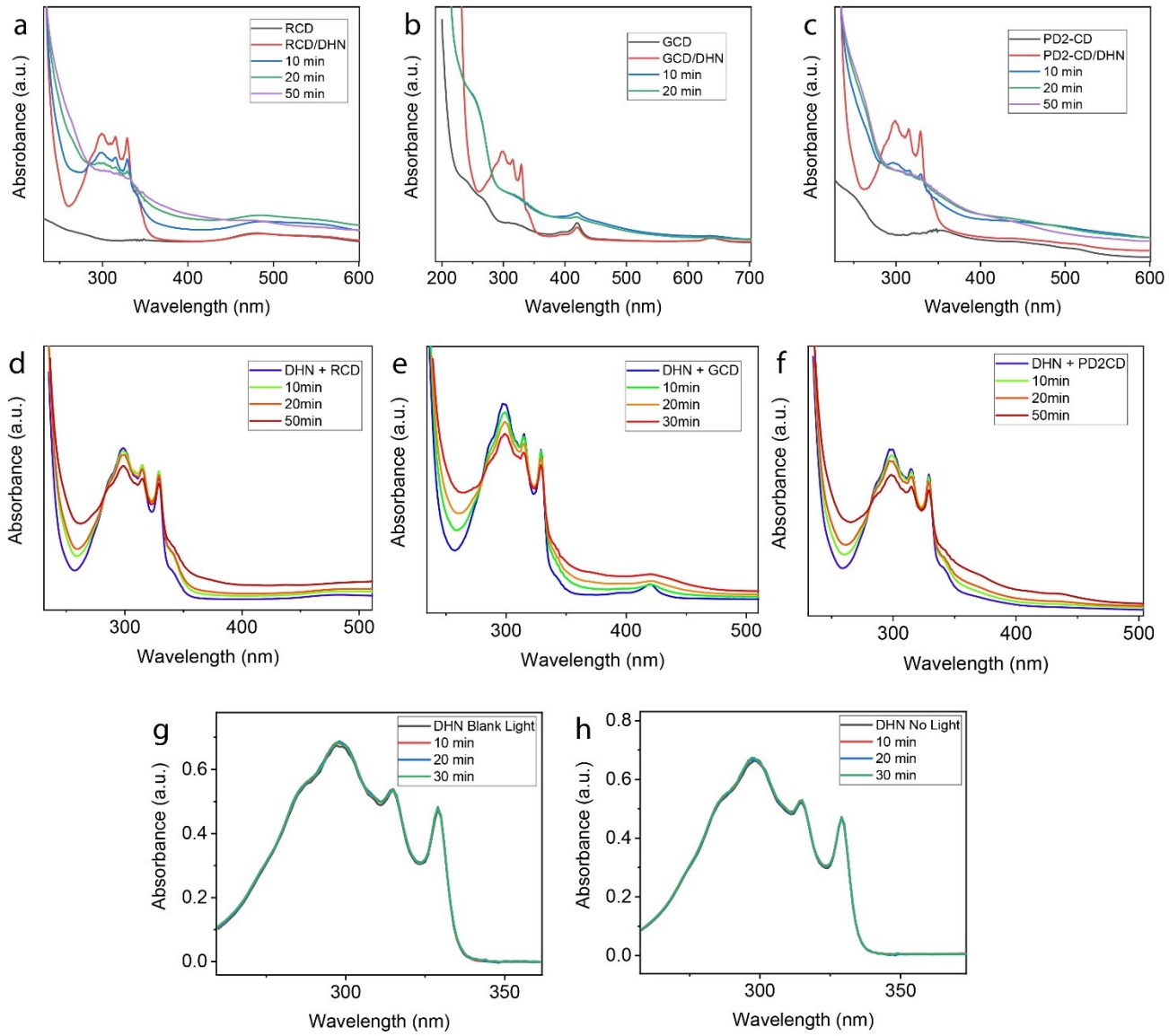

Figure A23. These UV-Vis plots show the sensitization of singlet oxygen by the three different types of CDs. Plots (a-c) depict the photodegradation of DHN through singlet oxygen generated with a dispersion of RCDs (a), GCDs (b), and PD2-CDs (c) in water saturated with O_2. The same experiments were performed under an argon atmosphere (d-f) where no significant DHN photodegradation was observed. Control experiments were obtained under light irradiation (g) and in the dark (h) for an O_2 saturated solution of DHN in water. No photodegradation is observed in the absence of CDs.